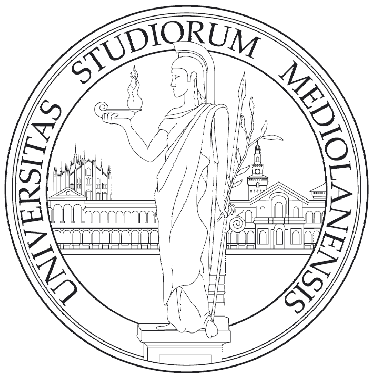

UNIVERSITÀ DEGLI STUDI DI MILANO

Facoltà di Scienze Matematiche Fisiche Naturali

DOTTORATO DI RICERCA IN

FISICA, ASTROFISICA E FISICA APPLICATA

Supersymmetry discovery potential in the 2 leptons channel with ATLAS

SETTORE SCIENTIFICO DISCIPLINARE FIS/04

Coordinatore: Prof. Gianpaolo Bellini
Tutore: Prof. Francesco Ragusa

Tesi di Dottorato di:
Umberto De Sanctis
Ciclo XXI

Anno Accademico 2008-2009

If you can keep your head when all about you
Are losing theirs and blaming it on you,
If you can trust yourself when all men doubt you,
But make allowance for their doubting too;
If you can wait and not be tired from waiting,
Or being lied about, don't deal in lies,
Or being hated, don't give way to hating,
And yet don't look too good, nor talk too wise:
If you can dream - and not make dreams your master;
If you can think - and not make thoughts your aim;
If you can meet with Triumph and Disaster
And treat those two impostors just the same;
If you can bear to hear the truth you've spoken
Twisted by knaves to make a trap for fools,
Or watch the things you gave your life to, broken,
And stoop and build 'em up with worn-out tools;
If you can make one heap of all your winnings
And risk it on one turn of pitch-and-toss,
And lose, and start again at your beginnings
And never breathe a word about your loss;
If you can force your heart and nerve and sinew
To serve your turn long after they are gone,
And so hold on when there is nothing in you
Except the Will which says to them: "Hold on!"
If you can talk with crowds and keep your virtue,
Or walk with Kings - nor loose the common touch,
If neither foes nor loving friends can hurt you,
If all men count with you, but none too much;
If you can fill the unforgiving minute
With sixty seconds' worth of distance run:
Yours is the Earth and everything that's in it,
And - which is more - you'll be a Man, my son!

Rudyard Kipling

Contents

Introduction

The main argument of this PhD thesis is the evaluation of the ATLAS detector potential to discover Supersymmetry and to estimate the masses of the supersymmetric particles produced, using the signature characterised by the presence of two isolated leptons in the final state.
The analysis strategy will be developed concentrating on the initial data taking period of the Large Hadron Collider (LHC), with an expected integrated luminosity of 1 fb^{-1}.
After a brief introduction on Supersymmetry, explaining its mathematical structure, the motivations that make it one of the more suitable candidates to extend the Standard Model, and the searches currently in progress on this topic, I will describe the particular supersymmetric model used in this work: the mSUGRA framework. (Chapter1).
In Chapter 2, a brief overview of the ATLAS detector is given, while in Chapter 3, the Monte Carlo generators used to produce the physics samples employed in the analysis are described. I will also concentrate on the reconstruction performances of the physical objects crucial for this analysis: electrons, muons, jets and missing energy.
In Chapter 4, the focus will move on methods that allow to estimate from data the Standard Model background to Supersymmetry searches. The robustness and reliability of the methods will be analysed, evaluating the systematic uncertainties related to the detector performances and finally showing the Supersymmetry discovery potential in the mSUGRA parameter space.
Finally, the techniques to extract some information on the SUSY mass particles spectrum using the two reconstructed leptons will be the main topic of Chapter 5. Here, the decay of some supersymmetric particles will be reconstructed pointing out the characteristic edge in the di-lepton invariant mass distribution that allows to extract information about the masses of the supersymmetric particles involved in the decay chain.

Chapter 1

Theoretical introduction

1.1 The Standard Model

The Standard Model (SM) [1] [2] is a theory built in the '60 that proved to be the best theory to explain, in a compelling way, the large amount of experimental data collected in the last 50 years in particle physics. It describes three of the four fundamental forces: the strong interaction, the weak interaction and the electromagnetic interaction between fundamental fermions(leptons and quarks). At the moment it does not include the gravitational interaction, but its effects are negligible at the electroweak scale where the Standard Model has been tested. The Standard Model is built as a local gauge theory that foresee the existence of bosonic gauge fields (massless or not) as carriers of these fundamental interactions.
The SM gauge group is $G_{SM} = SU(3)_C \otimes SU(2)_L \otimes U(1)_Y$, meaning that the three symmetry groups are not unified in a single gauge group with only one set of quantum numbers. The SM is then a theory that does not foresee any kind of unification between the fundamental interactions.
This gauge group foresees the existence of 12 particles: 8 massless vectorial bosons called gluons mediating the strong coloured interactions, 3 massive vector bosons W^+, W^- and W^0, mediating the weak interaction and the massive B boson, mediating the electromagnetic interaction.
In this model it is also introduced a complex doublet of scalar fields, the Higgs field. It plays a fundamental role in the spontaneous electroweak symmetry breaking process that gives a mass to the weak vector bosons, and via the Yukawa couplings to the SM fundamental fermions.
Let us now describe briefly these three sectors that are the building blocks of the Standard Model: the gauge sector, the fermionic sector and the Higgs sector.

1. The gauge sector
   Composed by bosons with spin-parity $J^P = 1^-$, one can classify them into:
   Gluons G^a_μ There are 8 massless mediators of the strong interaction. Their gauge group is $SU(3)_C$ and their quantum number is called colour. The strong interaction that brings together the nucleons is, then, reduced to an interaction among quarks mediated by these gluons in the nucleons themselves.
   Vector bosons W^j_μ**,** B_μ There are 4 massive mediators of the weak interaction and their gauge group is respectively $SU(2)_L$ (for the W^j_μ) and $U(1)_Y$ (for the B_μ). Two of them (W^1_μ and W^2_μ) are charged while the others (W^3_μ and B_μ) are neutral. Before the spontaneous electroweak symmetry breaking mechanism, all these bosons are massless, while the mass eigenstates come from a mixing between the neutral bosons W^3_μ and B_μ, with a mixing angle called Weinberg angle θ_W.

2. The fermionic sector
   Composed by spin 1/2 elementary particles without any internal structure. There are 3 generations of leptons and quarks with different quantum numbers based on their chirality, because the SM gauge groups distinguish between left handed and right handed fermions.
   Leptons There are 3 left-handed doublets of weak isospin, composed by a negatively charged lepton (electron, muon and tau) and its respective neutrino and three right-handed singlets, composed only by the charged component of the three generations. They are sensible only to the weak and electromagnetic interaction.
   Quarks They are arranged with the same doublets/singlets structure of the leptons, but with the addition of three colours for each doublet/singlet. They are also characterised by a fractional electric charge: +2/3 and -1/3 respectively for the two components of each doublet. They are sensible to all the three forces.

3. The Higgs sector
   In the minimal version, the SM foresees only one complex doublet of scalar fields $\phi = (\phi^+, \phi^0)$ that gives a mass to the W^j_μ and B_μ bosons after a spontaneous electroweak symmetry breaking mechanism of the gauge group $SU(2)_L \otimes U(1)_Y$, and to the fermions with a Yukawa coupling. In fact, in order to preserve the chiral symmetry of the electroweak interaction, one cannot insert trivial mass terms $m(\psi^\dagger_L \psi_R + \psi^\dagger_R \psi_L)$ (manifestly not gauge-invariant for example under $SU(2)_L$) neither for fermions nor for vector bosons. An alternative mechanism is then needed to insert the masses, and the most credited

one is the Higgs mechanism. It starts from the following Lagrangian for a complex doublet of scalar fields:

$$L = (D_\mu \phi)^\dagger (D^\mu \phi) + \mu^2 \phi^\dagger \phi - \lambda (\phi^\dagger \phi)^2 \tag{1.1}$$

that involves also the self-interaction term $\lambda(\phi^\dagger\phi)^2$. When the mass parameter μ^2 becomes negative, the potential has infinite minima lying in the complex plane for $|\phi| = \pm\sqrt{-\mu^2/\lambda}$. The symmetry breaking mechanism consists in the choice of one particular minimum (i.e. fixing the phase in the complex plane) that defines a vacuum expectation value (v.e.v) $\nu = \sqrt{-\mu^2/\lambda}$ for the Higgs field different from zero. Avoiding further technical details, in this way G_{SM} symmetry is broken and the effects are to reduce G_{SM} to the residual symmetry $SU(3)_C \otimes U(1)_{EM}$ and to give a mass to the intermediate vector bosons.
In order to make contact with measurable quantities, one is lead to introduce the physical basis for the gauge fields obtained by the mixing between the bosons W^j_μ and B_μ:

$$W^\pm_\mu = (W^1_\mu \pm W^2_\mu)/\sqrt{2} \tag{1.2}$$

$$Z^0_\mu = \sin\theta_W B_\mu - \cos\theta_W W^3_\mu \tag{1.3}$$

$$\gamma_\mu = \cos\theta_W B_\mu + \sin\theta_W W^3_\mu \tag{1.4}$$

and their respective masses:

$$m_W = g_2 v/\sqrt{2} \tag{1.5}$$

$$m_Z = m_W/\cos\theta_W \tag{1.6}$$

where $tan\theta_W = g_1/g_2$ represents the ratio between the two coupling constants for the bosons B_μ and W^j_μ. According to the spontaneous symmetry breaking pattern foreseen by the Higgs mechanism, the photon γ_μ is massless.
The Higgs boson mass is $m_H = \sqrt{-2\mu^2}$, while the Yukawa coupling with fermions gives them a mass proportional to the v.e.v of the Higgs ν and to their coupling constant with the Higgs field.

Hence the SM depends on the following 19 free parameters:

- The three coupling constants g_1,g_2 (or $sin\theta_W$) and g_3;
- The 9 Yukawa couplings with fermions;
- The 2 parameters of the Higgs potential: μ^2 (or m_H or ν) and λ;
- The three angles and the phase (to parametrise the CP violation in the SM) of the CKM matrix (Cabibbo-Kobayashi-Maskawa);
- The θ_{QCD} parameter describing the CP violation in the strong interaction Lagrangian.

1.2 Beyond the Standard Model

1.2.1 The limits of the Standard Model

The Standard Model, and in particular the electroweak theory, have been heavily tested in the last 30 years, without finding any significant failure in its predictions. Hence, the motivations to consider the SM as an "effective theory" are essentially related to its mathematical structure, rather than to its capacity to predict the physical processes. Some of these motivations are listed here.

- The hierarchical problem
  The problem is strongly related to the structure of the Higgs scalar field. As explained above, the mass of the Higgs boson is $m_H^0 = \sqrt{-2\mu^2}$ at the tree level, but, during the renormalisation process, the value of the mass parameter μ^2 is corrected by a factor $\delta\mu^2$ that comes from the loop-corrections. The physical parameter is then $\mu^2 = \mu_0^2 + \delta\mu^2$ indicating μ_0^2 the tree-level value, while the dependency of $\delta\mu^2$ from the cut-off scale Λ is quadratic. It follows that the correction to the Higgs mass $\delta m_H^2 = c\Lambda^2$ is itself proportional to Λ^2 that is independent to the tree-level value and especially quadratically divergent with the cut-off scale. If one wants that the physical value of the Higgs mass will be of the order of the electroweak scale keeping the Higgs sector as explained above and if one wants that the SM will be extended until some unification scale (i.e. $\Lambda = 10^{15}$ GeV) one needs to have a fine-tuning for the c constant until 10^{-28}!!
- The Dark matter problem
  The recent cosmological observations suggest that about 25% of the energy of the Universe comes from the Dark Matter. Keeping these results as reliable, the SM does not have any candidate to explain which are the constituents of this Dark matter (i.e. a massive, electrically neutral and weakly interacting particle).

- The unification problem
  Starting from the "global SM electroweak fit", the running coupling constants for the three interactions (strong, electromagnetic and weak) do not converge to a single value when one extrapolates them towards the Planck scale, contrasting any theory that foresees the unification of the forces.

There are several other problems not mentioned here (neutrino masses, matter-antimatter asymmetry, fermion masses hierarchy, etc..), but all of them lead to the idea that the SM is an "effective theory" that works fine at the electroweak scale, when it is extended to higher energy.

1.3 The Supersymmetry

The Supersymmetry (SUSY) [3] is one of the most favourite candidates to extend the SM, solving many of the problems explained above. Proposed during the 70's, this theory introduces a new symmetry, in addition to those of the SM, that associates a fermionic (bosonic) partner to each SM boson (fermion). The generators of this new symmetry are the Majorana spinors Q_α (α = 1,...,4) that act on the physical states changing their spin of a quantity $\pm 1/2$.
This fermionic generators satisfy the following relations:

$$[Q_\alpha, M^{\mu\nu}] = i(\sigma^{\mu\nu})^\beta_\alpha Q_\beta \tag{1.7}$$

$$\{Q_\alpha, \bar{Q_\beta}\} = -2(\gamma_\mu)_{\alpha\beta} P^\mu \tag{1.8}$$

$$[Q_\alpha, P^\mu] = \{Q_\alpha, Q_\beta\} = \{\bar{Q_\alpha}, \bar{Q_\beta}\} = 0 \tag{1.9}$$

with

$$\sigma_{\mu\nu} = \frac{1}{4}[\gamma_\mu, \gamma_\nu] \tag{1.10}$$

$$\bar{Q_\alpha} = Q^T_\alpha \gamma^0 \tag{1.11}$$

where γ_μ are the usual 4x4 Dirac matrices, P^μ is the momentum operator and $M^{\mu\nu}$ is the Lorentz group generator.
In the Minimal Supersymmetric extension of the Standard Model (MSSM), each chiral fermion $f_{L,R}$ has a scalar sfermion partner $\tilde{f}_{L,R}$, and each massless gauge boson A_μ, with two helicity states ± 1, has a massless spin 1/2 gaugino partner with helicities $\pm 1/2$. In order to avoid triangular anomalies, there must also be two complex Higgs doublets and their associated Higgsinos. The interactions of SUSY particles are basically obtained from the Standard Model ones, by replacing any two lines in a vertex by their SUSY

partners; for example, the gluon-quark-quark and gluino-quark-squark couplings are the same. See [4] for the construction of the complete Lagrangian. SUSY provides a solution to the hierarchy problem because it implies an equal number of bosons and fermions, which give opposite signs in loops and so cancel the quadratic divergences. This cancellation works to all orders: since the masses of fermions are only logarithmic divergent, this must also be true for boson masses in a supersymmetric theory. When SUSY is broken, the corrections to the Higgs and other scalar masses become proportional to the SUSY mass scale, rather than the Planck scale. If the Higgs is to be light without unnatural fine tuning, then the SUSY particles should have masses below about 1 TeV.

SUSY must of course be broken, since superparticles have not been observed: there is certainly no spin-0 selectron degenerate with the electron. Gauge invariance forbids mass terms in the Lagrangian for all Standard Model particles; masses can be introduced only by spontaneous symmetry breaking, using the Higgs mechanism. In contrast, mass terms are allowed for all the SUSY particles. Thus, it is possible to parametrise SUSY breaking by introducing by hand SUSY-breaking mass terms for the squarks, sleptons, Higgsinos, and gauginos. Additional soft terms (bilinear B terms and trilinear A terms with dimension $d < 4$) consistent with gauge invariance can also be added without reintroducing quadratic divergences. Finally, a Higgsino mass term must be included; this must be of the same order as the SUSY breaking terms even though it is SUSY conserving.

The requirements of gauge invariance and renormalisability are sufficient to guarantee that the Standard Model Lagrangian conserves baryon and lepton number. In supersymmetric theories it is possible to violate both, potentially leading to disastrous weak-scale proton decay. The unwanted terms can be eliminated by imposing invariance under R-parity,

$$R = (-1)^{3(B-L)+2S} \tag{1.12}$$

where B, L, and S are respectively the baryon number, the lepton number, and the spin. Hence $R = +1$ for all Standard Model particles and $R = -1$ for all SUSY particles. This has the consequence that SUSY particles must be produced in pairs and that the lightest SUSY particle (LSP) is absolutely stable. R-parity conservation holds automatically in many GUT models under rather general assumptions [5]. Weak-scale proton decay can also be avoided by imposing either baryon or lepton number conservation.

1.3.1 The MSSM: Minimal Supersimmetric Standard Model

The Minimal Supersymmetric Standard Model (MSSM) is the supersymmetric extension of the SM with the minimal particle content, as listed in

Table 1.1: Chiral supermultiplets in the Minimal Supersymmetric Standard Model. The squarks and sleptons come in three generations. The physical Higgs bosons after symmetry breaking are h, H, A, and $H^{\pm}$.

Name	**Spin 0**	**Spin 1/2**	$SU(3) \otimes SU(2) \otimes U(1)$
squarks, quarks	$\tilde{Q} = (\tilde{u}_L, \tilde{d}_L)$ $\tilde{u}^*_R$ $\tilde{d}^*_R$	$Q = (u_L, d_L)$ $\bar{u}_R$ $\bar{d}_R$	(3, 2, 1/6) ($\bar{3}$, 1, -2/3) ($\bar{3}$, 1, 1/3)
sleptons, leptons	$\tilde{L} = (\tilde{\nu}, \tilde{e}_L)$ $\tilde{e}^*_R$	$L = (\nu, e_L)$ e_R	(1, 2, -1/2) (1, 1, 1)
Higgs, Higgsinos	$H_u = (H_u^+, H_u^0)$ $H_d = (H_d^0, H_d^-)$	$\tilde{H}_u = (\tilde{H}_u^+, \tilde{H}_u^0)$ $\tilde{H}_d = (\tilde{H}_d^0, \tilde{H}_d^-)$	(1, 2, 1/2) (1, 2, -1/2)

Table 1.2: Vector supermultiplets in the Minimal Supersymmetric Standard Model. After symmetry breaking, the winos and bino mix with the Higgsinos to give four neutralinos $\tilde{\chi}_i^0$ and two charginos $\tilde{\chi}_i^{\pm}$, and the W^0 and B mix as in the Standard Model.

Name	**Spin 1/2**	**Spin 1**	$SU(3) \otimes SU(2) \otimes U(1)$
gluino, gluon	$\tilde{g}$	g	(8, 1, 0)
winos, W's	$\tilde{W}^{\pm}$, $\tilde{W}^0$	$W^{\pm}$, W^0	(1, 3, 0)
bino, B	$\tilde{B}$	B	(1, 1, 1)

Table 1.1 and 1.2, with R-parity conservation.

The cancellation of quadratic divergences for scalar masses only requires Supersymmetry for the terms with mass dimension four. In the MSSM, SUSY is broken "by hand" by adding to the Lagrangian all possible soft terms consistent with $SU(3) \otimes SU(2) \otimes U(1)$ gauge invariance. This includes

mass terms for all the superpartners and trilinear A terms:

$$\begin{aligned} L_{SOFT} = \quad & -m_{H_d}^2|H_d|^2 - m_{H_u}^2|H_u|^2 + \mu B\epsilon_{ij}(H_d^i H_u^j + h.c) \\ & -\frac{1}{2}M_1\tilde{\bar{B}}\tilde{B} - \frac{1}{2}M_2\tilde{\bar{W}}\tilde{W} - \frac{1}{2}M_1\tilde{\bar{g}}\tilde{g} \\ & -M_{\tilde{Q}}^2(\tilde{u}_L^*\tilde{u}_L + \tilde{d}_L^*\tilde{d}_L) - M_{\tilde{U}}^2 u_R^* u_R - M_{\tilde{D}}^2 d_R^* d_R \\ & -M_{\tilde{L}}^2(\tilde{l}_L^*\tilde{l}_L + \tilde{\nu}_L^*\tilde{\nu}_L) - M_{\tilde{E}}^2 l_R^* l_R \\ & -\epsilon_{ij}(-\lambda_u A_u H_u^i \tilde{Q}^j \tilde{u}_R^* + \lambda_d A_d H_d^i \tilde{Q}^j \tilde{d}_R^* + \lambda_l A_E H_d^i \tilde{L}^j \tilde{l}_R^* \end{aligned} \tag{1.13}$$

where Q, L, H_u and H_d denote $SU(2)$ weak doublets as in Table 1.1 and a summation over generations is implied. All the parameters are in general matrices in flavour space and complex; there are a total of 105 new parameters [6] in addition to the SM ones. One of these is the SUSY-conserving Higgsino mass μ, which must be of the same order as the SUSY breaking masses. Electroweak symmetry cannot be broken by hand in a similar way, since this would destroy gauge invariance. Instead it is broken by the Higgs mechanism as previously explained giving rise to masses for quarks, leptons, W and Z bosons. SUSY requires two Higgs doublets and relates the Higgs self-coupling to gauge couplings:

$$\begin{aligned} V_{Higgs} = \quad & (m_{H_d}^2 + \mu^2)|H_d|^2 + (m_{H_u}^2 = \mu^2)|H_u|^2 - B\mu(\epsilon_{ij}H_d^i H_u^j + h.c) \\ & +\frac{1}{8}(g^2 + g'^2)(|H_d|^2 - |H_u|^2)^2 + \frac{1}{2}g^2|H_d^{*i}H_u^i|^2 \end{aligned} \tag{1.14}$$

Once SUSY and the electroweak symmetry are broken, particles with the same quantum numbers will general mix. The gauginos and Higgsinos mix to form two spin 1/2 charged particles called "charginos" $\tilde{\chi_i^{\pm}}$ with the matrix in the (W^+,H^+) basis:

$$\begin{pmatrix} m_2 & \sqrt{2}M_W sin\beta \\ \sqrt{2}M_W cos\beta & \mu \end{pmatrix}$$

and four spin-1/2 neutral particles called "neutralinos" $\tilde{\chi_i^0}$ with the mass matrix in the (B, W^0, H_d, H_u) basis:

$$\begin{pmatrix} m_1 & 0 & -M_Z cos\beta sin\theta_W & M_Z sin\beta sin\theta_W \\ 0 & m_2 & M_Z cos\beta cos\theta_W & M_Z sin\beta cos\theta_W \\ -M_Z cos\beta sin\theta_W & M_Z cos\beta cos\theta_W & 0 & -\mu \\ M_Z sin\beta sin\theta_W & -M_Z sin\beta cos\theta_W & -\mu & 0 \end{pmatrix}$$

where, in both formulae, θ_W is the Weinberg angle and $tan(\beta)$ is the ratio of the two v.e.v's of the two Higgs doublets.

The phenomenology of the different SUSY models strongly depends on this mixing, but in many of these models one can write the following relation:

$$\frac{M_1}{\alpha_1} = \frac{M_2}{\alpha_2} = \frac{M_3}{\alpha_3} \tag{1.15}$$

with the mass term μ that is of order of $M_{\tilde{g}}$. So that the two lighter neutralinos and the lighter chargino are dominantly gaugino, while the heavier states are dominantly Higgsino and weakly coupled to the first two generations.
Concerning the sfermion sector, due to the fact that chiral fermions f_L, f_R must have the same mass by Lorentz invariance, their super-partners $\tilde{f}_L$, $\tilde{f}_R$ are scalars with separate masses. Their squared mass matrix also gets off-diagonal contributions proportional to the fermion mass with the result that this left-right mixing is mainly important for the third generation. These eigenstates are called $\tilde{t}_{1,2}$, $\tilde{b}_{1,2}$ and $\tilde{\tau}_{1,2}$ (stop, sbottom and stau), while the mixing for the first two generations is negligible.
These are the features common to nearly all the SUSY models; in the next subsection, I will explain some particular model before to concentrate on mSUGRA model, that is the framework within this work is developed.

1.3.2 Particular SUSY models

Clearly it is not possible to explore the complete parameter space of the MSSM; in the absence of experimental help some theoretical prejudice must be imposed. Presumably Supersymmetry should be broken spontaneously rather than by hand, and should be unified with gravity. It does not seem possible to construct a phenomenologically acceptable model, with spontaneous Supersymmetry breaking, using only the MSSM fields. Instead, it is necessary to introduce a hidden sector to break SUSY and then to communicate the breaking to the MSSM sector using some messenger interaction that couples to both. In supergravity (SUGRA) models, gravity is the unique messenger[7]. Then the MSSM masses are scaled by the Planck scale, $M_{MSSM} \approx \frac{F}{M_P}$ so the SUSY breaking scale in the hidden sector must be roughly $F \approx (10^{11}\text{GeV})^2$. This model will be further discussed in the next section.
It is also possible that the SUSY breaking scale in the hidden sector is $F_m << (10^{11}\text{GeV})^2$ and that the MSSM particles get masses through $SU(3) \otimes SU(2) \otimes U(1)$ gauge interactions at a messenger scale $M_m << M_P$. This is known as Gauge Mediated Supersymmetry Breaking (GMSB)[8] . Since the gravitino $\tilde{G}$ gets its mass only through gravitational interactions, it is much lighter than all the MSSM particles, which eventually decay into it. In the minimal GMSB model, the MSSM masses are proportional to $\Lambda = \frac{F_m}{M_m}$; the

gaugino masses are proportional to the number of messenger fields N_5, while the scalar masses are proportional to $\sqrt{N_5}$. The phenomenology is determined by whether the next to lightest SUSY particle (NLSP) is a $\tilde{\chi}_1^0$ or a $\tilde{\tau}_1$ and by whether the NLSP decay $\tilde{\chi}_1^0 \to \tilde{G}\gamma$ or $\tilde{\tau}_1 \to \tilde{G}\tau$ occurs promptly or outside the detector. Signatures for the long-lived $\tilde{\chi}_1^0$ case are qualitatively similar to those for SUGRA, but the other three cases are quite different.
Finally, R parity may be broken, although there are strong constraints on many of the R-violating couplings[10]. If the R-violating couplings are small, then the main effect is to allow the LSP to decay, violating either baryon number, e.g. $\tilde{\chi}_1^0 \to qqq$, or lepton number, e.g. $\tilde{\chi}_1^0 \to l^+l^-\nu$, but of course not both baryon and lepton number, since that would give rapid proton decay.
Even if the general MSSM is correct, none of these models is likely to be the whole truth, but they do provide self-consistent frameworks in which to test the ability of the ATLAS detector to study Supersymmetry at the LHC. Discovery of signals for any of these at the LHC is straightforward. The main problem is not to distinguish SUSY from the Standard Model (that should be possible already with low statistic) but to separate the many SUSY processes that occur and try to exclude the models that cannot explain the phenomenology. This argument is however absolutely out of the goals of this work that will be focused on the possibility to discover the Supersymmetry in the mSUGRA scenario with early data.

1.4 The mSUGRA model

The minimal supergravity (SUGRA) model[7] assumes that at the GUT scale all scalars (squarks, sleptons, and Higgs bosons) have a common mass m_0 , all gauginos and Higgsinos have a common mass $m_{1/2}$, and all the trilinear Higgs-sfermion-sfermion couplings have a common value A_0. Such common masses are suggested by the fact that gravity is universal, but are sometimes not found in models with realistic GUT-scale dynamics. The remaining parameters at the GUT scale are the bilinear SUSY breaking term B and the SUSY conserving Higgs mass μ. These masses are split when they are run down to the weak scale with the RGE's (Renormalisation Group Equations)[9]. These equations are 26 and are then solved iteratively between the weak and GUT scale. On each iteration the SUSY masses are calculated and used to determine the thresholds at which the masses and other parameters are frozen. Because of the specific form of the RGE's, the squared mass of the Higgs field is driven negative by the large top Yukawa coupling, causing electroweak symmetry breaking at around 100 GeV, but leaving unbroken the colour and electromagnetic interactions. This

mechanism is called ElectroWeak Radiative Symmetry Breaking (EWRSB) because the symmetry is broken in a dynamical way, simply evolving the running coupling constants up to the electroweak scale.
Then B and μ^2 can be eliminated in favour of $sgn\mu = \pm 1$ and the ratio $\tan\beta = \frac{\nu_u}{\nu_d}$ of Higgs vev's. The parameters defining this minimal model are therefore:

$$m_0, m_{1/2}, A_0, \tan\beta, sgn\mu = \pm 1 \tag{1.16}$$

Due to the large difference between the Planck and the electroweak scale, the phenomenology foreseen by the model is very sensible to the precision with which the SM parameters are known. Hence it is usual to insert the top mass as a sixth parameter of the model because its precision is, for example, three order of magnitude worse than the one on the Z mass.
Within this six dimensional parameter space, there are some regions that are forbidden by several constraints coming from theoretical or experimental motivations. The main theoretical constraint is, obviously, the resolvability of the RGE's equation in such a way that electroweak symmetry is broken at the expected scale. Instead, the experimental constraints can come from the direct searches of Supersymmetry at the colliders (Tevatron and LEP), that will be shown in the next section or from indirect searches. In this last category the principal constraints are on the LSP mass (from the measurements on the density of the cold dark matter in the Universe, supposing that the LSP is the constituent of the cold dark matter), on the branching ratio of the decay $b \to s\gamma$ (for the low mass SUSY scale), on the proton lifetime (especially for the R-parity violating models where it is too short) and on the Flavour Changing Neutral Currents processes (that are usually too large in some regions).

1.5 Experimental searches on Supersymmetry

In order to understand the typical scenarios where the searches have been developed, one has to focus on the experimental signatures that characterise the SUSY phenomenology. As explained above, there are several possible scenarios that are strongly dependent on the model, but I will try to focus here on the most common features belonging to a large number of these models.
The principal feature that allows to distinguish the supersymmetric signals from the SM ones is the existence of the LSP (Lightest Supersymmetric Particle). In the R-parity conserving models (for example mSUGRA or GMSB), this LSP is neutral, stable and weakly or gravitationally interacting and then is detectable only through a large amount of E_T^{MISS}, which is the missing energy in the transverse plane with respect to the beam direction,

calculated starting from the deposits of energy in the calorimeters. The only SM processes that can give this kind of signature are those involving the production of neutrinos. Other useful signatures are those with isolated and energetic leptons or photons associated with an important hadronic activity. This kind of signature will be deeply studied in the next chapters in the mSUGRA scenario.
On the other hand, in the R-parity violating models, also the LSP decays and then the signatures are characterised through an excess of leptons and hadronic jets.

1.5.1 Searches at the colliders

LEP searches

At LEP, 180pb^{-1} at $\sqrt{s}$ =189 GeV, 80pb^{-1} at $\sqrt{s} < 206$ GeV and 140pb^{-1} between $\sqrt{s}$ =206 GeV and $\sqrt{s}$ =209 GeV have been collected. In the runs at the Z mass peak, the searches for SUSY have been performed looking for its contributions to the Z width, but nothing different from the SM has been found, so that only lower limits on the SUSY masses have been fixed. At higher energies, the processes involving SUSY particles decaying in SM or LSP particles have been studied using the signature lepton+jets+E^{MISS}. The main backgrounds to this channel are essentially two: the two photon interactions and the four fermions events. Both these channels are characterised by a significant amount of fake or real E^{MISS}, that can mimic the SUSY signatures.
The first background comes from two photons emitted by the electrons of the beam. The two photons interact creating a leptonic or hadronic system with low invariant mass. The decay products of this system are nearly collinear to the beam direction and then are not detected, contributing to the missing energy.
The second background comes from the WW and ZZ events, where the two bosons decay leptonically producing leptons (not detected) and neutrinos.
Cutting on E^{MISS}, these backgrounds can be strongly reduced (especially the two photons background), but if the difference in mass ΔM between the LSP and the NLSP (Next to the Lightest Supersymmetric Particle) is about 10 GeV/c^2, the analysis becomes more problematic. The resulting limits on the masses in the various sectors of the MSSM are summarised in Table 1.3.

TEVATRON searches

The two experiments running at TEVATRON (CDF and D$\varnothing$) collected in the RUN I a statistic of 110 pb^{-1} at $\sqrt{s} = 1.8$ TeV, while in the RUN II,

Table 1.3: Lower limits to the masses of SUSY particles at LEP. GMSB means a general model where the Supersymmetry is broken by a gauge interaction, while RPV means a general model with R-parity violation. The other results are intended in the general MSSM framework.[11]

Particle	Condition	Limit(GeV/c^2)	Source
$\chi_1^{\pm}$	$m_{\tilde{\nu}} > 200$GeV/c^2	103	LEP2
	$m_{\tilde{\nu}} > m_{\tilde{\chi}^{\pm}}$	85	LEP2
	any $m_{\tilde{\nu}}$	45	Z Width
	$M_2 < 1$TeV/c^2	99	LEP2
	RPV	88	LEP2
χ_1^0	any tanβ, $m_{\tilde{\nu}} > 500$GeV/c^2	39	LEP2
	any tanβ, any m_0	36	LEP2
	GMSB	93	LEP2 combined
	RPV	23	LEP2
$\tilde{e}_R$	$\Delta M > 10$GeV/c^2	99	LEP2 combined
$\tilde{\mu}_R$	$\Delta M > 10$GeV/c^2	95	LEP2 combined
$\tilde{\tau}_R$	$M_{\chi_0^1} > 10$GeV/c^2	80	LEP2 combined
$\tilde{\nu}$		43	Z Width
$\tilde{\mu}_R$, $\tilde{\tau}_R$	stable	86	LEP2 combined
$\tilde{t}_1$	any θ_{mix}, $\Delta M > 10$GeV/c^2	95	LEP2 combined
	any θ_{mix}, any ΔM	59	ALEPH
$\tilde{t}_1 \to bl\tilde{\nu}$	any θ_{mix}, $\Delta M > 7$GeV/c^2	96	LEP2 combined

actually ongoing at $\sqrt{s} = 1.96$ TeV, a statistic of about 4 fb^{-1} (even if the more recent analyses have been performed with an integrated luminosity of 3 fb^{-1}). Here the production of SUSY particles is dominated by the strong interacting sparticles, i.e. squarks and gluinos, that are produced in pairs and decay via the gauginos until the two LSP ($\tilde{\chi}_1^0$ or $\tilde{G}$). An additional problem, with respect to the physics of LEP, comes from the uncertainties on the parton density functions (PDF's). The spread of partonic energies is very large, so one has to consider the possible presence of several SUSY signals in one data set. A search in a given topology, such as ≥ 3 jets+E_T^{MISS}, can capture events from squarks, gluinos and even gauginos, with or without cascade decays. Applying experimental bounds on one production mechanism ignoring the other ones would be invalid, so the two experiment have chosen a relatively simple way to organise the phenomenology turning to the

mSUGRA framework, because its fundamental parameters m_0 and $m_{1/2}$ can be fairly easily related to the squark, gluino and gaugino masses which determine the event kinematics and hence the signal acceptance.
These experiments can profit of the larger production cross sections with respect to LEP because it is an hadronic collider, but also the backgrounds are several order of magnitude larger due to the hadronic activity. These backgrounds are essentially of two types. First, ordinary multijet events can appear to have missing energy due to measurement errors. While large mis-measurements are rare, there are very many di-jet and tri-jet "QCD" events that anyway can be estimated directly from control samples. Second, much rarer processes yield energetic neutrinos which produce a genuine missing energy signature, essentially from the production of the W and Z bosons with initial-state radiation, of the boson pairs or of the top quark. Estimates for these backgrounds commonly are based on theoretical cross sections, although in some analyses direct measurements are used to reduce the uncertainties of the Monte Carlo.
A brief sketch of the resulting limits on the masses in the various sectors of the MSSM is summarised in Table 1.4.

Table 1.4: Lower limits to the masses of SUSY particles at Tevatron. GMSB means a general model where the Supersymmetry is broken by a gauge interaction. The other results are intended in the general MSSM framework.[11]

Particle	Condition	Limit(GeV/c^2)	Source
$\chi_1^{\pm}$	GMSB	150	D$\varnothing$ isolated photons
$\tilde{t}_1$	any θ_{mix}, $M_{\tilde{\chi}_1^0} \approx \frac{1}{2} M_{\tilde{t}}$	115	CDF
$\tilde{g}$	any $M_{\tilde{q}}$	195	CDF jets + E_{MISS}^T
$\tilde{q}$	$M_{\tilde{q}} \approx M_{\tilde{g}}$	300	CDF jets + E_{MISS}^T

1.5.2 Limits from the cosmology

One of the strongest motivation for the Supersymmetry is that it foresees a candidate for the Dark Matter (i.e. the LSP, usually the lightest neutralino). Hence the cosmological constraints represent a kind of "reasonable limits" on the parameter space that should be taken into account.
The existence of the Dark Matter is by now well established, and the currently most accurate (even if indirect) determination of its density Ω_{DM} comes from global fits of cosmological parameters to a variety of observa-

tions. For example, using measurements of the anisotropy of the Cosmic Microwave Background (CMB) and of the spatial distribution of galaxies, one finds a density of cold, non-baryonic matter

$$\Omega_{nbm}h^2 = 0.111 \pm 0.006 \tag{1.17}$$

where h is the Hubble constant in units of 100 Km/(s $\cdot$ Mpc).
The upper bound[12] on the contribution of light neutrino (SM-like) is

$$\Omega_\nu h^2 \leq 0.0076 \quad 95\% CL \tag{1.18}$$

so the constituents of this DM must come from non SM particles. There are several possible candidates: primordial black-holes, axions and WIMP's (Weakly Interacting Massive Particles). I will briefly focus on this last category because strongly related with mSUGRA models.
The WIMP's χ are particles with mass roughly between 10 GeV and a few TeV and with cross sections of approximately weak strength. Their present relic density can be calculated reliably if the WIMP's were in thermal and chemical equilibrium with the hot "soup" of SM particles after the inflation. In this case their density would become exponentially (Boltzmann) suppressed at $T < m_\chi$. The WIMP's therefore drop out of the thermal equilibrium ("freeze out" phase) once the rate of reactions that change SM particles into WIMP's and vice versa, becomes smaller than the Hubble expansion rate of the Universe. The rate is proportional to the product of the WIMP's number density and the WIMP pair annihilation cross section into SM particles σ_A times the velocity. So that, the present relic density is then approximately given by[13]

$$\Omega_\chi h^2 \approx const \cdot \frac{T_0^3}{M_{PL}^3 < \sigma_A v >} \approx \frac{0.1\text{pb} \cdot \text{c}}{< \sigma_A v >} \tag{1.19}$$

where T_0 is the current CMB temperature, M_{PL} is the Planck mass, c is the speed of light, σ_A is the total annihilation cross section of a pair of WIMP's into SM particles, v is the relative velocity between two WIMP's in their cms system and $< ... >$ denotes the thermal averaging. Freeze out happens at temperature $T_F \approx m_\chi/20$ almost independently of the properties of the WIMP, and this means that the WIMP's are already non-relativistic when they decouple from the thermal plasma.
This fact has many consequences that are not explained here, but one of these is to exclude heavy neutrinos described by SU(2) doublet as in the SM, because its relic density is too small if the mass is larger than $M_Z/2$, as required by LEP data.
The currently best motivated WIMP candidate is therefore the LSP in the

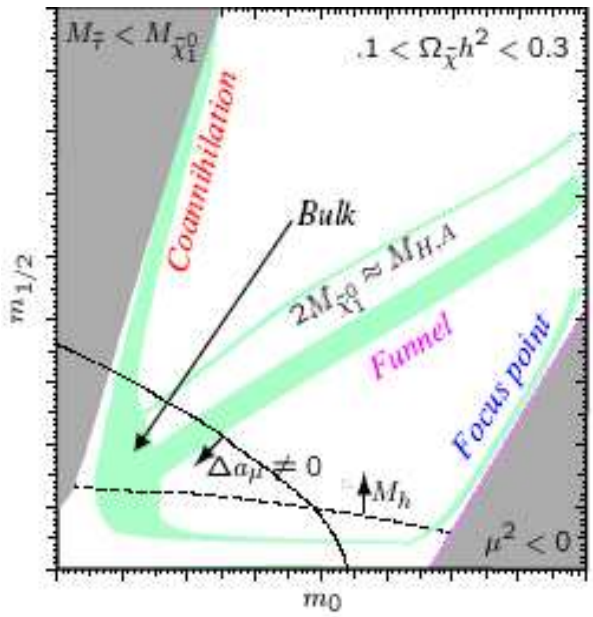

Figure 1.1: Qualitative picture of the mSUGRA (m_0, $m_{1/2}$) plane, for fixed values for $A_0 = 0$, $sgn\mu > 0$ and $tan\beta = 50$. The four "cosmologically allowed regions" are shown in green, together with the limits on the Higgs mass fixed by LEP (dashed line) and on the anomalous magnetic moment of the muon $\Delta\alpha_\mu$ (dashed-dotted line). These two limits aim to exclude the low mass regions of the plane. The grey regions are instead excluded by imposing the neutrality of the LSP (left region) or the resolvability of the RGE's assuring the Electroweak Symmetry Breaking (right region).

R-parity conserving models[14], and the possibilities are essentially two: sneutrino or lightest neutralino. The first one is excluded by the largest cross section, unless the neutrino mass is several hundreds of GeV/c^2, that is uncomfortable in view of naturalness arguments.
The most studied candidate is then the lightest neutralino, and detailed calculations[15] show that there are at least four distinct regions of parameter space, where the relic thermal density is compatible with the data. All these regions, represented in Fig.1.1, are joined by the existence of some annihilation process that reduces the relic thermal density and in particular:

- **Bulk region** Low m_0 and $m_{1/2}$ region near to the region of the parameter space excluded by LEP data. In this region there are the largest cross sections of the "allowed" parameter space.

- **Coannihilation region** Low m_0 region where the relic density is lower due to the $\tilde{\chi} - \tilde{\tau}$ annihilation favoured by the fact that $m_{\tilde{\chi}} \approx m_{\tilde{\tau}}$

- **Focuspoint region** Low $m_{1/2}$ and high m_0 region where the mixing matrix of the gauginos is such that the lightest neutralino is mostly higgsino. This increases the annihilation cross section via a virtual Z^0, and then brings the relic density within the cosmological constraints.

- **Funnel region** Region where the neutralinos have a mass about a half of one of the Higgs bosons mass, and so the $\tilde{\chi}$ annihilation process via the exchange of a virtual A^0 is enhanced putting the relic density within the limits.

The benchmark points chosen by ATLAS lie in these regions and are the signal samples that will be used in this thesis to estimate the SUSY discovery potential in the di-leptonic channel.

Bibliography

[1] For a theoretical approach: M.Kaku, Quantum field theory (1993) Oxford Press University;

[2] For an experimental approach: D.H.Perkins, Introduction to high energy physics (1999) Cambridge Press University;

[3] Y.Gol'fand e E.Likthman, JETP Lett. 13 (1971) 323;
D.Volkov e V.Akulov, Phys. Lett. 46B (1973) 109;
J.Wess e B.Zumino, Nucl. Phys. B70 (1974) e B78 (1975) 1

[4] General reviews of SUSY include H.P. Nilles, Phys. Rep. 111 (1984) 1;
H.E. Haber and G.L. Kane, Phys. Rep. 117 (1985) 75;
J. Wess and J. Bagger, Supersymmetry and Supergravity, ISBN 0691085560 (1992);
S.P. Martin, hep-ph/9709356 (1997).

[5] S.P.Martin, hep-ph/9602324, Phys Rev. D54 (1996) 2340;

[6] S.Dimopoulos and D.Sutter, Nucl. Phys. B452 (1995) 496;

[7] L. Alvarez-Gaume, J. Polchinski, and M.B. Wise, Nucl. Phys. B221 (1983) 495;
L. Ibanez, Phys. Lett. 118B (1982) 73;
J. Ellis, D.V. Nanopolous, and K. Tamvakis, Phys. Lett. 121B (1983) 123;
K. Inoue et al., Prog. Theor. Phys. 68 (1982) 927;
A.H. Chamseddine, R. Arnowitt, and P. Nath, Phys. Rev. Lett. 49 (1982) 970.

[8] M. Dine, W. Fischler and M. Srednicki, Nucl. Phys. B189 (1981) 575;
S. Dimopoulos and S. Raby, Nucl. Phys. B192 (1981) 353;
C. Nappi and B. Ovrut, Phys. Lett. 113B (1982) 175;
L. Alvarez-Gaume, M. Claudson, and M. Wise, Nucl. Phys. B207 (1982) 961;
M. Dine and A. Nelson, Phys. Rev. D48 (1993) 1227;
M. Dine, A. Nelson, and Y. Shirman, Phys. Rev. D51 (1995) 1362;
M. Dine, et al., Phys. Rev. D53 (1996) 2658.

[9] For the form of the RGE's used here, see V. Barger, M.S. Berger, and P. Ohmann, hep-ph/9311269, Phys. Rev. D49 (1994) 4908.

[10] H. Dreiner, hep-ph/9707435 (1997).

[11] W-M Yao et al. J. Phys G: Nucl. Part. Phys. Vol 33 (2006) 1
Sez. Supersymmetry, Part II(Experimental) p.1120 Available online on the site http://stacks.iop.org/JPhysG/33/1

[12] M.Boezio et al., Astroph. J. 532, 653 (1999);

[13] E.W.Kolb and M.E.Turner, "The early Universe", Addison-Wesley (1990);

[14] For a review, see G.Jungman, M.Kamionkowski and K.Griest, Phys. Reports 267, 195 (1996);

[15] See e.g. J.R.Ellis et al. Nucl. Phys. B652, 259 (2003);
J.R.Ellis at al. Phys. Lett. B565, 176 (2003);
H.Baer et al. JHEP 0306, 054 (2003);
A.Bottino et al., Phys. Rev. D68, 043506 (2003).

Chapter 2

The ATLAS detector

2.1 Introduction

The Large Hadron Collider (LHC) at CERN will extend the frontiers of particle physics with its unprecedented high energy and luminosity. Inside the LHC, at full performances, bunches of up to 10^{11} protons will collide 40 million times per second to provide 14 TeV proton-proton collisions at a design luminosity of $10^{34}\text{cm}^{-2}\text{s}^{-1}$. Obviously, it will take some years to achieve these performances, but the indications are that in the 2009 the collisions will be at 10 TeV in the center of mass. The LHC will also collide heavy ions, in particular lead nuclei, at 5.5 TeV per nucleon pair, at a design luminosity of $10^{27}\text{cm}^{-2}\text{s}^{-1}$. The high interaction rates, radiation doses, particle multiplicities and energies, as well as the requirements for precision measurements have set new standards for the design of particle detectors. Two general purpose detectors, ATLAS (A Toroidal LHC ApparatuS) and CMS (Compact Muon Solenoid) have been built for probing p-p and ion-ion collisions. [1]

2.2 Definitions and reference frames

The coordinate system and nomenclature used for describing the ATLAS detector and the particles emerging from the p-p collisions are briefly summarised here as they are used repeatedly throughout this thesis. The beam direction defines the z-axis and the x-y plane is transverse to the beam direction. The positive x-axis is defined as pointing from the interaction point to the centre of the LHC ring and the positive y-axis is defined as pointing upwards. The side-A of the detector is defined as that with positive z and side-C is that with negative z. The azimuthal angle ϕ is measured around the beam axis, and the polar angle θ is the angle from the beam axis. The

pseudorapidity is defined as $\eta = -ln(tan(\theta/2))$. The transverse momentum p_T, the transverse energy E_T, and the missing transverse energy E_T^{MISS} are defined in the x-y plane unless stated otherwise. The distance ΔR in the pseudorapidity-azimuthal angle space is defined as $\Delta R = \sqrt{(\Delta\eta)^2 + (\Delta\phi)^2}$.

2.3 Physics requirements and detector overview

LHC will provide a rich physics potential, ranging from more precise measurements of Standard Model parameters to the search for new physics phenomena. Requirements for the ATLAS detector system [3] have been defined using a set of processes covering much of the new phenomena which one can hope to observe at the TeV scale. The high luminosity and increased cross-sections with respect to the TEVATRON enable further high precision tests of QCD, electroweak interactions, and flavour physics. The top quark will be produced at the LHC at a rate of a few Hz, providing the opportunity to test its couplings and spin. The search for the Standard Model Higgs boson has been used as a benchmark to establish the performance of important sub-systems of ATLAS. This process is particularly demanding in term of detector performances since there is a range of production and decay mechanisms, depending on the mass of the Higgs boson, H. At low masses ($m_H < 2m_Z$), the natural width would only be a few MeV, and so the observed width would be defined by the instrumental resolution. The predominant decay mode into hadrons would be difficult to detect due to QCD backgrounds, and the two-photon decay channel would be an important one. Other promising channels could be, for example, associated production of H such as $t\bar{t}H$, WH, and ZH, with $H \to b\bar{b}$, using a lepton from the decay of one of the top quarks or of the vector boson for triggering and background rejection. For masses above 130 GeV, Higgs-boson decays, $H \to ZZ$, where each Z decays to a pair of oppositely charged leptons, would provide the experimentally cleanest channel to study the properties of the Higgs boson. For masses above approximately 600 GeV, WW and ZZ decays into jets or involving neutrinos would be needed to extract a signal. Searches for the Higgs boson beyond the Standard Model, for such particles as the A and $H^{\pm}$ of the Minimal Supersymmetric extension of the Standard Model (MSSM), require sensitivity to processes involving τ-leptons and good b-tagging performance. Should the Higgs boson be discovered, it would need to be studied in several modes, regardless of its mass, in order to fully disentangle its properties and establish its credentials as belonging to the Standard Model or an extension thereof.

The decays of supersymmetric particles, as said in Chapter 1, such as squarks and gluinos, would involve cascades which, if R-parity is conserved,

always contain a lightest stable supersymmetric particle (LSP). As the LSP would interact very weakly with the detector, the experiment would measure a significant missing transverse energy, E^T_{MISS} , in the final state. The rest of the cascade would result in a number of leptons and jets. In schemes where the LSP decays into a photon and a gravitino, an increased number of hard isolated photons is expected. Several new models propose the existence of extra dimensions leading to a characteristic energy scale of quantum gravity in the TeV region. In terms of experimental signatures, this could lead to the emission of gravitons which escape into extra dimensions and therefore generate E_T^{MISS} or of Kaluza-Klein excitations which manifest themselves as Z-like resonances with a separations in mass of order of TeV. Other experimental signatures could be anomalous high-mass di-jet production, and miniature black-hole production with spectacular decays involving democratic production of fundamental final states such as jets, leptons, photons, neutrinos, W and Z.

The formidable LHC luminosity and resulting interaction rate are needed because of the small cross-sections expected for many of the processes mentioned above. However, with an inelastic proton-proton cross-section of 80 mb, the LHC will produce a total rate of 10^9 inelastic events/s at design luminosity. This presents a serious experimental difficulty as it implies that every candidate event for new physics will on the average be accompanied by 23 inelastic events per bunch crossing. The nature of proton-proton collisions imposes another difficulty. QCD jet production cross sections dominate over the rare processes mentioned above, requiring the identification of experimental signatures characteristic of the physics processes in question, such as E_T^{MISS} or secondary vertexes. Identifying such final states for these rare processes imposes further demands on the integrated luminosity needed, and on the particle-identification capabilities of the detector. Viewed in this context, these benchmark physics goals can be turned into a set of general requirements for the LHC detectors:

- Due to the experimental conditions at the LHC, the detectors require fast, radiation-hard electronics and sensor elements. In addition, high detector granularity is needed to handle the particle fluxes and to reduce the influence of overlapping events.

- Large acceptance in pseudorapidity with almost full azimuthal angle coverage is required.

- Good charged-particle momentum resolution and reconstruction efficiency in the inner tracker are essential. For offline tagging of τ-leptons and b-jets, vertex detectors close to the interaction region are required to observe secondary vertexes.

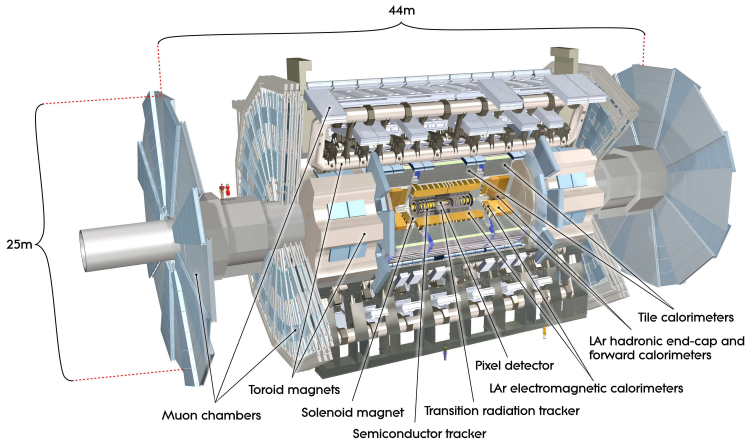

Figure 2.1: Cut-away view of the ATLAS detector. The dimensions of the detector are 25 m in height and 44 m in length. The overall weight of the detector is approximately 7000 tonnes.

- Very good electromagnetic (EM) calorimetry for electron and photon identification and measurements, complemented by full-coverage hadronic calorimetry for accurate jet and missing transverse energy measurements, are important requirements, as these measurements form the basis of many of the studies mentioned above.

- Good muon identification and momentum resolution over a wide range of momenta and the ability to determine unambiguously the charge of high p_T muons are fundamental requirements.

- Highly efficient triggering on low transverse-momentum objects with sufficient background rejection, is a prerequisite to achieve an acceptable trigger rate for most physics processes of interest.

The overall ATLAS detector layout is shown in Fig. 2.1 and its main performance goals are listed in Table 2.1. It is important to note that, for high-p_T muons, the muon-spectrometer performance as given in Table 1 is independent of the inner-detector system.

The magnet configuration comprises a thin superconducting solenoid surrounding the inner detector cavity, and three large superconducting toroids (one barrel and two end-caps) arranged with an eight-fold azimuthal symmetry around the calorimeters. This fundamental choice drove the design of the rest of the detector. The inner detector is immersed in a 2T solenoidal field. Pattern recognition, momentum and vertex measurements,

Table 2.1: General performance goals of the ATLAS detector. Note that, for high-p_T muons, the muon spectrometer performance is independent of the inner-detector system. The units for E and p_T are in GeV.

Components	**Required resolution**	**η coverage**	
		Measurement	Trigger
Tracking	$\sigma_{p_T}/p_T = 0.05\% p_T \oplus 1\%$	$\pm$ 2.5	
EM Cal.	$\sigma_E/E = 10\%/\sqrt{E} \oplus 0.7\%$	$\pm$ 3.2	$\pm$ 2.5
Hadr. Cal. (jets)			
barrel, end-cap	$\sigma_E/E = 50\%/\sqrt{E} \oplus 3\%$	$\pm$ 3.2	$\pm$ 3.2
forward	$\sigma_E/E = 100\%/\sqrt{E} \oplus 10\%$	$3.1 < \|\eta\| < 4.9$	$3.1 < \|\eta\| < 4.9$
Muon spectrometer	$\sigma_{p_T}/p_T = 10\%$ ($p_T = 1$ TeV)	$\pm$ 2.7	$\pm$ 2.7

and electron identification are achieved with a combination of discrete, high-resolution semiconductor pixel and strip detectors in the inner part of the tracking volume, and straw-tube tracking detectors with the capability to generate and detect transition radiation in its outer part. High granularity liquid-argon (LAr) electromagnetic sampling calorimeters, with excellent performance in terms of energy and position resolution, cover the pseudo-rapidity range $|\eta| < 3.2$. The hadronic calorimetry in the range $|\eta| < 1.7$ is provided by a scintillator-tile calorimeter, which is separated into a large barrel and two smaller extended barrel cylinders, one on either side of the central barrel. In the end-caps ($|\eta| > 1.5$), LAr technology is also used for the hadronic calorimeters, matching the outer $|\eta|$ limits of end-cap electromagnetic calorimeters. The LAr forward calorimeters provide both electromagnetic and hadronic energy measurements, and extend the pseudorapidity coverage to $|\eta| = 4.9$.

The calorimeter is surrounded by the muon spectrometer. The air-core toroid system, with a long barrel and two inserted end-cap magnets, generates strong bending power in a large volume within a light and open structure. Multiple-scattering effects are thereby minimised, and excellent muon momentum resolution is achieved with three layers of high precision tracking chambers. The muon instrumentation includes, as a key component, trigger chambers with timing resolution of the order of 1.5-4 ns. The muon spectrometer defines the overall dimensions of the ATLAS detector.

The proton-proton interaction rate at the luminosity of $10^{34}\mathrm{cm}^{-2}\mathrm{s}^{-1}$ is approximately 1 GHz, while the event data recording, based on technology and resource limitations, is limited to about 200 Hz. This requires an overall rejection factor of $5 \cdot 10^6$ against minimum-bias processes while maintaining maximum efficiency for the new physics. The Level-1 (L1) trigger system uses a subset of the total detector information to make a decision on whether

or not to continue processing an event, reducing the data rate to approximately 75 kHz (limited by the bandwidth of the readout system, which is upgradeable to 100 kHz). The subsequent two levels, collectively known as the high-level trigger, are the Level-2 (L2) trigger and the event filter. They provide the reduction to a final data-taking rate of approximately 200 Hz. The initial input capacity will be limited to a L1 trigger rate of about 40 kHz. This capacity will be increased as needed to deal with the LHC luminosity profile during the first years. The ultimate goal is to be able to handle 100 kHz if needed. Some parts of the muon spectrometer are staged, most noticeably part of the precision chambers in the transition region between the barrel and the end-caps. In addition, some of the forward shielding elements will be completed later, as the LHC approaches design luminosity.

2.4 Tracking

Approximately 1000 particles will emerge from the collision point every 25 ns within $|\eta| < 2.5$, creating a very large track density in the detector. To achieve the momentum and vertex resolution requirements imposed by the benchmark physics processes, high-precision measurements must be made with fine detector granularity. Pixel and silicon microstrip (SCT) trackers, used in conjunction with the straw tubes of the Transition Radiation Tracker (TRT), offer these features. The layout of the Inner Detector (ID) is illustrated in Fig. 2.2. The ID is immersed in a 2 T magnetic field generated by the central solenoid, which extends over a length of 5.3 m with a diameter of 2.5 m. The precision tracking detectors (pixels and SCT) cover the region $|\eta| < 2.5$. In the barrel region, they are arranged on concentric cylinders around the beam axis while in the end-cap regions they are located on disks perpendicular to the beam axis. The highest granularity is achieved around the vertex region using silicon pixel detectors. All pixel sensors are identical and have a minimum pixel size of $50 \times 400\mu$m. The pixel layers are segmented in R-ϕ and z with typically three pixel layers crossed by each track. The intrinsic accuracies in the barrel are 10 μm (R-ϕ) and 115 μm (z) and in the disks are 10 μm (R-ϕ) and 115 μm (z).The pixel detector has approximately 80.4 million readout channels. For the SCT, eight strip layers (four space points) are crossed by each track. In the barrel region, this detector uses small-angle (40 mrad) stereo strips to measure both coordinates, with one set of strips in each layer parallel to the beam direction, measuring R-ϕ. They consist of two 6.4 cm long daisy-chained sensors with a strip pitch of 80 μm. In the end-cap region, the detectors have a set of strips running radially and a set of stereo strips at an angle of 40 mrad. The mean pitch of the strips is also approximately 80 μm. The intrinsic accuracies per module

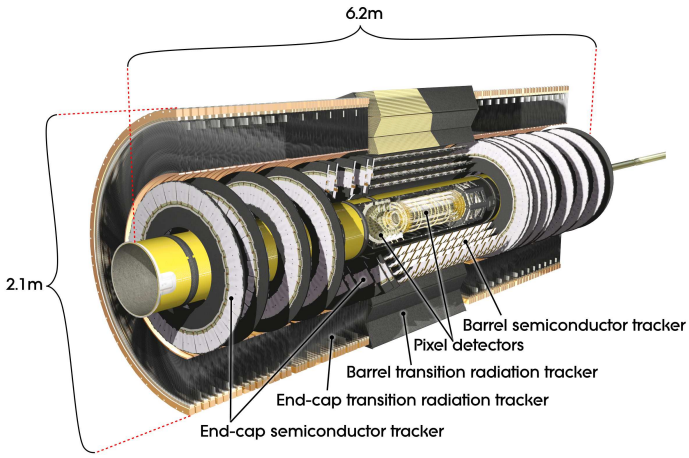

Figure 2.2: Cut-away view of the ATLAS inner detector.

in the barrel are 17 μm (R-ϕ) and 580 μm (z) and in the disks are 17 μm (R-ϕ) and 580 μm (R). The total number of readout channels in the SCT is approximately 6.3 million.

A large number of hits (typically 36 per track) is provided by the 4 mm diameter straw tubes of the TRT, which enables track-following up to $|\eta| < 2.5$. The TRT only provides Rϕ information, for which it has an intrinsic accuracy of 130 μm per straw. In the barrel region, the straws are parallel to the beam axis and are 144 cm long, with their wires divided into two halves, approximately at $|\eta| = 0$. In the end-cap region, the 37 cm long straws are arranged radially in wheels. The total number of TRT readout channels is approximately 351000. The combination of precision trackers at small radii with the TRT at a larger radius gives very robust pattern recognition and high precision in both R-ϕ and z coordinates. The straw hits at the outer radius contribute significantly to the momentum measurement, since the lower precision per point compared to the silicon is compensated by the large number of measurements and longer measured track length. The inner detector system provides tracking measurements in a range matched by the precision measurements of the electromagnetic calorimeter. The electron identification capabilities are enhanced by the detection of transition-radiation photons in the xenon-based gas mixture of the straw tubes. The semiconductor trackers also allow impact parameter measurements and vertexing for heavy-flavour and τ-lepton tagging. The secondary vertex measurement performance is enhanced by the innermost layer of pixels, at a radius of about 5 cm.

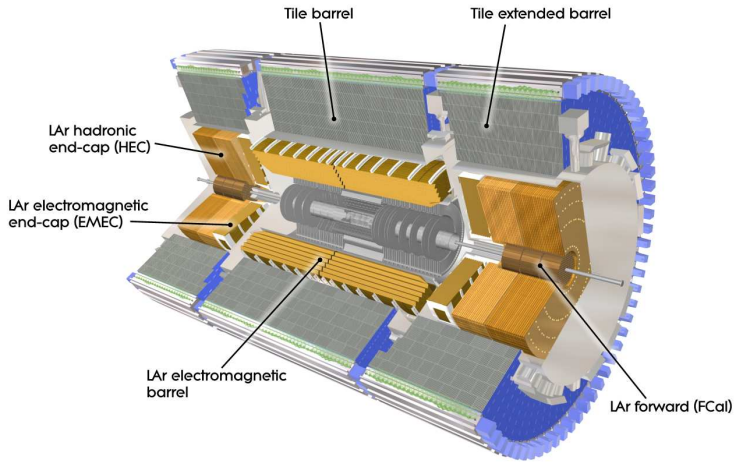

Figure 2.3: Cut-away view of the ATLAS calorimeter system.

2.5 Calorimetry

A view of the sampling calorimeters is presented in Fig. 2.3. These calorimeters cover the range $|\eta| < 4.9$, using different techniques suited to the widely varying requirements of the physics processes of interest and of the radiation environment over this large η-range. Over the η region matched to the inner detector, the fine granularity of the EM calorimeter is ideally suited for precision measurements of electrons and photons. The coarser granularity of the rest of the calorimeter is sufficient to satisfy the physics requirements for jet reconstruction and E_T^{MISS} measurements. Calorimeters must provide good containment for electromagnetic and hadronic showers, as well as limit punch-through into the muon system. Hence, calorimeter depth is an important consideration. The total thickness of the EM calorimeter is more than 22 radiation lengths (X0) in the barrel and more than 24 X0 in the end-caps. The approximate 9.7 interaction lengths (λ) of active calorimeter in the barrel (10 λ in the end-caps) are adequate to provide good resolution for high-energy jets (see Table 2.1). The total thickness, including 1.3 λ from the outer support, is 11 λ at $\eta = 0$ and has been shown both by measurements and simulations to be sufficient to reduce punch-through well below the irreducible level of prompt or decay muons. Together with the large η coverage, this thickness will also ensure a good E_T^{MISS} measurement, which is crucial for many physics signatures and in particular for SUSY particle searches.

2.5.1 LAr electromagnetic calorimeter

The EM calorimeter is divided into a barrel part ($|\eta| < 1.475$) and two end-cap components ($1.375 < |\eta| < 3.2$), each housed in their own cryostat. The position of the central solenoid in front of the EM calorimeter demands optimisation of the material in order to achieve the desired calorimeter performance. As a consequence, the central solenoid and the LAr calorimeter share a common vacuum vessel, thereby eliminating two vacuum walls. The barrel calorimeter consists of two identical half-barrels, separated by a small gap (4 mm) at z = 0. Each end-cap calorimeter is mechanically divided into two coaxial wheels: an outer wheel covering the region $1.375 < |\eta| < 2.5$, and an inner wheel covering the region $2.5 < |\eta| < 3.2$. The EM calorimeter is a lead-LAr detector with accordion-shaped kapton electrodes and lead absorber plates over its full coverage. The accordion geometry provides complete ϕ symmetry without azimuthal cracks. The lead thickness in the absorber plates has been optimised, as a function of η, in terms of EM calorimeter performance in energy resolution. Over the region devoted to precision physics ($|\eta| < 2.5$), the EM calorimeter is segmented into three longitudinal sections. For the end-cap inner wheel, the calorimeter is segmented in two longitudinal sections and has a coarser lateral granularity than for the rest of the acceptance. In the region of $|\eta| < 1.8$, a presampler detector is used to correct for the energy lost by electrons and photons upstream of the calorimeter. The presampler consists of an active LAr layer of thickness 1.1 cm (0.5 cm) in the barrel (end-cap) region.

2.5.2 Hadronic calorimeters

Tile calorimeter The tile calorimeter is placed directly outside the EM calorimeter envelope. Its barrel covers the region $|\eta| < 1.0$, and its two extended barrels the range $0.8 < |\eta| < 1.7$. It is a sampling calorimeter using steel as the absorber and scintillating tiles as the active material. The barrel and extended barrels are divided azimuthally into 64 modules. Radially, the tile calorimeter extends from an inner radius of 2.28 m to an outer radius of 4.25 m. It is longitudinally segmented in three layers approximately 1.5, 4.1 and 1.8 interaction lengths thick for the barrel and 1.5, 2.6, and 3.3 interaction length for the extended barrel. The total detector thickness at the outer edge of the tile-instrumented region is 9.7 λ at $\eta = 0$. The tiles are 3 mm thick and the total thickness of the steel plates in one period is 14 mm. Two sides of the scintillating tiles are read out by wavelength shifting fibres into two separate photomultiplier tubes. In η , the readout cells built by grouping fibres into the photomultipliers are pseudo-projective towards the interaction region.

LAr hadronic end-cap calorimeter The Hadronic End-cap Calorimeter (HEC) consists of two independent wheels per end-cap, located directly behind the end-cap electromagnetic calorimeter and sharing the same LAr cryostats. To reduce the drop in material density at the transition between the end-cap and the forward calorimeter (around $|\eta| = 3.1$), the HEC extends out to $|\eta| = 3.2$, thereby overlapping with the forward calorimeter. Similarly, the HEC η range also slightly overlaps that of the tile calorimeter ($|\eta| < 1.7$) by extending to $|\eta| = 1.5$. Each wheel is built from 32 identical wedge-shaped modules, assembled with fixtures at the periphery and at the central bore. Each wheel is divided into two longitudinal segments, for a total of four layers per end-cap. The wheels closest to the interaction point are built from 25 mm parallel copper plates, while those further away use 50 mm copper plates (for all wheels the first plate is half-thickness). The outer radius of the copper plates is 2.03 m, while the inner radius is 0.475 m (except in the overlap region with the forward calorimeter where this radius becomes 0.372 m). The copper plates are interleaved with 8.5 mm LAr gaps, providing the active medium for this sampling calorimeter.

LAr forward calorimeter The Forward Calorimeter (FCal) is integrated into the end-cap cryostats, as this provides clear benefits in terms of uniformity of the calorimetric coverage as well as reduced radiation background levels in the muon spectrometer. In order to reduce the amount of neutron albedo in the inner detector cavity, the front face of the FCal is recessed by about 1.2 m with respect to the EM calorimeter front face. This severely limits longitudinal space and therefore calls for a high-density design. The FCal is approximately 10 interaction lengths deep, and consists of three modules in each end-cap: the first, made of copper, is optimised for electromagnetic measurements, while the other two, made of tungsten, measure predominantly the energy of hadronic interactions. Each module consists of a metal matrix, with regularly spaced longitudinal channels filled with the electrode structure consisting of concentric rods and tubes parallel to the beam axis. The LAr in the gap between the rod and the tube is the sensitive medium. This geometry allows for excellent control of the gaps, which are as small as 0.25 mm in the first section, in order to avoid problems due to ion buildup.

2.6 Muon system

The conceptual layout of the muon spectrometer is shown in Fig. 2.4. It is based on the magnetic deflection of muon tracks in the large superconducting air-core toroid magnets, instrumented with separate trigger and high-precision tracking chambers. Over the range $|\eta| < 1.4$, magnetic bend-

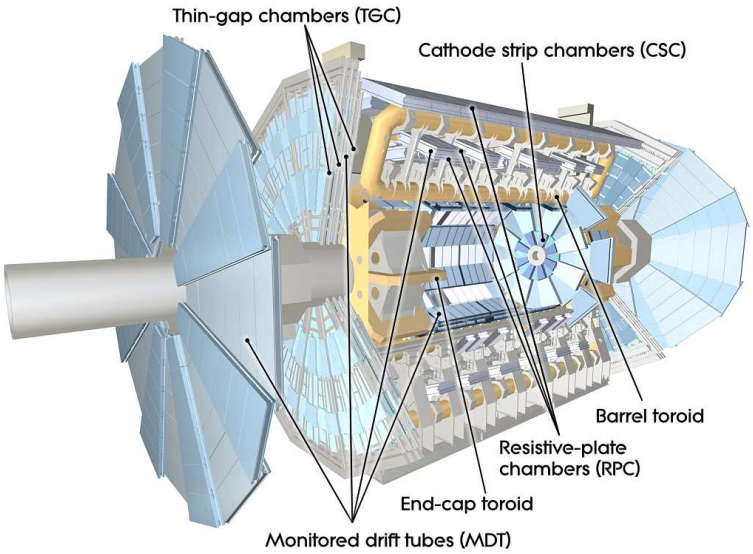

Figure 2.4: Cut-away view of the ATLAS muon system.

ing is provided by the large barrel toroid. For $1.6 < |\eta| < 2.7$, muon tracks are bent by two smaller end-cap magnets inserted into both ends of the barrel toroid. Over $1.4 < |\eta| < 1.6$, usually referred to as the transition region, magnetic deflection is provided by a combination of barrel and end-cap fields. This magnet configuration provides a field which is mostly orthogonal to the muon trajectories, while minimising the degradation of resolution due to multiple scattering. The anticipated high level of particle flux has had a major impact on the choice and design of the spectrometer instrumentation, affecting performance parameters such as rate capability, granularity, ageing properties, and radiation hardness. In the barrel region, tracks are measured in chambers arranged in three cylindrical layers around the beam axis; in the transition and end-cap regions, the chambers are installed in planes perpendicular to the beam, also in three layers.

2.6.1 The toroid magnets

A system of three large air-core toroids generates the magnetic field for the muon spectrometer. The two end-cap toroids are inserted in the barrel toroid at each end and line up with the central solenoid. Each of the three toroids consists of eight coils assembled radially and symmetrically around the beam axis. The end-cap toroid coil system is rotated by 22.5° with respect to the barrel toroid coil system in order to provide radial overlap

and to optimise the bending power at the interface between the two coil systems. The barrel toroid coils are housed in eight individual cryostats, with the linking elements between them providing the overall mechanical stability. Each end-cap toroid consists of eight racetrack-like coils in an aluminium alloy housing. Each coil has two double-pancake type windings. They are cold-linked and assembled as a single cold mass, housed in one large cryostat. Therefore the internal forces in the end-cap toroids are taken by the cold supporting structure between the coils, a different design solution than in the barrel toroid. The performance in terms of bending power is characterised by the field integral $\int Bdl$, where B is the field component normal to the muon direction and the integral is computed along an infinite momentum muon trajectory, between the innermost and outermost muon-chamber planes. The barrel toroid provides 1.5 to 5.5 $T \cdot m$ of bending power in the pseudorapidity range $0 < |\eta| < 1.4$, and the end-cap toroids approximately 1 to 7.5 Tm in the region $1.6 < |\eta| < 2.7$. The bending power is lower in the transition regions where the two magnets overlap ($1.4 < |\eta| < 1.6$).

2.6.2 Muon chamber types

Over most of the η-range, a precision measurement of the track coordinates in the principal bending direction of the magnetic field is provided by Monitored Drift Tubes (MDT's). The mechanical isolation in the drift tubes of each sense wire from its neighbours guarantees a robust and reliable operation. At large pseudorapidities, Cathode Strip Chambers (CSC's, which are multiwire proportional chambers with cathodes segmented into strips) with higher granularity are used in the innermost plane over $2 < |\eta| < 2.7$, to withstand the demanding rate and background conditions. The stringent requirements on the relative alignment of the muon chamber layers are met by the combination of precision mechanical-assembly techniques and optical alignment systems both within and between muon chambers. The trigger system covers the pseudorapidity range $|\eta| < 2.4$. Resistive Plate Chambers (RPC's) are used in the barrel and Thin Gap Chambers (TGC's) in the end-cap regions. The trigger chambers for the muon spectrometer serve a three-fold purpose: provide bunch-crossing identification, provide well-defined p_T thresholds, and measure the muon coordinate in the direction orthogonal to that determined by the precision-tracking chambers.

2.6.3 Muon chamber alignment and B-field reconstruction

The overall performance over the large areas involved, particularly at the highest momenta, depends on the alignment of the muon chambers with

respect to each other and with respect to the overall detector. The accuracy of the stand-alone muon momentum measurement necessitates a precision of $30\mu m$ on the relative alignment of chambers both within each projective tower and between consecutive layers in immediately adjacent towers. The internal deformations and relative positions of the MDT chambers are monitored by approximately 12000 precision-mounted alignment sensors, all based on the optical monitoring of deviations from straight lines. Because of geometrical constraints, the reconstruction and/or monitoring of the chamber positions rely on somewhat different strategies and sensor types in the end-cap and barrel regions, respectively. The accuracy required for the relative positioning of non-adjacent towers to obtain adequate mass resolution for multi-muon final states, lies in the few millimetre range. This initial positioning accuracy is approximately established during the installation of the chambers. Ultimately, the relative alignment of the barrel and forward regions of the muon spectrometer, of the calorimeters and of the inner detector will rely on high-momentum muon trajectories. For magnetic field reconstruction, the goal is to determine the bending power along the muon trajectory to a few parts in a thousand. The field is continuously monitored by a total of approximately 1800 Hall sensors distributed throughout the spectrometer volume. Their readings are compared with magnetic-field simulations and used for reconstructing the position of the toroid coils in space, as well as to account for magnetic perturbations induced by the tile calorimeter and other nearby metallic structures.

2.7 Forward detectors

Three smaller detector systems cover the ATLAS forward region . The main function of the first two systems is to determine the luminosity delivered to ATLAS. At ± 17 m from the interaction point lies LUCID (LUminosity measurement using Cerenkov Integrating Detector). It detects inelastic $p-p$ scattering in the forward direction, and is the main online relative-luminosity monitor for ATLAS. The second detector is ALFA (Absolute Luminosity For ATLAS). Located at ± 240 m, it consists of scintillating fibre trackers located inside Roman pots which are designed to approach as close as 1 mm to the beam. The third system is the Zero-Degree Calorimeter (ZDC), which plays a key role in determining the centrality of heavy-ion collisions. It is located at ± 140 m from the interaction point, just beyond the point where the common straight-section vacuum-pipe divides back into two independent beam-pipes. The ZDC modules consist of layers of alternating quartz rods and tungsten plates which will measure neutral particles at pseudorapidities $|\eta| \geq 8.2$.

2.8 Trigger, readout, data acquisition, and control systems

The Trigger and Data Acquisition (collectively TDAQ) systems, the timing- and trigger-control logic, and the Detector Control System (DCS) are partitioned into sub-systems, typically associated with sub-detectors, which have the same logical components and building blocks. The trigger system has three distinct levels: L1, L2, and the event filter. Each trigger level refines the decisions made at the previous level and, where necessary, applies additional selection criteria. The data acquisition system receives and buffers the event data from the detector-specific readout electronics, at the L1 trigger accept rate, over 1600 point-to-point readout links. The first level uses a limited amount of the total detector information to make a decision in less than 2.5 μs, reducing the rate to about 75 kHz. The two higher levels access more detector information for a final rate of up to 200 Hz with an event size of approximately 1.3 Mbyte.

2.8.1 Trigger system

The L1 trigger searches for high transverse-momentum muons, electrons, photons, jets, and τ-leptons decaying into hadrons, as well as large missing and total transverse energy. Its selection is based on information from a subset of detectors. High transverse-momentum muons are identified using trigger chambers in the barrel and end-cap regions of the spectrometer. Calorimeter selections are based on reduced-granularity information from all the calorimeters. Results from the L1 muon and calorimeter triggers are processed by the central trigger processor, which implements a trigger menu made up of combinations of trigger selections. Pre-scaling of trigger menu items is also available, allowing optimal use of the bandwidth as luminosity and background conditions change. Events passing the L1 trigger selection are transferred to the next stages of the detector-specific electronics and subsequently to the data acquisition via point-to-point links. In each event, the L1 trigger also defines one or more Regions-of-Interest (RoI's), i.e. the geographical coordinates in η and ϕ, of those regions within the detector where its selection process has identified interesting features. The RoI data include information on the type of feature identified and the criteria passed, e.g. a threshold. This information is subsequently used by the high-level trigger. The L2 selection is seeded by the RoI information provided by the L1 trigger over a dedicated data path. L2 selections use, at full granularity and precision, all the available detector data within the RoI's (approximately 2% of the total event data). The L2 menus are designed to reduce the trigger rate to approximately 3.5 kHz, with an event processing time of about 40

ms, averaged over all events. The final stage of the event selection is carried out by the event filter, which reduces the event rate to roughly 200 Hz. Its selections are implemented using offline analysis procedures within an average event processing time of the order of four seconds.

2.8.2 Readout architecture and data acquisition

The Readout Drivers (ROD's) are detector-specific functional elements of the front-end systems, which achieve a higher level of data concentration and multiplexing by gathering information from several front-end data streams. Although each sub-detector uses specific front-end electronics and ROD's, these components are built from standardised blocks and are subject to common requirements. The front-end electronics sub-system includes different functional components:

- the front-end analogue or analogue-to-digital processing;
- the L1 buffer in which the (analogue or digital) information is retained for a time long enough to accommodate the L1 trigger latency;
- the derandomising buffer in which the data corresponding to a L1 trigger accept are stored before being sent to the following level. This element is necessary to accommodate the maximum instantaneous L1 rate without introducing significant deadtime (maximum 1%);
- the dedicated links or buses which are used to transmit the front-end data stream to the next stage.

After an event is accepted by the L1 trigger, the data from the pipe-lines are transferred off the detector to the RODs. Digitised signals are formatted as raw data prior to being transferred to the DAQ system. The RODs follow some general ATLAS rules, including the definition of the data format of the event, the error detection/recovery mechanisms to be implemented, and the physical interface for the data transmission to the DAQ system. The first stage of the DAQ, the readout system, receives and temporarily stores the data in local buffers. It is subsequently solicited by the L2 trigger for the event data associated to RoIs. Those events selected by the L2 trigger are then transferred to the event-building system and subsequently to the event filter for final selection. Events selected by the event filter are moved to permanent storage at the CERN computer centre. In addition to the movement of data, the data acquisition also provides for the configuration, control and monitoring of the hardware and software components which together provide the data-taking functionality.
The DCS permits the coherent and safe operation of the ATLAS detector

hardware, and serves as a homogeneous interface to all sub-detectors and to the technical infrastructure of the experiment. It controls, continuously monitors and archives the operational parameters, signals any abnormal behaviour to the operator, and allows automatic or manual corrective actions to be taken. Typical examples are high-and low-voltage systems for detector and electronics, gas and cooling systems, magnetic field, temperatures, and humidity. The DCS also enables bi-directional communication with the data acquisition system in order to synchronise the state of the detector with data-taking. It also handles the communication between the sub-detectors and other systems which are controlled independently, such as the LHC accelerator, the CERN technical services, the ATLAS magnets, and the detector safety system.

Bibliography

[1] ATLAS Collaboration, G. Aad et al., The ATLAS experiment at the CERN Large Hadron Collider, JINST (2008) S08003;

[2] ATLAS Collaboration, Detector and Physics Performance Technical Design Report CERN/LHCC/99-14/15 (1999);

Chapter 3

Analysis tools

3.1 Introduction

In this chapter I will briefly show the techniques to generate and analyze the events used in my thesis. These techniques are essentially divided into three categories:

- **The event generation.** In order to evaluate the potential of the ATLAS detector, Monte Carlo generators are used to simulate physical processes producing all the particles present in the final state, starting from the primary p-p collisions. Usually the generators produce partons in the final state so, the hadronization process starting from quarks and gluons is also simulated.

- **The simulation of detector response.** The passage through the detector of all the physical particles produced in the collisions is simulated, reproducing their interaction with the material of the detector.

- **The event reconstruction.** Starting from the raw energy released by the particles in the detector, many different algorithms reconstruct the energy and the position of the particles.

The last two steps can be simulated either in a complete and detailed way (called "full simulation") or in a less detailed but faster way (called "fast simulation"), where the effect of the passage of the particles through the matter and the event reconstruction are parametrized using probability distribution functions of the relevant physical quantities determined by the full simulation data. All the samples used in this thesis have been simulated using the full simulation procedure.
In the next sections I will first describe the three steps mentioned above; I will then introduce the samples used in this work, discussing in particular

the specific physical characteristic of each data sample; finally I will discuss the performance of the detector in. reconstructing the physical objects used in the analysis. A list of the useful kinematical variables strongly used in this study is also presented.

3.2 The event generation

The event generation procedure usually is independent from the other two steps of the simulation, to allow to independently modify, if needed, either the detector description or the digitization algorithms without requiring to generate again the physical processes. The simulation of the p-p collisions and of the subsequent decay chains and branching ratios (BRs) is very complicated because, for each simulated physical process (e.g. pp$\rightarrow$ SUSY or pp$\rightarrow t\bar{t}$), all the Feynman diagrams have to be taken into account to compute the total amplitude.
The generator starts from the elementary interactions between quarks and gluons belonging to the two protons, computes the amplitude to a given order evaluating all the Feynman diagrams contributing to the process in hand and then makes the convolution of the evaluated cross sections with parton distribution functions (pdf's) of the quarks and the gluons inside the protons. These pdf's are determined analyzing the data collected in previous experiments and extrapolating them up to the LHC energy. Obviously this extrapolation procedure introduces a source of uncertainty, in addition to the experimental uncertainty on the pdf's itself, that contributes to the total uncertainty on the computed cross section of QCD events. Once the cross sections and the momentum distributions have been computed, the generator simulates the radiative processes involving the final states. Special care is used in the simulation of the QCD processes where the collinear and infrared divergences play an important role. Finally the generator simulates the production of the hadronic jets by quarks and gluons, starting once again from models gathered from the experimental data.
Many other features have to be taken into account in the computation process (e.g. the top quarks that does not hadronize, the hadronic decay chains with respective branching ratios, the SUSY particles production, etc.); for each of them the whole procedure described above has to be repeated.
The generators used in my work are:

- **MC@NLO.**[1] Generator used, in this work, to simulate the $t\bar{t}$ processes. It includes full calculation of the production and decay processes at NLO.

- **HERWIG.**[2] Generator used here to simulate SUSY events and dibosons samples events(e.g. WW, WZ and ZZ). This generator also pro-

vides the simulation of the hadronization and the QCD radiation processes. Even if the calculation is performed only at LO, the final cross sections of SUSY processes are rescaled by a constant factor (called k-factor) to the total NLO cross-section computed by Prospino[3].

- **ALPGEN.**[4] Generator used to simulate W+jets, Z+jets, $b\bar{b}$+jets events. It is a specific generator built to simulate processes with final states characterised by high-multiplicity of jets (e.g. Wqqqq). Because it computes only the matrix element amplitudes at LO, one has to interface it with HERWIG to simulate the hadronization and the QCD radiation processes.

- **PYTHIA.**[5] Generator used to simulate QCD processes. It computes the evolution from QCD hard processes to the hadronic final state characterized by a large number of jets. The calculation of the fundamental QCD hard processes involving gluons and quarks is performed at LO.

- **AcerMC**[6] Generator used to simulate the $t\bar{t}$ and the $Z \rightarrow b\bar{b}$ processes. It includes full calculation at LO of the processes characterised by the presence of the heavy flavour jets and multiple isolated leptons in the final state.

3.3 The detector simulation

3.3.1 GEANT4

The second step after the Monte Carlo events generation is the simulation of the interaction of the particles produced in the event with the detector. In the "full simulation", this is done using GEANT4 [7].
Starting from the information about the ATLAS geometry, the materials description and the map of the magnetic field, the software tracks all the particles in the detector and then simulates and records the energy released in their passage through the detector materials. In particular:

1. The tracking procedure has been implemented using tags of the detector geometry that are also available at the reconstruction level, ensuring a complete agreement between the simulation phase and the reconstruction phase. However, in the simulation of the samples used in this work, some difference between simulation and reconstruction have been introduced by hand in order to describe an imperfect knowledge of the real detector geometry, as will be at the LHC start-up.

2. The simulation of the electromagnetic and hadronic showers is performed using a very low threshold (10 KeV) on the elementary interaction processes with respect to the shower energy that is usually in the TeV range. The comparison with test-beam data has been used as a fundamental cross-check to evaluate the goodness of the simulation itself.

3. An accurate description of the dead materials (e.g. support structures and not instrumented regions) is available. It plays a fundamental role in the physical performances of the apparatus because it affects some important parameters like the energy resolution, the linearity of the calorimeters response and the reconstruction of the missing energy of the event.

During all these phases, the 4-vectors of all the particles are available, enabling the software to compute the energy flow of the particles during their passage through the detector, that is a fundamental quantity for example to compute the real missing energy coming from the undetected particles and the energy lost in dead materials.

3.3.2 The digitization process

The digitization process is the second level of the detector simulation. At this step, all the information collected in the previous level are recorded, reprocessed in order to simulate the real electronic output of the detector and then formatted as real data and in this form written on magnetic media for further analysis. It is worth to mention that also partial results of this step (and of the previous step) can also be written on disk to allow the reconstruction of "true" quantities (the so called "Monte Carlo truth") that is very useful to understand features of the detector that could be hidden by the digitization phase and/or by the reconstruction phase described in the next section.

3.3.3 The reconstruction process

This is the final step in the production of simulated data samples; the information collected in the previous steps are transformed in the physical objects (electrons, muons, jets...) that can be used during the analysis using the same reconstruction programs that will be used to process real data. Starting from the signals in the detector, the ATLAS software called Athena loads the geometry of the detector, the magnetic field map and the results of the digitization process and then starts the reconstruction phase separately for each sub-detector.

In the **Pixel** and **SCT** detectors, the hits in the silicon are clustered in order to give the coordinates of the space points associated to the passage of the particles (clustering procedure). In the **TRT** detector, the calibrations R-t (position-drift time) are used to reconstruct the spatial coordinates of the points associated with the passage of the particles in the tubes. The reconstruction software keeps all these information and tries to identify the tracks (e.g. helicoidal trajectories in the electric and magnetic field) and their fundamental parameters combining the measured points in the single detectors planes.
In the **calorimetric system**, the cells where the amplitude of the electronic signal is larger than a certain threshold value, become the seeds around which the software groups the adjacent cells in clusters that are the basis to built the physical objects. There are several different clustering algorithms, but in this work I have used the clustering algorithm based on the fixed window $\Delta\Phi X\Delta\eta = 3X7$ cells to reconstruct the electrons in the electromagnetic calorimeter.
For the hadronic jets, an algorithm that uses at the same time cells from both calorimeters in a 0.4 amplitude cone in the (η, ϕ) plane has been used. All the clusters are then calibrated in order to give the best estimation of their energy.
In the **muon spectrometer**, starting from the coordinates of the points in the various planes of the system, the software combines them reconstructing the tracks with a procedure similar to the Inner Detector one.
The various information from the different sub-detectors are then combined to build more sophisticated objects. The electromagnetic clusters are combined with the tracks in the ID to find the electrons candidates and distinguish them from the jets (see later in this chapter) and to reconstruct the conversions of the photons. The electromagnetic clusters without any associated track are instead identified as unconverted photons. The characteristics of the hadronic jets and their associated tracks are used to distinguish the τ-jets from those generated by the quarks or the gluons. The ID and the muon spectrometer information are combined to give the best precision in the muon reconstruction.

3.4 Samples overview

The Computing System Challenge (CSC) effort has been organized by the ATLAS Collaboration with the goal to summarize all the activities done (both analysis and detector performances) within the experiment, and to prepare the strategies for the first collisions. In order to perform this effort,

Table 3.1: SUSY sample CSC ID, production cross section and the available number of events in the sample.

Signal	CSC ID	σLO (pb)	σNLO (pb)	N
SU1	005401	7.43	10.86	200 K
SU2	005402	4.86	7.18	50 K
SU3	005403	18.59	27.68	500 K
SU4	006400	262	402.19	200 K

a large and exhaustive Monte Carlo production has been realized. For the present study, I have used only the simulated data produced for this CSC activity.
The SUSY signal samples listed in Table 3.1 correspond to the following mSUGRA points, which were chosen to be roughly consistent with the observed cold dark matter density:

- SU1 $m_0 = 70$GeV, $m_{1/2} = 350$GeV, $A_0 = 0$, $\tan\beta = 10$, $\mu > 0$. Coannihilation region with nearly degenerate masses of $\tilde{\chi}_1^0$ and $\tilde{\ell}$.
- SU2 $m_0 = 3550$GeV, $m_{1/2} = 300$GeV, $A_0 = 0$, $\tan\beta = 10$, $\mu > 0$. Focus point region near boundary where $\mu^2 < 0$. This region of the parameter space is characterised by light Higgsinos which annihilate efficiently making the relic density of neutralinos compatible with cosmological data.
- SU3 $m_0 = 100$GeV, $m_{1/2} = 300$GeV, $A_0 = -300$GeV, $\tan\beta = 6$, $\mu > 0$. Bulk region: relatively light sleptons enhance LSP annihilation.
- SU4 $m_0 = 200$GeV, $m_{1/2} = 160$GeV, $A_0 = -400$GeV, $\tan\beta = 10$, $\mu > 0$. Low mass point close to Tevatron bound.

Masses of supersymmetric particles corresponding to each of these points are listed in Table 3.2.

Even though the SUSY samples are all generated with mSUGRA, they provide a rather wide range of possible decay topologies. For all these points, the gluino mass is less than 1TeV, and the ratio $M(\tilde{g})/M(\tilde{\chi}_1^0) = 6$–$8$. For all points except SU2, the squark and gluino masses are comparable. Hence gluinos and squarks are copiously produced through strong interaction and decay giving relatively hard jets, possible leptons, and E_T^{MISS}. These features are common to a large class of supersymmetric models - although in some models not all features could be present at the same time-. However the capability to reproduce cold dark Matter results are very specific to

Table 3.2: Masses in GeV for the fully simulated SUSY samples.

Particle	SU1	SU2	SU3	SU4
$\tilde{d}_L$	764.90	3564.13	636.27	419.84
$\tilde{u}_L$	760.42	3563.24	631.51	412.25
$\tilde{b}_1$	697.90	2924.80	575.23	358.49
$\tilde{t}_1$	572.96	2131.11	424.12	206.04
$\tilde{d}_R$	733.53	3576.13	610.69	406.22
$\tilde{u}_R$	735.41	3574.18	611.81	404.92
$\tilde{b}_2$	722.87	3500.55	610.73	399.18
$\tilde{t}_2$	749.46	2935.36	650.50	445.00
$\tilde{e}_L$	255.13	3547.50	230.45	231.94
$\tilde{\nu}_e$	238.31	3546.32	216.96	217.92
$\tilde{\tau}_1$	146.50	3519.62	149.99	200.50
$\tilde{\nu}_\tau$	237.56	3532.27	216.29	215.53
$\tilde{e}_R$	154.06	3547.46	155.45	212.88
$\tilde{\tau}_2$	256.98	3533.69	232.17	236.04
$\tilde{g}$	832.33	856.59	717.46	413.37
$\tilde{\chi}_1^0$	136.98	103.35	117.91	59.84
$\tilde{\chi}_2^0$	263.64	160.37	218.60	113.48
$\tilde{\chi}_3^0$	466.44	179.76	463.99	308.94
$\tilde{\chi}_4^0$	483.30	294.90	480.59	327.76
$\tilde{\chi}_1^+$	262.06	149.42	218.33	113.22
$\tilde{\chi}_2^+$	483.62	286.81	480.16	326.59
h^0	115.81	119.01	114.83	113.98
H^0	515.99	3529.74	512.86	370.47
A^0	512.39	3506.62	511.53	368.18
H^+	521.90	3530.61	518.15	378.90
t	175.00	175.00	175.00	175.00

mSUGRA.

The SM background processes relevant for SUSY studies include $t\bar{t}$, $W+jets$, $Z+jets$, QCD jets, and diboson processes. Due to the presence of hard cuts in jets and E_T^{MISS} in almost all the SUSY analysis, specifically modified generators are used to simulate efficiently these backgrounds. In what follows, the modification to the generators are referred as *generation filters*. In the case of $t\bar{t}$ process, the MC@NLO generator was used. It includes full next to leading order QCD corrections and computes partonic hard subprocesses, which have non trivial implications on the dynamics of $t\bar{t}$ production

process at LHC energies.
In the case of $Z \rightarrow b\bar{b}$ process, the AcerMC generator was used. It provides the calculation of the matrix elements and phase space modules for the generation of the implemented processes. The hard process event, generated with these modules, can be completed by the initial and final state radiation, hadronisation and decays, simulated with PYTHIA.
The AcerMC generator was used also to simulate the $t\bar{t}$ process to perform a comparison between this generator and the MC@NLO generator allowing to evaluate the systematics related to the generator parameters. In particular, referring to the Table 3.3, the dataset identified by the ID 005205 simulates the process where at least one top quark decays leptonically (as in the MC@NLO case), while the datasets identified by the ID 006250 and 006251 simulate the $t\bar{t}$ process when the mass of the top quark is respectively lower or higher than the nominal value of 175 GeV.
The systematic uncertainties due to these effects will be analyzed in Chapter 4.
In the case of vector boson samples $W + jets$ and $Z + jets$ the ALPGEN generator was used.
At leading order in QCD and electroweak interactions, it calculates the exact matrix elements of multiparton hard processes in hadronic collisions [4]. Separated samples are generated exclusively for a fixed number of jets, by applying the MLM parton-jet matching procedure [1] [8] and later added together into one unique inclusive sample. In all samples, the generation filters reflect the minimum requests for the standard ATLAS SUSY search: the hardest jet transverse momentum above 80 GeV, the fourth jet transverse momentum above 40 GeV and missing transverse energy above 80 GeV.

Although ALPGEN samples are generally regarded to be the most appropriate for the background prediction in SUSY studies, PYTHIA samples, with higher statistics, were also used for $QCDjets$ backgrounds. Events with at least two high p_T jets are generated with filters: the hardest jet transverse momentum above 80 GeV, the second jet transverse momentum above 40 GeV and missing transverse energy above 100 GeV.
The contribution of the diboson processes WW, ZZ and WZ is almost negligible as they are strongly suppressed by the typical SUSY requests on the number of jets with high transverse momenta and on the missing transverse energy. HERWIG samples were used for the analysis of the diboson contri-

[1] This procedure consists of an angular association between the original parton and the jet that it produces. For multijets/multipartons events this procedure prevents that the events characterised by *n* partons and *n+1* jets are counted also in the sample with *n+1* partons and *n+1* jets.

Table 3.3: Background sample CSC ID, production cross-section, event filter efficiency, the effective cross-section and the available number of $t\bar{t}$ and QCD background events.

Background	CSC ID	σ (pb)	EF_{eff} (%)	σ_{eff} (pb)	N
$t\bar{t}$ MC@NLO	005200	833	54	450	600 K
$t\bar{t}$ AcerMC	005205	833	54	450	500 K
$t\bar{t}$ AcerMC	006250	833	54	450	500 K
$t\bar{t}$ AcerMC	006251	833	54	450	500 K
$Z \to b\bar{b}$	005178	205	49	102	125 K
J4	008090	3.16×10^{5}	0.29	916.40	70 K
J5	008091	1.25×10^{4}	5.24	655.	85 K
J6	008092	344	19.6	67.42	35 K
J7	008093	5.3	100	5.3	4 K
J8	008094	2.21×10^{-2}	100	2.21×10^{-2}	4 K

Table 3.4: Diboson sample CSC ID, production cross-section, event filter efficiency, K factor for recalculation the cross-section from leading-order to next-to-leading-order value, recalculated cross-section σ_{eff}^{NLO} and the available number of events in the sample.

Background	CSC ID	σ (pb)	EF_{eff} (%)	K	σ_{eff}^{NLO} (pb)	N
WW	005985	70	35	1.594	39.05	50 K
ZZ	005986	11	19	1.348	2.83	50 K
WZ	005987	27	29	1.803	14.06	50 K

bution to the Standard Model backgrounds.
Datasets used for Standard Model backgrounds with the corresponding effective cross-sections are listed in Table 3.3, Table 3.4 and Table 3.5. In the case of $t\bar{t}$ and $QCDjets$ processes (Table 3.3), the effective NLO cross-section is calculated as: $\sigma_{eff} = \sigma \times EF_{efficiency}$. In the case of diboson samples (Table 3.4), the effective NLO cross-section is calculated in the same way and then recalculated to the next-to-leading-order value multiplying by the corresponding K factor.
In the case of background processes generated with ALPGEN (Table 3.5) the effective cross-section is calculated as: $\sigma_{eff} = \sigma \times MLM_{efficiency} \times EF_{eff}$.
K factors for recalculating the cross-sections from leading-order to next-to-leading-order values are 1.15 for W and 1.27 for Z samples.
In Table 3.6, another set of W+jets and Z+jets ALPGEN samples is shown.

Table 3.5: ALPGEN sample CSC ID, production cross-section, parton - jet MLM matching efficiency, event filter efficiency, the effective cross section, K factor for recalculation the ALPGEN cross sections from leading-order to next-to-leading-order values, recalculated cross-section σ_{eff}^{NLO} and the available number of events in the sample.

Bckg.	CSC ID	σ (pb)	$\mathrm{MLM_{eff}}$	$\mathrm{EF_{eff}}$(%)	K	$\sigma_{\mathrm{eff}}^{\mathrm{NLO}}$(pb)	N
W$e\nu$	005223	504	0.5430	0.00244	1.15	0.77	4 K
	005224	122	0.4305	0.06460	1.15	3.90	16 K
	005225	28.4	0.3490	0.20330	1.15	2.32	10 K
	005226	6.1	0.3433	0.28452	1.15	0.69	3 K
W$\mu\nu$	008203	122	0.4309	0.01322	1.15	0.79	4 K
	008204	28.4	0.3490	0.18681	1.15	2.13	10 K
	008205	6.1	0.3503	0.28520	1.15	0.70	4 K
W$\tau\nu$	008208	504	0.5415	0.00196	1.15	0.61	3 K
	008209	122	0.4277	0.05449	1.15	3.27	14 K
	008210	28.4	0.3525	0.26725	1.15	3.08	14 K
	008211	6.1	0.3474	0.38370	1.15	0.94	5 K
Z$\nu\nu$	005124	79.8	0.4213	0.02501	1.27	1.07	40 K
	005125	18.5	0.3417	0.38164	1.27	3.06	48 K
	005126	3.96	0.3424	0.55204	1.27	0.95	14 K
Zee	005161	179.8	0.6755	0.00260	1.27	0.41	1.5 K
	005162	56.4	0.5407	0.10710	1.27	4.15	49 K
	005163	14.1	0.4204	0.36650	1.27	2.76	22 K
	005164	3.26	0.3482	0.48173	1.27	0.70	6 K
	005165	0.7	0.3522	0.56220	1.27	0.18	2 K
Z$\mu\mu$	008109	14.1	0.4213	0.03187	1.27	0.24	11 K
	008110	3.26	0.3431	0.37120	1.27	0.53	5 K
	008111	0.7	0.3522	0.54226	1.27	0.17	2 K
Z$\tau\tau$	008120	56.4	0.5321	0.02579	1.27	0.98	16 K
	008121	14.1	0.4215	0.22551	1.27	1.70	50 K
	008122	3.26	0.3458	0.43747	1.27	0.62	10 K
	008123	0.7	0.3435	0.54129	1.27	0.17	4 K
	008114	56.4	0.5321	0.00565	1.27	0.22	4 K
	008115	14.1	0.4215	0.05448	1.27	0.41	7 K
	008116	3.26	0.3458	0.14466	1.27	0.20	4 K
	008117	0.7	0.3435	0.20196	1.27	0.06	1 K

These samples have been generated using a generator filter that asks for at least one jet with transverse momentum larger than 20 GeV. They will be used in Chapter 4 because the cuts on the two hardest jets of the event and on missing energy used to perform the analysis, are looser than the Standard ATLAS SUSY cuts. For this reason, the samples in Table 3.5 could bias the selection.
With the exception of the J4, J5 and J6 samples, the number of available events in each SUSY and Standard Model background dataset corresponds to about 1 fb^{-1} of data or higher.

3.5 The physical objects

In this section I will describe in details the algorithms employed to reconstruct the fundamental physical objects used in this thesis.

3.5.1 The electrons

In SUSY searches, the requirement of a high p_T electron is normally associated with additional requirements on jets and E^T_{MISS}. As a consequence, for typical SUSY analyses, jet backgrounds are normally already reduced before requiring a lepton. Therefore ultimate rejection on jets is not needed in SUSY studies, and relatively mild electron identification cuts can be applied, leading to a significant gain in efficiency. This is especially useful for searches requiring many leptons.

Identification

The eGamma algorithm [9] was used for the electron identification and reconstruction, with the "medium" cuts [2] recommended by the electron combined performance studies [9] for the ATLAS software with the release 12.0.6 used in this work.
The transverse isolation energy in a cone of $\Delta R < 0.2$ around the electron, computed using the calorimetric information, is used to select isolated electrons. This quantity is required to be smaller than 10 GeV. In the available data sets this variable is not correctly calculated, However this problem introduces only a small bias, except for the crack region $1.37 < |\eta| < 1.52$.

[2] The results of the electron identification algorithms are encoded in the variable isEM; the medium cuts cited here correspond to the cut isEM & 0x3FF == 0 in release 12. This medium electron identification cut combines the information about the energy released in the calorimeter, the shape of the shower and the number of associated hits in the Pixel and in SCT detectors.

Table 3.6: ALPGEN sample (loose generator filter) CSC ID, production cross-section, parton - jet MLM matching efficiency, event filter efficiency, the effective cross section, K factor for recalculation the ALPGEN cross sections from leading-order to next-to-leading-order values, recalculated cross-section σ_{eff}^{NLO} and the available number of events in the sample.

Bckg.	CSC ID	σ (pb)	$\mathrm{MLM_{eff}}$	$\mathrm{EF_{eff}}$(%)	K	$\sigma_{\mathrm{eff}}^{\mathrm{NLO}}$(pb)	N
W$e\nu$	006101	16360	0.818	0.131	1.15	2016	250 K
	006102	4740	0.55	0.631	1.15	1890	250 K
	006103	2029	0.407	0.710	1.15	675	190 K
	006104	770	0.311	0.737	1.15	203	57 K
	006106	273	0.247	0.731	1.15	57	16 K
	006106	89.5	0.268	0.740	1.15	21	5 K
W$\mu\nu$	006107	16360	0.819	0.061	1.15	940	250 K
	006108	4740	0.546	0.628	1.15	1870	250 K
	006109	2029	0.407	0.712	1.15	676	190 K
	006110	770	0.306	0.738	1.15	200	57 K
	006111	273	0.250	0.738	1.15	58	16 K
	006112	89.5	0.272	0.742	1.15	21	5 K
W$\tau\nu$	006113	16360	0.819	0.018	1.15	278	191 K
	006114	4740	0.552	0.133	1.15	400	230 K
	006115	2029	0.408	0.153	1.15	146	41 K
	006116	770	0.311	0.169	1.15	47	13 K
	006117	273	0.248	0.180	1.15	14	4 K
	006118	89.5	0.273	0.194	1.15	5.5	1.2 K
Z$\nu\nu$	006524	79.8	0.4213	0.02501	1.27	1.07	40 K
	006525	18.5	0.3417	0.38164	1.27	3.06	48 K
	006526	3.96	0.3424	0.55204	1.27	0.95	14 K
Zee	008130	933	0.776	0.205	1.27	188	247 K
	008131	340	0.532	0.765	1.27	176	222 K
	008132	153	0.395	0.835	1.27	64	250 K
	008133	61	0.313	0.85	1.27	21	180 K
	008134	22	0.247	0.85	1.27	6	25 K
	008135	7.2	0.276	0.846	1.27	2.1	11 K
Z$\mu\mu$	008142	933	0.776	0.069	1.27	63	84 K
	008143	340	0.533	0.750	1.27	173	222 K
	008144	153	0.400	0.845	1.27	66	250 K
	008145	61	0.313	0.856	1.27	21	180 K
	008146	22	0.246	0.859	1.27	6	26 K
	008147	7.2	0.275	0.848	1.27	2.1	11 K
Z$\tau\tau$	008154	933	0.776	0.066	1.27	61	162 K
	008155	340	0.541	0.310	1.27	72	192 K
	008156	153	0.403	0.346	1.27	28	250 K
	008157	61	0.312	0.366	1.27	9	156 K
	008158	22	0.247	0.381	1.27	2.6	34 K
	008159	7.2	0.276	0.389	1.27	1.0	15 K

An *overlap removal* procedure has also been implemented in order to prevent that the same object to be reconstructed both as an electron and as a jet. An electron is rejected if it is found within a distance $0.2 < \Delta R < 0.4$ of a jet, as in this case it is most likely associated to the decay of a particle within the jet. In case $\Delta R(j, e) < 0.2$ the jet is discarded instead. In the region $1.37 < |\eta| < 1.52$, besides the problem with the isolation variable described above, the electron identification and measurement are degraded because of the large amount of material in front of the calorimeter and the crack between the barrel and extended barrel of the calorimeters [10].
Since in this analyses we require both high quality for the selected electrons and an efficient electron veto, events with a pseudorapidity in the crack region, with and with $p_T > 10$GeV and passing the medium eGamma cuts, are rejected.

Electron performance in SUSY events

In this paragraph I will discuss results of a study of the electron identification performance on the SUSY signal sample SU3 and on leptonically decaying top quarks (sample T1) which constitute a major background for SUSY analyses with leptons. The reconstruction algorithms are optimised to infer the true properties of the generated (*truth*) particles from the detector response as accurately as possible. The resolution is a measure of the quality of those algorithms and is here defined as $(p_T^{\text{reco}} - p_T^{\text{truth}})/p_T^{\text{reco}}$, where p_T^{reco} and p_T^{truth} are the transverse momenta of the reconstructed and the generated electron respectively.
Figure 3.1 shows the mean value of the resolution for each bin as a function of p_T and pseudorapidity (η). Signal and top background shows a very similar behaviour. The upper plot indicates that the truth transverse momenta are underestimated for electrons which have a p_T up to about 140 GeV. This underestimation starts from about 3% of the reconstructed p_T value and remains slightly below 0 for electrons with higher p_T. The lower plot shows that near the cracks (barrel - end-cap transition, η around 1.45) the truth p_T is, on average, up to about 15% higher than the actual measured value, the reason of which can be ascribed to an only partial reconstruction of the electron showering in that region.

The width (RMS) of the resolution distribution gives an idea of how much the p_T resolution of single electrons fluctuates around the mean. In the upper plot of figure 3.2, one can observe that the deviation is strong, up to about 13%, for low p_T values and reaches a stable value of approximately 3% for higher p_T. The η distribution shows again the poorer performance in the crack regions.

Another quantity of interest is the reconstruction efficiency, computed as

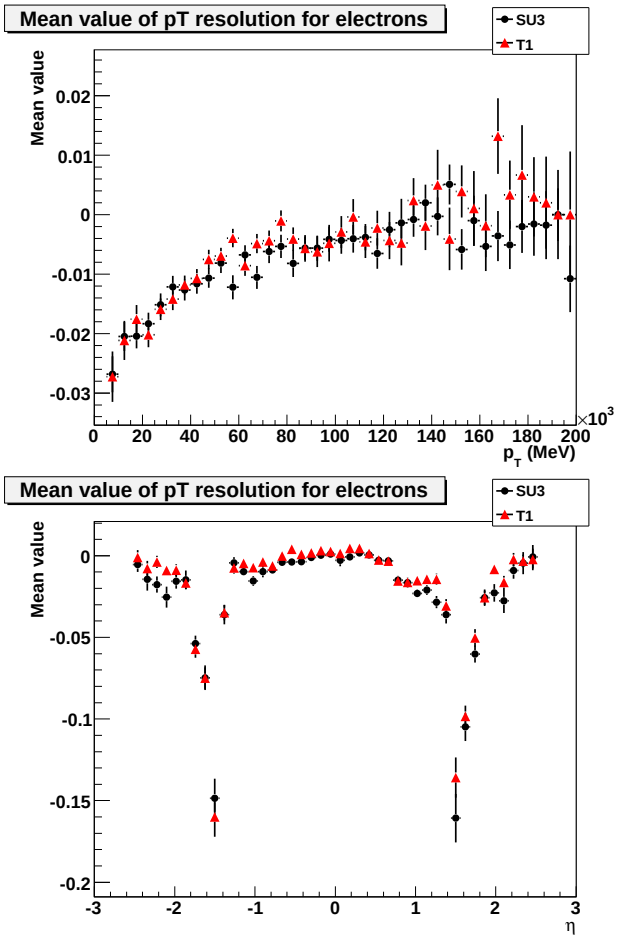

Figure 3.1: Mean transverse momentum resolution for electrons. The upper plot shows the mean value of the difference in p_T of reconstructed and truth electron relative to the reconstructed value, as a function of the reconstructed p_T, the lower plot the same quantity as a function of reconstructed pseudorapidity (transverse momentum required to be bigger than 5 GeV).

a fraction of the generated electrons that are identified in the detector. To get an estimate for this, one tries to find for each isolated truth electron a corresponding reconstructed candidate in close proximity, within a cone of $\Delta R < 0.02$, which is also required to be isolated. The two plots in figure 3.3 show the electron efficiency, respectively as a function of true transverse momentum and true pseudorapidity, again for the two processes SU3 and T1. Considering the upper plot first, one observes an increase in efficiency to a plateau just above 70%, starting from a p_T of about 40 GeV and re-

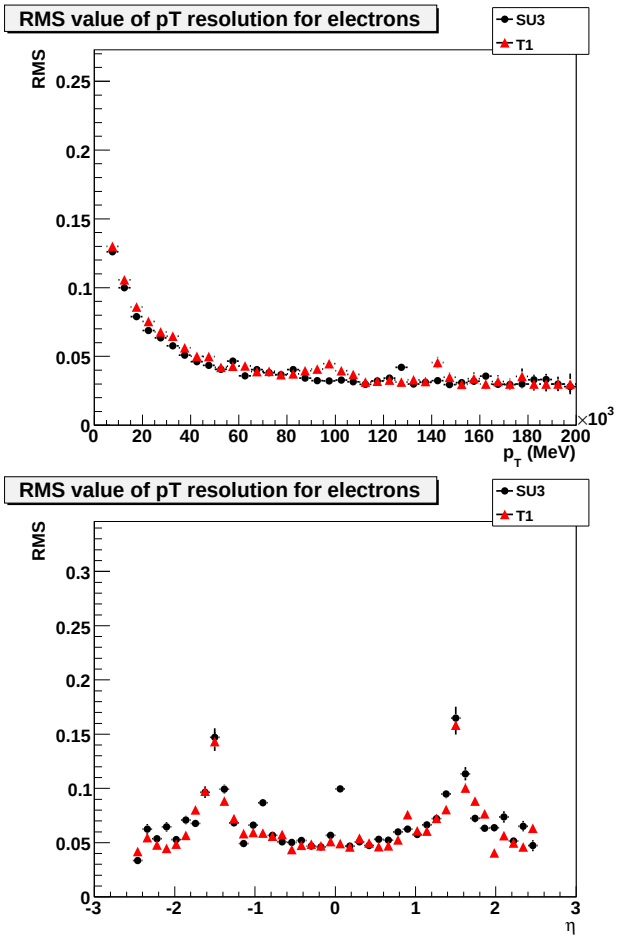

Figure 3.2: RMS of transverse momentum resolution for electrons as a function of transverse momentum (upper plot) and pseudorapidity (lower plot, transverse momentum required to be bigger than 5 GeV).

maining practically stable throughout to high values. The η dependency of the efficiency (lower plot) mirrors the geometry of the detector, showing an efficiency of roughly 80% in the barrel region (below $|\eta| = 1.4$), worse performance of approximately 60% in the end-cap region and substantial drops around the cracks (near $|\eta| = 1.45$). Both processes show a very similar behaviour.

Eventually, one also needs to know how many of the reconstructed electrons are actually jets or taus. Every isolated reconstructed electron, which cannot be matched to a truth one within a cone of $\Delta R < 0.02$, is considered a fake. Contrary to the case for efficiency, the truth electron does not need

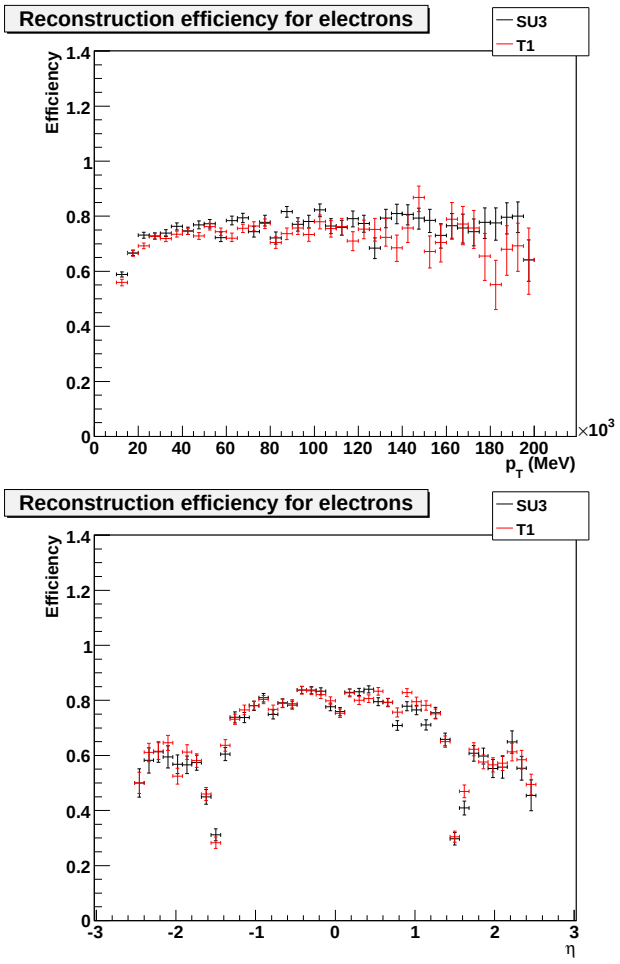

Figure 3.3: Reconstruction efficiency of isolated electrons as a function of true transverse momentum (upper plot) and true pseudorapidity (lower plot, transverse momentum required to be bigger than 10 GeV) for the SUSY signal SU3 and leptonically decaying top quarks (T1).

to be isolated as it often emits Bremsstrahlung, which compromises its factual isolation. One then tries to match those fake electrons to either jets or taus within a cone of $\Delta R < 0.2$. Consequently, the fake probability (or *fake rate*) is defined as the number of true jets/taus which fake electrons divided by the total number of true jets/taus.

The probability for jets to fake electrons is shown in the two plots in figure 3.4, as a function of p_T and η respectively. The fake rate peaks at a p_T value around 40 GeV and decreases for higher energetic electrons, since harder jets

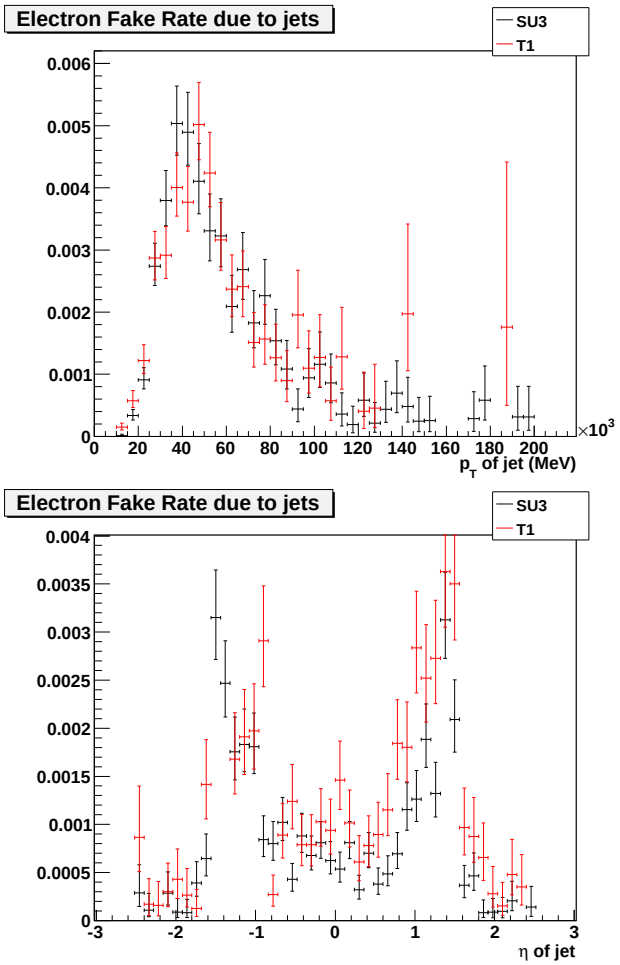

Figure 3.4: Jet-electron fake rate. The upper plot shows the probability for a jet to fake an electron as a function of the true jet transverse momentum, the lower plot the same quantity as a function of true pseudorapidity (transverse momentum required to be bigger than 10 GeV).

have a stronger leakage into the hadronic calorimeter and are, therefore, less prone to be misidentified as electrons. On average, the fake electron has a p_T which is roughly 40% smaller than the one of the corresponding truth jet, the deviation arising from differently tuned reconstruction algorithms for electrons and jets. Not surprisingly, the fake probability is significantly higher in the crack regions (see lower plot). The overall fake probability amounts to about 0.1% for both SU3 and T1.

Tau fake rate is particularly important for SU3, since approximately 50%

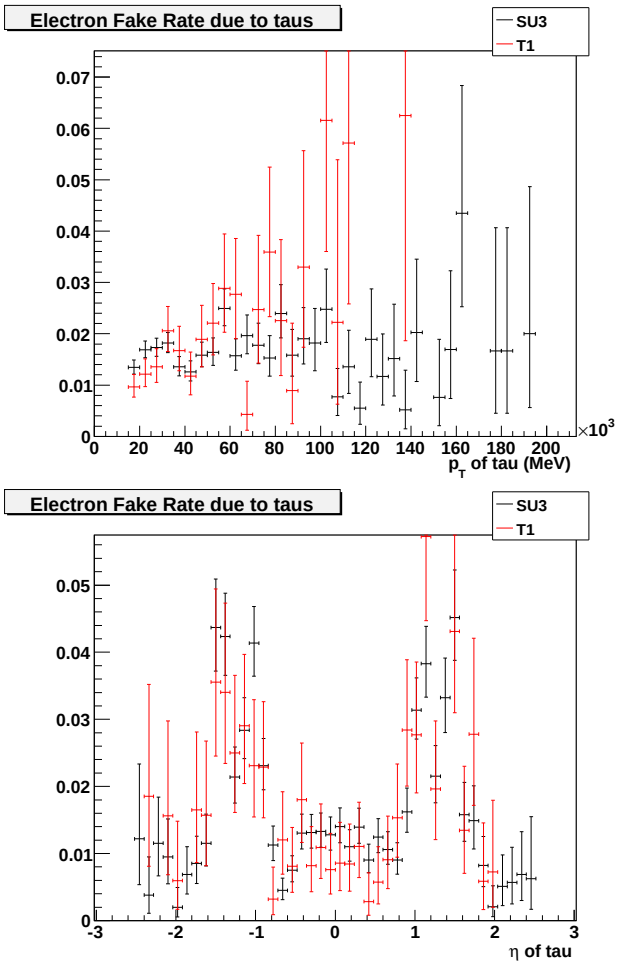

Figure 3.5: Tau-electron fake rate. The upper plot shows the probability for a tau to fake an electron as a function of the true tau transverse momentum, the lower plot the same quantity as a function of true pseudorapidity (transverse momentum required to be bigger than 10 GeV).

of all fake electrons arise from hadronically decaying taus. In the case of T1 they constitute a quarter of all fakes. Figure 3.5 shows again the dependence on p_T and η. The peak in the p_T dependence is not as pronounced as in the case of jets, but the shape of the η-dependence is fairly similar. The overall tau fake probability is about 2%, which is roughly 10 times higher than the jet fake rate.

3.5.2 The muons

Based on muon identification cuts optimised with respect to the SUSY environment, the goal of this section is to perform a comparison between different SUSY samples and between SUSY and the background T1 sample.

Identification

The muons are reconstructed using the *STACO* algorithm, which performs a statistical combination of a MUONBOY track, reconstructed in the muon spectrometer with its corresponding track in the inner detector.
Muons produced by the *MuTag* algorithm, dedicated to the identifications of very low-p_T muons, are discarded. A reasonable quality of combination is guaranteed with a loose requirement that the tracks should match with $\chi^2 < 100$.
If more than one Inner Detector track matched one track from the Muon Spectrometer, only the one with best match (smallest distance ΔR) was kept.
The total calorimeter energy deposited in a cone of $\Delta R < 0.2$ around the muon is required to be less than 10 GeV.
Finally, muons found within a distance $\Delta R < 0.4$ of a jet, are discarded.

Muon performance in SUSY events

The study shown in the following, concentrates once again on the SUSY signal samples SU1, SU3 and SU4, and on leptonically decaying top quarks (sample T1). For a further in-depth treatment of muon performance see [11]. Only statistical errors on the available event statistics are considered.
The kinematical and identification cuts applied for the calculation of the relevant performance figures are given in Table 3.7.
In addition, a reconstructed jet are removed from studies if a reconstructed electron (passing the selection cuts previously listed) is found to be at a distance $\Delta R < 0.2$ from this reconstructed jet. If there is a truth electron (with $p_T > 20$ GeV, $|\eta| < 2.5$ and calorimeter isolation in $\Delta R < 0.2$ less than 10 GeV) at a distance $\Delta R < 0.2$ from a truth jet, then the truth jet is discarded.
The standard muon identification cuts described above, stipulates that if a reconstructed muon is found at a distance $\Delta R < 0.4$ from a reconstructed jet, then the muon is excluded from studies. The studies of efficiencies and fake rates exposed in the following part of this section, are performed both before and after applying this last cut.
The muons in the events can originate from several sources. They are either produced in the decays of "heavy" particles, like SUSY particles, Z and W

Table 3.7: Identification cuts applied on truth and reconstructed muons/jets when computing efficiencies and fake rates.

	p_T(GeV)	$\|\eta\|$ max	E_T^{isol}(GeV)	match χ^2/ndf
Truth μ eff.	20	2.5	< 10	
Reco. μ eff.	15	2.5	< 10	< 20
Truth μ fake	15	2.5		
Reco. μ fake	20	2.5	< 10	< 20
Truth jet	20	2.5		
Reco. jet	20	2.5		

bosons, τ leptons, or they can come from heavy and light flavours decays. There is also the possibility that muons are radiated by other muons in Bremsstrahlung processes (so called G4 muons). Depending on the origin of the muon, three collections of truth muons are used for the definition of efficiencies and fake rates:

1. Muons from decays of "heavy" particles: SUSY, Z, W and τ (Def1);
2. Muons from decays of all particles (SUSY, Z, W, τ, heavy and light flavours), apart from G4 muons (Def2);
3. Muons from decays of all particles, including G4 muons (Def3).

The efficiency is defined as the number of truth muons matched with a reconstructed muon within a distance $\Delta R < 0.02$, divided by the total number of truth muons. The truth muons, according to the first two definitions (Def1 and Def2), are used. The efficiencies as a function of p_T and of η for STACO muons from SU3 and T1 samples, before applying the $\Delta R(\mu, jet) > 0.4$ cut, are shown in Figure 3.6, for truth muons described by Def2. The average efficiency values for the different samples before and after applying $\Delta R(\mu, jet) > 0.4$ cut, are reported in Table 3.8. The fake rate is defined as the number of reconstructed muons without a matching truth muon at a distance $\Delta R < 0.02$, divided by the total number of truth jets. Truth muons from all three definitions (Def1, Def2, Def3) are analysed. Fake rates are reported in Table 3.9 before and after applying the $\Delta R(\mu, jet) > 0.4$ cut. It can be seen in Table 3.8 that muon efficiencies are reasonably consistent for the different SUSY samples. Fake rates, with respect to muons coming from particles described by definitions Def2 and Def3, are statistically compatible in different SUSY and T1 samples and very low, of order 10^{-5}. With respect to muons described by Def1, fake rates are one or two orders of magnitude larger, because they contain also the contribution of reconstructed muons

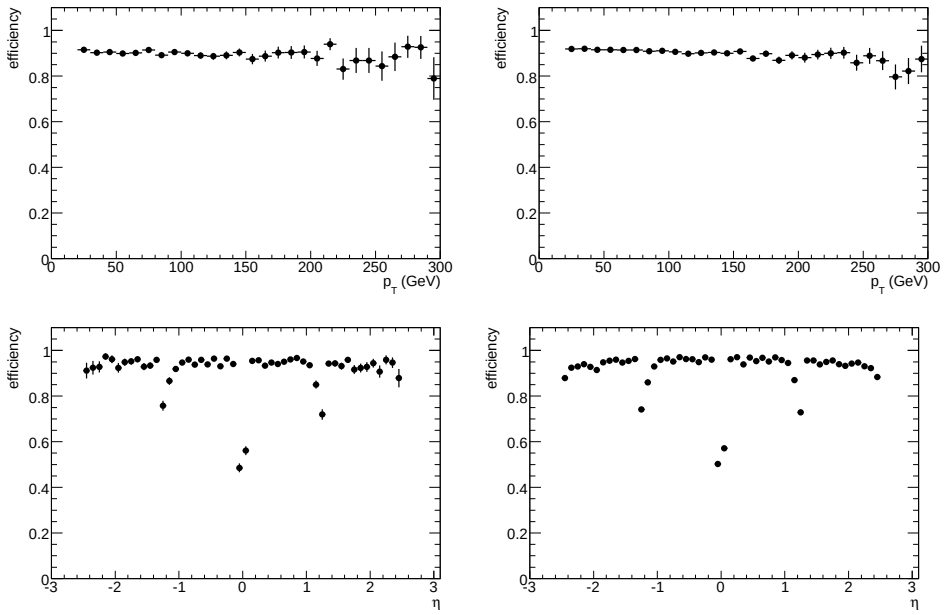

Figure 3.6: STACO muon efficiencies as a function of p_T(top) and η (bottom) for the SU3 sample (left) and T1 sample (right), calculated with respect to truth muons described by Def2. Muon transverse momentum $p_T > 20$ GeV.

Table 3.8: STACO muon efficiencies for SU1, SU3, SU4 and T1 samples before and after applying $\Delta R(\mu, jet) > 0.4$ cut.

	efficiency before $\Delta R(\mu, jet) > 0.4$	efficiency after $\Delta R(\mu, jet) > 0.4$
SU1, Def1 truth μ	90.4(2)%	85.4(2)%
SU1, Def2 truth μ	90.4(2)%	85.4(2)%
SU3, Def1 truth μ	90.3(2)%	84.4(3)%
SU3, Def2 truth μ	90.3(2)%	84.4(3)%
SU4, Def1 truth μ	90.7(2)%	83.4(2)%
SU4, Def2 truth μ	90.7(2)%	83.2(2)%
T1, Def1 truth μ	91.46(7)%	87.06(9)%
T1, Def2 truth μ	91.45(7)%	86.95(9)%

coming from jets. The T1 and SU4 samples (Def1 truth muons) have larger fake rates than SU1 and SU3 events, because of their larger average number of b-jets. The cut $\Delta R(\mu, jet) > 0.4$ reduces fake rates (Table 3.9), especially

Table 3.9: STACO muon fake rates for SU1, SU3, SU4 and T1 samples before and after applying $\Delta R(\mu, jet) > 0.4$ cut.

	fake rate before $\Delta R(\mu, jet) > 0.4$	fake rate after $\Delta R(\mu, jet) > 0.4$
SU1, Def1 truth μ	$4.5(2) \times 10^{-4}$	$1.38(4) \times 10^{-4}$
SU1, Def2 truth μ	$1.4(4) \times 10^{-5}$	$0.4(2) \times 10^{-5}$
SU1, Def3 truth μ	$1.4(4) \times 10^{-5}$	$0.4(2) \times 10^{-5}$
SU3, Def1 truth μ	$4.1(3) \times 10^{-4}$	$1.3(2) \times 10^{-4}$
SU3, Def2 truth μ	$1.4(5) \times 10^{-5}$	$1.3(5) \times 10^{-5}$
SU3, Def3 truth μ	$1.3(5) \times 10^{-5}$	$1.1(4) \times 10^{-5}$
SU4, Def1 truth μ	$12.4(4) \times 10^{-4}$	$3.9(2) \times 10^{-4}$
SU4, Def2 truth μ	$1.5(4) \times 10^{-5}$	$0.7(3) \times 10^{-5}$
SU4, Def3 truth μ	$1.5(4) \times 10^{-5}$	$0.7(3) \times 10^{-5}$
T1, Def1 truth μ	$17.2(3) \times 10^{-4}$	$5.4(2) \times 10^{-4}$
T1, Def2 truth μ	$1.9(3) \times 10^{-5}$	$1.5(3) \times 10^{-5}$
T1, Def3 truth μ	$1.5(3) \times 10^{-5}$	$1.0(2) \times 10^{-5}$

in the case of highly isolated muons from heavy particles decays (Def1).

3.5.3 The jets

Because of the relatively large multiplicity of jets in SUSY events, a narrow cone is preferable in the reconstruction of jets. The algorithm used to reconstruct jets in the analysis documented here is the Cone4Tower algorithm [12] with a cone size of 0.4. Jets matching within a cone of $\Delta R < 0.2$ an isolated electron passing the reconstruction cuts described below are discarded.
The mean and RMS E_T of reconstructed jets in SU3 SUSY events as a function of the jet energy averaged over $\eta < 3$, are shown in Figure 3.7. The calibration is good to $\mathcal{O}(2\%)$, which would be adequate for initial discovery. It should be noted, however, that this calibration was derived using Monte Carlo truth, not from an analysis that could be done with real data.
A jet is identified as a b-jet if the weight from the IP3D+SV1 algorithm [13] is larger than 6.75. This value corresponds to a b-tagging efficiency of 60% and a light jet rejection of about 100 for the signal samples SU3 and SU4.

3.5.4 The missing energy

The p-p collisions at LHC have total transverse missing energy equal to zero by the momentum conservation. Hence the definition of the transverse

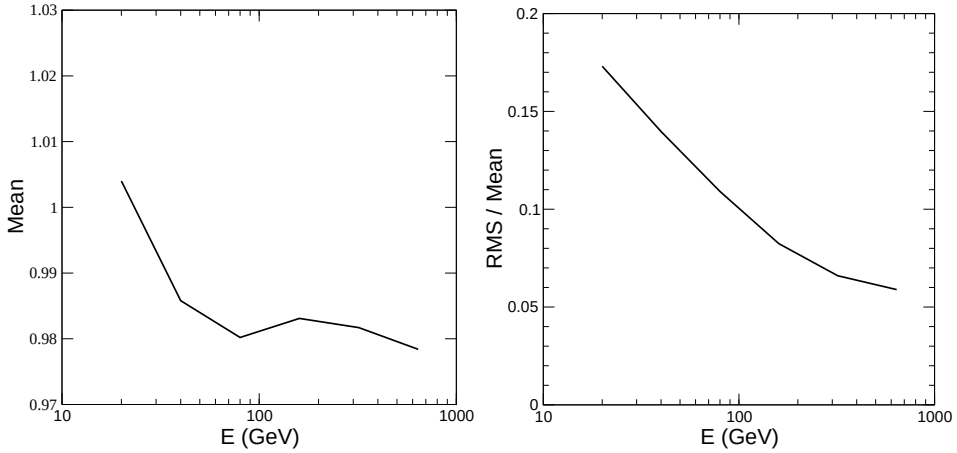

Figure 3.7: Mean and RMS E_T of reconstructed jets in SU3 events compared to Monte Carlo truth.

missing energy E_T^{MISS} is:

$$E^T_{MISS} = \sqrt{{E^X_{MISS}}^2 + {E^Y_{MISS}}^2} \tag{3.1}$$

where $E^{X(Y)}_{MISS} = -\sum E^X(E^Y)$ and $\sum E^X$, $\sum E^Y$ are the sum of the total energies measured in the detector along the X and Y direction. Another important variable is the total transverse energy $\sum E^T = \sum E^X + \sum E^Y$. A precise determination of E^X_{MISS} and E^Y_{MISS} is fundamental for ATLAS, both to study the SM channels involving neutrinos (semileptonic W and top decay, $Z \to \nu\nu$, τ decay) and to give robustness and reliability to the eventual discovery of new physics (SUSY, extra-dimension, etc..). E^T_{MISS} in ATLAS is computed basing on the energy of the calorimetric cells, on the momentum of the muon tracks and on the estimation of the energy lost in the cryostat between the two calorimeters. Let now describe how these three components are evaluated and used to give the estimation of E^T_{MISS}.

- **The calorimetric term**
  This contribution involves only the calorimetric information. It consists in two steps: the selection of the cells contributing to the signal and the calibration of them, taking into account if they are associated to an electromagnetic or hadronic shower.
  The first phase consists in the division of the cells in those belonging to the signal and to the noise. Hence, a powerful algorithm is needed to suppress the noise because of the enormous number of channels (about 200 K) of the calorimeter. For example, the electronic noise

contributes to a worsening of 13 GeV in the E^T_{MISS} resolution (test-beam data). In ATLAS there are two different algorithms to suppress the noise. Both of them need the knowledge of the pure electronic noise (σ_{Noise}) and eventually of the pile-up noise ($\sigma_{pile-up}$), that has been obtained using the test-beam data.
The first algorithm (called "Standard E^T_{MISS}") fixes the thresholds in unity of σ_{Noise}, and it uses the cells with an amount of energy larger than a fixed threshold value in order to compute the contribution to E^T_{MISS}.
The second algorithm uses the cells in the TopoClusters. The TopoCluster is a tridimensional topological cluster in the calorimeter, which is built using the following procedure:

1. Find a cell with an energy larger than $4\sigma_{Noise}$. This cell is called "seed".
2. All the adjacent cells, with energy larger than $2\sigma_{Noise}$, are put together to form a proto-cluster around the "seed" cell.
3. The cells with energy larger than $0\sigma_{Noise}$ are find and used as "border cells" of the TopoCluster.
4. An algorithm separates the overlapping clusters, assigning the shared cells to different TopoClusters.

So that, the x and y components of the non-calibrated calorimetric term contributing to E^T_{MISS} are computed at the electromagnetic scale using only the cells owing to the TopoClusters:

$$E^{X(Y),CALO}_{MISS} = -\sum E_X(E_Y) \tag{3.2}$$

and the same for the total transverse energy using only the total transverse energy of each TopoClusters cell.
The second phase is the calibration procedure.
Due to the fact that, in ATLAS, the calorimeters have different behaviour with respect to hadronic and electromagnetic particles, the cells have to be calibrated in a different way whether they belong to an hadronic or an electromagnetic cluster.
The calibration method (called Refined Calibration) calibrates the cells after the association to the reconstructed physical objects they belong to. Hence, once the cells in the TopoClusters have been selected by the noise suppression algorithm, the TopoClusters are associated to the reconstructed physical objects, following the association order below:

1. Electrons and photons;
2. Taus;
3. b-jets;
4. Jets;
5. Muons.

Each of these objects is identified using the ATLAS identification criteria, similar to those exposed in the previous sections for electrons, muons and jets. The cells are then associated to the objects and the ambiguities are solved associating the various shared cells to the objects following the order exposed above. Once the association cells maps has been performed, the algorithm loops on the TopoCluster cells not yet present in the various association maps and considers them as a contributions to E^T_{MISS} from not reconstructed objects.
The final contribution to E^T_{MISS} is recorded separately for each physical object and, the calorimetric term, is the sum of the missing energy related to each physical reconstructed object and of the contribution related to the not reconstructed objects. The same procedure is applied to compute the total transverse energy. The cells belonging to electrons, photons and muons, are left at the electromagnetic scale while those associated to τ-jets, b-jets, jets and the external cells are calibrated using the H1 method, where different weights are assigned to the cells based on their energy, their position in the (η,ϕ) plane and on the calorimetric region they belong to (barrel, forward, end-cap).

- **The cryostatic term**
  This term, takes into account the energy lost by the particles in the dead materials of the detector (e.g. not or poor instrumented regions of the detector), and, in particular, in the cryostat between the electromagnetic and hadronic calorimeter.
  The energy of the jets is then corrected by a factor that describes this loss of energy, and the impact of the correction on the jet energy scale can reach the 5% for jets with $p_T > 500$GeV.

- **The muonic term**
  The muon contribution to E^T_{MISS} is computed using the information on the energy of the muons. In order to avoid a double counting of the energy lost in the calorimeter, already taken into account in the calorimetric term, only the information from the spectrometer are used for this purpose.
  Further information coming from the Inner Detector are used (e.g the

χ^2 match between the two combined tracks), in order to suppress the probability to have contributions from fake muons.

This reconstruction and calibration procedure to compute E^T_{MISS}, needs to be validated with early data at LHC. In order to reach this goal, an important work of "event cleaning" will be necessary to understand and take under control the instrumental effects of the detector, before to start any kind of physics analysis using E^T_{MISS}. In particular, the E^T_{MISS} calculation in the early phase should try to use as less as possible the reconstructed objects, until their identification algorithms will be robust and reliable. Once the particle identification will reach this level of maturity, the procedure exposed above will start using also the information coming from the minimum bias events (where E^T_{MISS} should be zero) and from particular physics channels like $Z \rightarrow \tau\tau$.

E^T_{MISS} performances in SUSY events

For the studies presented here, the output of the most refined algorithm for the reconstruction of the transverse missing energy, known as *MET_RefFinal*, was used [14]. [3]

We assume that the scale and resolution for this variable are understood. Sources of fake missing energy, such as dead or noisy parts of the calorimeter, fake muons, beam-gas and beam halo events, cosmic rays and electronics problems are not considered here. A detailed discussion of the strategies to remove sources of fake E_T^{MISS} in early data and to measure the E_T^{MISS} resolution and scale can be found in [14]. The resolution on transverse missing energy is shown in Fig. 3.8 (from [10]) as a function of ΣE_T, the scalar sum of the transverse energies of calorimetric cells. SUSY events are characterised by large values of ΣE_T, and have a resolution which is similar to that of Standard Model processes with the same value of this variable.

This resolution is much smaller than the typical analysis cuts. The Standard Model background is thus expected to be due to either events with true missing energy (that is, hard neutrinos) or to non-gaussian tails in the missing energy resolution.

The latter contribution can be strongly suppressed by requiring a minimum angular separation between the E_T^{MISS} vector and the leading jets in the event. This cut also suppresses the contributions from jets containing hard neutrinos from the leptonic decays of charmed and beauty mesons, even if

[3] For the data samples simulated with a Geant4 range cut of 1 mm, the missing energy was recalculated after correcting for the resulting average miscalibration of electrons, tau, and jets. The correction is small and within the systematic error on the missing energy scale used to evaluate systematic errors.

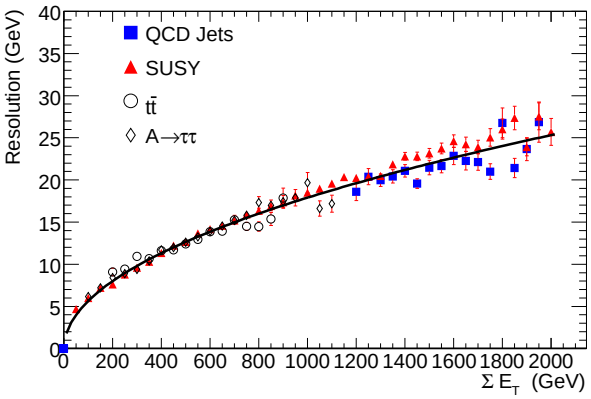

Figure 3.8: Resolution of the two components of the E_T^{MISS} variable as a function of the total transverse energy ΣE_t in the calorimeters for different processes.

this contribution to fake E_T^{MISS} is already strongly suppressed in the dilepton channel, by the request to have two isolated leptons with high p_T.

3.6 Useful variables

3.6.1 The effective mass

The effective mass is a measure of the total activity in the event. In the analysis reported here, it is computed as the scalar sum of the p_T of the 4 leading jets with $|\eta| < 2.5$, missing energy, and leptons. This variable is useful in discriminating Standard Model and SUSY events. It has also the interesting properties that, for SUSY events, it peaks at a value which is strongly correlated with the mass of the pair of SUSY particles, produced in the pp interaction. It can therefore be used to measure the mass scale of SUSY events [15].

3.6.2 The transverse sphericity

The transverse sphericity is useful since SUSY events are, on the average, more spherical than the backgrounds after applying typical analysis cuts on jets and missing energy. Here it will be computed using all jets with $|\eta| < 2.5$ and $p_T > 20$ GeV, and the leptons.

The definition of the transverse sphericity is:

$$S_T = \frac{2\lambda_2}{\lambda_1 + \lambda_2} \tag{3.3}$$

where λ_1 and λ_2 are the eigenvalues of the 2×2 sphericity tensor $S_{ij} = \Sigma_k \mathbf{p}_{ki}\mathbf{p}_{kj}$. The tensor is computed using all jets with $|\eta| < 2.5$ and $p_T > 20$GeV, and all selected leptons. SUSY events tend to be relatively spherical ($S_T \approx 1$), since the initial heavy particles are usually produced approximately at rest in the detector and their cascade decays emit particles in many different directions. QCD events are dominated by back-to-back configurations ($S_T \approx 0$).

3.6.3 The transverse mass

The transverse mass M_T is defined by:

$$M_T^2 = (E_T^\beta + E_T^{MISS})^2 - \mathbf{p}_T^\beta \cdot \mathbf{p}_T^{MISS} \tag{3.4}$$

where $\mathbf{p}_T^\beta$ and E_T^β are, respectively, the transverse momentum and the transverse energy of some visible particle, and $\mathbf{p}_T^{MISS}$ is the missing-transverse-energy two-vector.
This variable is useful when one parent particle decays to one visible and one invisible daughter particle, for example $W \to e\nu$ where it is clear that the mass of the invisible particle (neutrino) can indeed be safely neglected.

Bibliography

[1] S. Frixione and B.R. Webber, JHEP 0206 (2002) 029 [hep-ph/0204244];

[2] HERWIG 6.5, G. Corcella, I.G. Knowles, G. Marchesini, S. Moretti, K. Odagiri, P. Richardson, M.H. Seymour and B.R. Webber, JHEP 0101 (2001) 010 [hep-ph/0011363]; hep-ph/0210213
S. Moretti, K. Odagiri, P. Richardson, M.H. Seymour and B.R. Webber, JHEP 0204 (2002) 028 [hep-ph/0204123];

[3] Prospino2, http://www.ph.ed.ac.uk/tplehn/prospino/;

[4] M.L. Mangano, M. Moretti, F. Piccinini, R. Pittau, A. Polosa, JHEP 0307:001,2003, hep-ph/0206293.;

[5] T.Sjostrand, S. Mrenna, P.Skands, CERN-LCGAPP-2007-04, FERMILAB-PUB-07-512-CD-T (2007);

[6] B. Kersevan and E. Richter-Was, Comput. Phys. Commun. 149 (2003) 142.

[7] S. Agostinelli, J. Allison, K. Amako et al., Nuclear Instruments and Methods in Physics Research A 506 (2003) 250-303,
J. Allison, K. Amako, J. Apostolakis et al. IEEE Transactions on Nuclear Science 53 No. 1 (2006) 270-278;

[8] M.L.Mangano, hep-ph:/0602031 (2002);

[9] ATLAS Collaboration, Expected Performance of the ATLAS Experiment, Detector, Trigger and Physics. Electron/Photon CSC Chapter, CERN-OPEN-2008-020, Geneva, 2008, to appear.

[10] ATLAS Collaboration, The ATLAS Experiment at the CERN Large Hadron Collider, paper submitted to JINST;

[11] ATLAS Collaboration, Expected Performance of the ATLAS Experiment, Detector, Trigger and Physics. Muon Combined Performance CSC Chapter, CERN-OPEN-2008-020, Geneva, 2008, to appear.

[12] ATLAS Collaboration, Expected Performance of the ATLAS Experiment, Detector, Trigger and Physics. Jet, Missing Et and Tau Combined Performance Chapter, CERN-OPEN-2008-020, Geneva, 2008, to appear;

[13] ATLAS Collaboration, Expected Performance of the ATLAS Experiment, Detector, Trigger and Physics. The Expected Performance and Calibration of ATLAS b-Tagging Algorithms Chapter, CERN-OPEN-2008-020, Geneva, 2008, to appear;

[14] ATLAS Collaboration, Expected Performance of the ATLAS Experiment, Detector, Trigger and Physics. Jet, Missing Et and Tau Combined Performance Chapter, CERN-OPEN-2008-020, Geneva, 2008, to appear;

[15] D.R.Tovey, SN-ATLAS-2002-020 (2002) and EPJ Direct: 4 (2002) pp. N4;

Chapter 4

Discovery potential in the 2 leptons channel

4.1 Introduction

In this chapter, I will focus on finding a reliable and robust technique to estimate the Standard Model (SM) background in the dileptonic+jets+missing energy channel, using the so-called "data driven" approach. As the name suggests, this approach has the peculiarity to be based uniquely on the information available in the real data, using only in a marginal way the Monte Carlo.
Even if this channel has a lower $S/\sqrt{B}$ ratio (due to leptonic branching ratio that lowers the signal) with respect to zero lepton+jets+missing energy or one lepton+jets+missing energy channels, it gives a clearer signature because of the presence of two isolated leptons that can be precisely measured even with early data and it has also a useful trigger redundancy between the leptonic and the jet-missing energy triggers, as will be explained in the following. For these motivations, the discovery potential of this channel in the first LHC phase with this channel can be competitive with respect to other signatures.
Hence, the focus here is on the first hundreds of pb^{-1} of collected data, that should allow a possible SUSY discovery in the low mass regions of the mSUGRA parameter space. This explains the choice of SU4 as a benchmark SUSY signal point (see section 3.4 for the point definition in the mSUGRA space and for the mass spectrum) and the choice to quote the results for luminosities of 100 pb^{-1} and 1 fb^{-1} .
In this chapter, I will explain the estimation method chosen to reach this aim (section 4.2), the kinematical variables analysed to distinguish the Standard Model events from the SUSY events (section 4.3), the event selection

procedure (section 4.4) and, finally, the evaluation of the competitiveness and robustness of this method to perform a SUSY discovery in this channel with early data in one of the SUSY benchmark points(section 4.5). A scan of the whole mSUGRA parameter space in order to evaluate the discovery potential of the channel in a more exhaustive way is also presented (section 4.6).

4.2 The estimation method

As previously exposed, the purpose of this method is to estimate the SM background in this channel using only the information gathered from data. The main idea of this method is to estimate the contribution of the SM background in the regions where the signal (SUSY in this case) should dominate starting only from the information on the distribution of some key variable (like E^T_{MISS} or effective mass) in the regions where instead the SM background should dominate.
The starting point is then to find at least two variables that behave as differently as possible in the presence of Standard Model events and SUSY events. Furthermore these variables should not be correlated for the SM events. The latest requirement is fundamental, as will be evident in the following, because the correlation constitutes a source of systematic uncertainties of the method that can worsen the quality of the estimation procedure.
Analyzing the distributions of these variables for SM and SUSY events, for example in our case E^T_{MISS} and the transverse mass M_T (see section 3.6 for the definition), two fundamental regions for each of the variables are identified, by the use of some kinematical cuts: the Control Region (CR) where the SM events dominate over the SUSY signal and the Signal Region (SR) where the SUSY events dominate over the SM background. A total of four regions are then defined within this hypothetical plane. Fig.4.1 shows an example using E^T_{MISS} and the transverse mass M_T. I will use it as a reference to explain the core of the estimation procedure.
Most of the SM background events should lie in the A region, while most of the SUSY events should stay in the D region. In the B and C regions, instead, the SM and the SUSY events are both present.

The extreme importance of the choice of two uncorrelated variables is due to the fact that the estimation procedure assumes that the shape of the distribution of one of these two variables (E^T_{MISS} in the example) will be the same, independently on the position of the kinematical cut on the other variable (M_T in the example). This is obvious by definition if the two

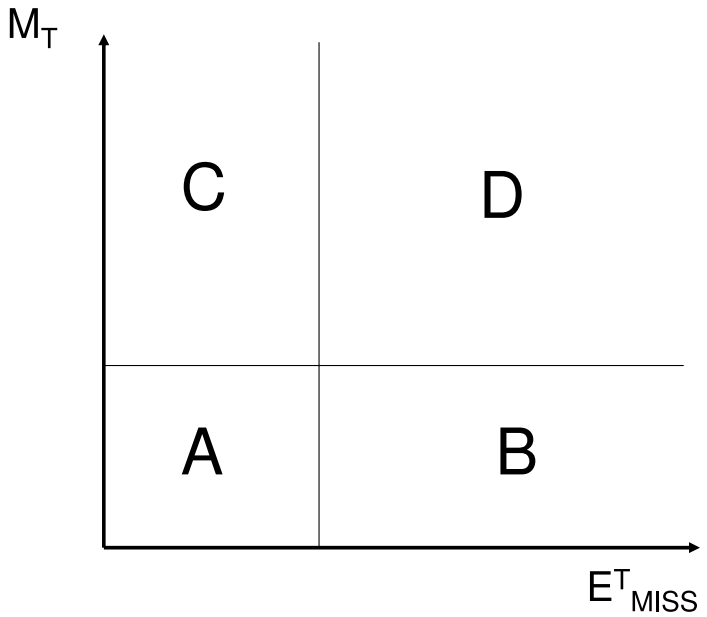

Figure 4.1: Example of the estimation procedure explained in the text, for the pair of variables transverse missing energy (E^T_{MISS}) - transverse mass (M_T).

variables are not correlated, but it can be a source of systematic error if they are correlated.
In case of poor or absent correlation, one can be safely confident that the E^T_{MISS} distribution of the SM events in the D region is obtained rescaling the E^T_{MISS} distribution in the B region, by a factor that is the ratio between the number of events in the C region and those in the A region. This rescaling allows to normalize the E^T_{MISS} distribution for events with low M_T (A region) to the total E^T_{MISS} distribution (that includes both the SUSY signal and the SM background) in a region where E^T_{MISS} is low and then, probably, dominated by events produced by SM processes. The rescaled E^T_{MISS} distribution in the region characterised by high E^T_{MISS} and M_T values (D region) is the estimation of the contribution coming from the SM processes to the tail of the total (SUSY signal + SM background) E^T_{MISS} distribution.
The presence of SUSY signal should then appear if the total and rescaled E^T_{MISS} distributions in the D region are different, showing an excess of events characterised by high E^T_{MISS} values and then, probably, related to a SUSY sparticle production.
As one can notice, the method itself is very simple, and in particular it makes use uniquely of information available in the data, like the E^T_{MISS} or M_T distributions, that are supposed to be "under control" before to perform such an analysis. However, there are a couple of aspects that can lead to a wrong estimation of the SM background, then have to be carefully taken into account.
The first aspect is related to the possible correlation between E^T_{MISS} and the other variable involved in the procedure (M_T in the example). As I will show later, the correlation can become a huge problem, because the shape of the E^T_{MISS} distribution in the regions below and beyond the cut in M_T is different depending on the position of the cut. The effect of such a correlation is a wrong estimate of the shape of the E^T_{MISS} distribution in the Signal Region, causing a systematic error of under/overestimation of the SM contribution in the Signal Region. This error has to be considered as an "intrinsic" error of the method, because the estimation fails even if only the SM background is present.
The second aspect concerns the contamination of the SUSY signal in the Control Region. In this case, the effect is essentially limited to the rescaling factor, but it leads to an overestimation of the SM contribution in the Signal Region that reduces the excess of SUSY events in that region, affecting the discovery potential in that channel.
Both these aspects will be treated in the next sections evaluating accurately their contributions to the systematic errors.

4.3 The discriminating variables

In this section I will analyze the more interesting and useful kinematical variables that allow to discriminate between the SM and the SUSY events, taking into account their possible correlation with missing energy.
To find out these variables it is necessary to analyze first the kinematics of the channel, understanding the main SM background contributions and their difference with respect to the SUSY signal.
As usual in the mSUGRA framework, the SUSY signal in this channel is characterised by a large amount of missing transverse energy due to LSPs, high-p_T jets from the squarks and gluino decays and two isolated leptons.
The most important of the SM backgrounds is the $t\bar{t}$ production. In these events the two leptons and E^T_{MISS} come from the semileptonic decay of W's coming from the decays of both tops. These events provide the signature of two isolated leptons, missing energy due to neutrinos and jets from the two b quarks. The remaining SM backgrounds to SUSY events come from the production of W+jets, Z+jets, the associated production of two gauge bosons (WW, ZZ and WZ) and QCD events, even if the contribution of the latest is negligible because of the requirement of two isolated leptons and high missing energy.
So that, I have examined three variables that can be useful to perform this discrimination between SUSY signal and SM background. They are defined as follows:

- **HT2**
  Defined as $p_T^{lep1} + p_T^{lep2} + p_T^{2ndjet} + p_T^{3rdjet} + p_T^{4thjet}$ (the hardest jet is not included in order to avoid a possible correlation with E^T_{MISS} due to mismeasurement of the energy of the hardest jet itself). This variable should discriminate the SUSY signal from the SM background because in general SUSY events have a larger number of energetic jets.

- **m(lj)**
  Defined as the invariant mass between one lepton and one jet in the event, it should discriminate the SUSY signal from the SM background because of the presence of a kinematical endpoint at $\sqrt{m^2_{top} - m^2_W}$ (in the limit of massless b quark) if the lepton and jet come from the decay of the same top quark. For SUSY events, this kinematical limit is not present.
  In this case, the two leptons and the two hardest jets are used to build the invariant mass. This creates an ambiguity because four lepton-jet pairs are possible, but only two couples of pairs are meaningful. In particular, calling l_1, l_2 the two leptons and j_1, j_2 the two hardest jets of the events, only the couples $(l_1 - j_1, l_2 - j_2)$ and $(l_1 - j_2, l_2 - j_1)$ have

physical meaning, because the semileptonic top decay is reconstructed. If the association is correct, both the $l-j$ pairs in one couple are below the kinematical endpoint, and then the pair with largest invariant mass is taken into account. The same is done for the other couple of pairs and between the two selected pairs, the one with lowest invariant mass is considered, because surely below the endpoint. If instead the association is wrong the selected $l-j$ pair will constitute the combinatorial background beyond the kinematical endpoint.

- M_T
  Defined as the invariant mass in the transverse plane between one of the leptons and the missing transverse energy (see section 3.6 for the exact definition). This variable is useful to discriminate between SUSY signal and SM background because, in case of semileptonic W decay where the only source of missing transverse energy is the neutrino, this invariant mass in the transverse plane has necessarily a kinematical limit given by the W mass. In SUSY events, similarly to the m(lj) variable case, this kinematical limit does not exist because of the different correlation between the leptons and the source of E^T_{MISS} that are the LSPs.
  Also in this case there is an ambiguity due to the choice of the lepton that is used to evaluate the transverse mass. Here the ambiguity is solved keeping the combination with lowest transverse mass, because of its greater discrimination power with respect to the other combination.

In the next section all these variables will be used to perform the SM background estimation with the method previously explained.

4.4 The event selection

The focus of this work is on evaluating the discovery potential in the dileptonic channel with early data. Therefore the event selection has been optimised for this purpose, in contrast, for example, with the selection criteria used in the next chapter, where the focus will be on the reconstruction of the kinematic of the events after the SUSY discovery. In addition, the sensitivity to the low mass regions of the mSUGRA parameter space, necessarily leads to a general softening of the kinematical cuts with respect to the usual selections used to perform both an inclusive and an exclusive search (as in the next chapter or for example in [1]).

The event selection (see section 3.5 for the definition of the physical objects) used here is performed requiring:

- $E^T_{MISS} > 60$GeV;
- Two jets with $p_T > 30$GeV, but one jet with $p_T > 50$GeV;
- Exactly two Opposite Sign leptons with the identification criteria explained in the section 3.5 and with $p_T > 15$GeV and $|\eta| < 2.5$;

The choice to use relatively soft cuts on E^T_{MISS} and the transverse momenta of the jets, is also driven by the idea to have as more SM events as possible in the Control Region, in order to verify the goodness of the method rather than to have the maximum discriminating power between the SUSY signal and the SM background, at least for early data.
The presence of the single leptonic triggers $\mu 20$ and $e25i$ (e.g. one isolated muon with $p_T > 20$GeV or one isolated electron with $p_T > 25$GeV) and the double leptonic trigger $2\mu 10$ and $2e15i$ (e.g. two isolated muons with $p_T > 10$GeV or two isolated electrons with $p_T > 15$GeV) should give a good efficiency and reliability also with early data, while the jet-missing energy trigger $xE70j70$ (e.g. $E^T_{MISS} > 70$GeV and $p_T > 70$GeV for the hardest jet), that usually recovers a significant part of the events giving an important trigger redundancy, here is not useful due to the low threshold for the cuts on E^T_{MISS} and on jets. The trigger menu available in the CSC samples used here is defined for an instantaneous luminosity of $10^{33}\text{cm}^{-2}\text{s}^{-1}$. But our goal is to evaluate the discovery potential with early data, where probably the instantaneous luminosity will be of order of $10^{32}\text{cm}^{-2}\text{s}^{-1}$. In this case, obviously, the various thresholds (especially for the missing energy-jet trigger) will be generally lower than the thresholds that will be used at luminosity of 10^{33} . Hence the decision has been taken to orientate the analysis for a trigger menu of lower luminosity, even if specific triggers for this luminosity are not available in the generated Monte Carlo samples. Possible thresholds for low luminosity triggers could be $2\mu 10$ and $2e10i$ for the leptonic trigger and $2j42xE30$ for the missing energy-jet trigger.
Anyway, the trigger efficiencies in the high luminosity scenario for the selection cuts in the SU4 signal sample in Table 4.1 show that only the 9% of the events is not triggered by the leptonic triggers ($\mu 20$, $e25i$, $2\mu 10$ and $2e15i$) and that the inefficiency rate lowers to 3% if one use also the information from the jet-missing energy trigger ($xE70j70$).
The number of events that pass the cuts above on missing energy, jets and leptons is shown in Table 4.2.
As expected the main SM background is from $t\bar{t}$ events, that are the 90% of the whole SM background. The other important contributions (4% each one)

Table 4.1: Efficiencies, on the SU4 benchmark point events, of the leptonic and missing energy-jet triggers, described in the text for the higher luminosity scenario at $10^{33}\text{cm}^{-2}\text{s}^{-1}$ ($\mu 20$ and $e25i$ for the single lepton trigger, $2\mu 10$ and $2e15i$ for two lepton triggers and $xE70j70$ for the missing energy-jet trigger). The four columns represent the trigger efficiencies respectively for: both leptonic and missing energy-jet triggers passed, only the leptonic trigger passed, only the missing energy-jet trigger passed, no triggers passed. Each trigger refers to the complete chain from L1 to EF. The first row shows the efficiencies for the requirement of only two isolated leptons, while the second row shows the efficiencies after adding the cuts on missing energy and jets.

CUTS	LEPT.+MET	LEPT. ONLY	MET ONLY	NO TRIG.
2 lept.	51.1 %	39.8 %	4.7 %	4.4 %
2 lept.+ jets+MET	61.4 %	29.5 %	5.9 %	3.2 %

come from Z+jets, when the Z decays into two muons or two taus. Events where the Z decays into two electrons, having more precise determination of missing energy than in the muon or tau case, give small contribution to the SM background because they do not pass the cut on missing energy.
The remaining 2% of the SM background comes from the other decays of the Z, from gauge bosons production and from W+jets events.
The QCD events do not contribute to the SM background, but due to the huge cross-section for these events, a limited statistics is available for these samples (order of some pb^{-1}). The tails of the missing energy distribution in these events are then difficult to control and can contribute to the total number of events passing the cuts.

In Fig.4.2 are shown the distributions of the three discriminating variables (respectively HT2, m(lj) and M_T) for the SU4 signal and the SM backgrounds. The vertical lines show the position of the cuts on each variable. These cuts will be used in the next section to define the Control Region and the Signal Region in the background estimation procedure.
The main contribution to the SM background comes from the $t\bar{t}$ events (solid gray line) as expected.
These cuts have been optimised trying to keep the SU4 signal contamination in the Control Region as low as possible, but ensuring, in the same time, a number of SM events in that region large enough to keep low the statistical error of the extrapolation.

Table 4.2: Cut-flow of the events passing the cuts on leptons, missing energy and transverse momenta of the two hardest jets for the SU4 signal sample and for the SM backgrounds samples (defined in the section 3.2) considered here. The thresholds for the cuts are explained in the text. All the numbers are normalised to 1 fb^{-1}.

	Lepton+E^T_{MISS}+jet cuts
SU4	7279
$t\bar{t}$	8025
WW	29
WZ	13
ZZ	7
$W \to e\nu$+jets	61
$W \to \mu\nu$+jets	42
$W \to \tau\nu$+jets	31
$Z \to ee$+jets	29
$Z \to \mu\mu$+jets	183
$Z \to \tau\tau$+jets	147
$Z \to b\bar{b}$+jets	16
$Z \to \nu\nu$+jets	0
QCD (J3-J7)	0
TOTAL SM	8583

Table 4.3: Number of events for the SUSY signal and the SM background in the Control Region and in the Signal Region, for the three discriminating variables considered. The definition of the Control and Signal regions is given in the text. All the numbers are normalised to 1fb^{-1}

	Control Region		Signal Region	
	SM	SU4	SM	SU4
HT2	4502	1331	4081	5948
m(lj)	5437	2309	3146	4970
M_T	3434	1723	5149	5556

The final cuts on these variables used to discriminate the Control Region from the Signal Region are the following:

- $HT2 < 200\text{GeV}$;
- $m(lj) < 120\text{GeV}$;
- M_T in the window 60-100 GeV;

In Table 4.3 is shown the number of events for SU4 signal and SM background in the Control Region (CR) and in the Signal Region (SR). Notice that the contamination of SUSY signal in all the three Control Region is about 23% for HT2 variable, 30% for m(lj) but it reaches the 34% for the transverse mass M_T. This aspect will be discussed in the next section, when the estimation procedure will be performed.

4.5 Evaluation of the discovery potential

Once the cuts have been defined, it is necessary to identify the normalization region. In order to have a reliable and robust extrapolation, the normalization has to be done in the E^T_{MISS} regions, where the contribution of the SM events is higher than the contribution of the signal. In fact, the contamination, as previously mentioned, is crucial in this step of the procedure, leading to a possible overestimation of the SM background in the signal region, with the consequence to mask a potential excess of the signal with respect to the background.
Hence it seems natural to choose the low E^T_{MISS} region, where the SM backgrounds dominate over the SUSY signal. Given that the event selection cut on E^T_{MISS} is 60 GeV, the normalisation region has been fixed in two different ranges: 60-100 GeV and 60-120 GeV.

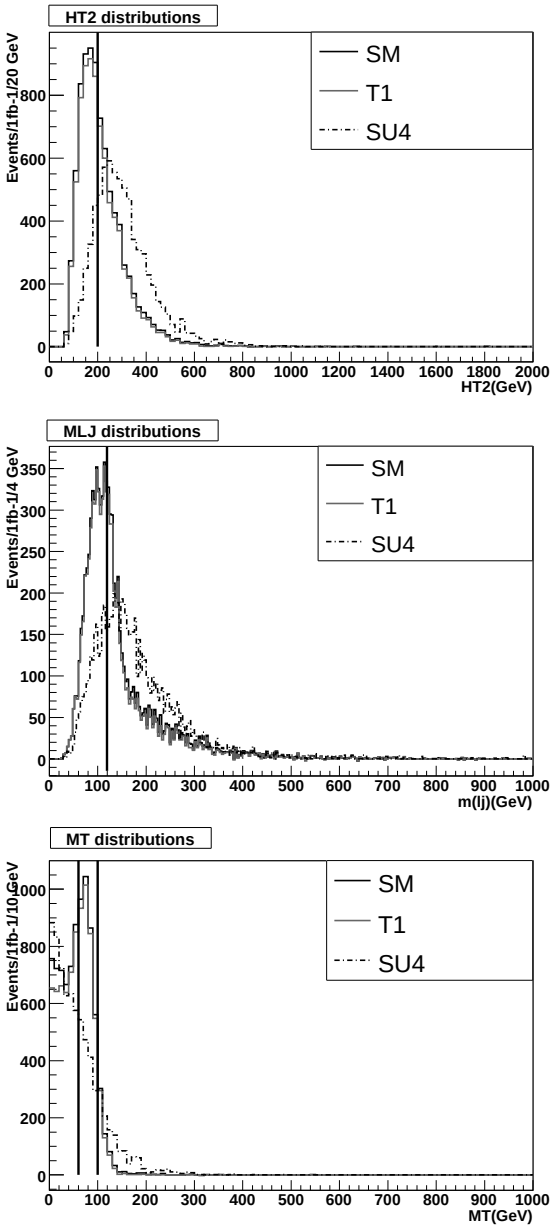

Figure 4.2: Distribution of the three discriminating variables used to define the Control Region. For all the plots, the black solid line represents the contribution of all the SM considered backgrounds, the gray solid line represents the $t\bar{t}$ contribution to the SM backgrounds and the dashed line represents the contribution of the SU4 signal. The vertical lines show the position of the cuts used to defined the Control region, as described in the text. All the distributions are normalised to 1 fb^{-1}.

The three variables have been evaluated and compared taking into account two requirements. The first one is that each variable has to ensure the correct result of the method itself when only the SM background is present, avoiding the principal source of systematic that is the correlation between E^T_{MISS} and the discriminating variables.
Then, for each variable, the significance of the signal over background excess is evaluated in the Signal Region, where the background was determined using the estimation procedure. The contamination in the Control Region can mask the effect of this excess and, then, has to be carefully examined and possibly reduced.
The tables 4.4 and 4.5 show, for the three evaluated discriminating variables, their capability to estimate the SM background when only the SM background itself is present as a function of the E^T_{MISS} normalisation region. The table 4.4 assumes a normalisation region of 60-100 GeV, while the table 4.5 assumes a normalisation region of 60-120 GeV.
Both the HT2 and m(lj) variables systematically underestimate the number of events in the Signal Region (e.g. for $E^T_{MISS} > 120(100)$ GeV). This underestimation can reach the 40% if the normalisation region is 60-120 GeV, while lowers to about 30% if the normalisation region is narrower. The discrepancy between the true and the estimated number of events is largely incompatible with the statistical error, that is of 3-4% for both the variables in both the normalisation regions. The underestimation itself and the fact that it varies for different normalisation regions, suggest that HT2 and m(lj) variables are correlated with E^T_{MISS}.
The transverse mass variable M_T is instead more efficient than the other two variables, estimating correctly within 5% the number of background events in the Signal Region for both the normalisation regions. The statistical error here is about 5% because of the lowest number of events in the Control and normalisation region with respect to the other two variables. The discrepancy between the measured and estimated events is then within the statistical error.

In Table 4.6 and 4.7 the same estimates are shown when the SU4 SUSY signal is added to the SM background.
First of all it is important to notice that the SUSY signal is present also in the Control Region and then it affects the estimation. In fact, the second and third columns of the Table 4.6 and Table 4.7 should be similar if the Control Region was strongly dominated by SM events and the estimation method was correct when only the SM background is present. The effect of this contamination is to mask the excess of SUSY signal events and consequently to lower the significance. The contamination masks the 25-30% of the true signal events for HT2 and m(lj) variables, but the 70% for the M_T

Table 4.4: Number of estimated and true events in the Signal Region, if only the SM background is present. The normalisation region used in the table is 60-100 GeV in E^T_{MISS}. All the numbers are normalised to 1 fb^{-1}.

	SM estimated	SM true	Ratio
HT2	1290	1772	0.73±0.02
m(lj)	1437	1777	0.81±0.02
M_T	2053	2032	1.01±0.04

Table 4.5: Number of estimated and true events in the Signal Region, if only the SM background is present. The normalisation region used in the table is 60-120 GeV in E^T_{MISS}. All the numbers are normalised to 1 fb^{-1}.

	SM estimated	SM true	Ratio
HT2	681	1114	0.61±0.02
m(lj)	717	1133	0.63±0.02
M_T	1120	1198	0.94±0.05

variable, as shown in Table 4.6 and 4.7.
The significance of the excess of SUSY events quoted in tables 4.6 and 4.7, has been computed assuming a poissonian distribution for the estimated number of SM background events, with gaussian systematic errors calculated taking into account the statistical uncertainty of the rescaling procedure and the systematic uncertainty due to the wrong estimation of the SM background in the "background only" case. The latest contribution has to be assumed as a systematic error because it is strictly related to the choice of the discriminating variable that belongs to the definition itself of the method.
As tables 4.4 and 4.5 show, the systematic error is largely dominant for the HT2 and m(lj) variables (27% for HT2 and 19% for m(lj)), strongly lowering the significance with respect to M_T (6%), even if the signal over background ratio is better for the former variables. Narrowing the normalisation region this effect is less important, allowing to reach a significance of about 3-3.5 for both variables.
For the same reason, the transverse mass variable is the most performing one, even if the contamination reduces its capability to be a good estimator. Nevertheless, the significance that can be reached with an integrated luminosity of 1 fb^{-1} is 6.6, demonstrating that the SUSY contamination in the control region should not prevent a possible discovery.

Table 4.6: Number of estimated and true events in the Signal Region passing all the selection cuts, if both the SM background and the SUSY signal are present. The normalisation region used in the table is 60-100 GeV in E^T_{MISS}. The second column represents the number of estimated SM events with the error related to the estimation, the third column represents the true number of events passing the cuts in the Signal Region, the fourth column represents the estimated number of signal events, the fifth column represents the true number of signal events and the sixth column represents the statistical significance of the excess of signal events with respect to the estimated SM background. All the numbers are normalised to 1 fb^{-1}.

	SM Est.	SM true	SU4 signal est.	SU4 signal true	Significance
HT2	3006±1127	1772	3234	4468	2.9
m(lj)	3245±775	1777	2644	4112	3.4
M_T	4815±241	2032	1354	4137	5.8

Table 4.7: Number of estimated and true events in the Signal Region passing all the selection cuts, if both the SM background and the SUSY signal are present. The normalisation region used in the table is 60-120 GeV in E^T_{MISS}. The second column represents the number of estimated SM events with the error related to the estimation, the third column represents the true number of events passing the cuts in the Signal Region, the fourth column represents the estimated number of signal events, the fifth column represents the true number of signal events and the sixth column represents the statistical significance of the excess of signal events with respect to the estimated SM background. All the numbers are normalised to 1 fb^{-1}.

	SM Est.	SM true	SU4 signal est.	SU4 signal true	Significance
HT2	1986±1263	1114	2792	3664	2.2
m(lj)	2072±1204	1133	2479	3416	2.1
M_T	3074±231	1198	1570	3446	6.6

The effect of the contamination is also visible in Fig.4.3, 4.4 and 4.5, representing respectively the estimation performed using HT2, m(lj) and M_T variables. For all of them, the upper plot is produced using the narrowest E^T_{MISS} normalisation region (60-100 GeV), while the lower plot using the widest E^T_{MISS} normalisation region (60-120 GeV).
In all the plots, the estimation of the SM background in the Signal Region,

represented by the full triangles, systematically overestimates the "real" SM contribution in the Signal Region (black solid curve). The reason of this overestimation is the contamination of the SU4 SUSY signal in the Control Region.
The effect of the correlation between E^T_{MISS} and HT2 and between E^T_{MISS} and m(lj), is confirmed looking at the relation between the SM contribution (black solid line) and the estimation of the SM background in the "SM background only" case (full circles in Fig.4.3 and Fig.4.4). The correlation leads in these cases to a systematical underestimation of the SM background. This effect is instead negligible using M_T as discriminating variable (Fig.4.5).
Anyway, the estimation obtained using the transverse mass M_T is more precise that the other two variables because the overall error on the estimation procedure, computed including both the statistical errors and the systematic intrinsic error of the method, is 7.5% in case of M_T (using the normalisation region 60-100 GeV in E^T_{MISS}), but it is 38% for HT2 and 23% for m(lj) (using for both variables the narrowest normalisation region 60-100 GeV in E^T_{MISS}).
The "intrinsic" systematic error then is crucial in this estimation method because, with an integrated luminosity of 1fb^{-1}, it dominates over the statistical errors of the method, causing a significant lack of discovery potential.

In Table 4.8 and 4.9, the same results as in Table 4.6 and 4.7 (e.g. the significance of the estimation method when both the SUSY signal and the SM background are present) are shown, but with an integrated luminosity of 100pb^{-1}.
The effect of the poorer statistics leads, as expected, to a lowering of all the significances.
This effect is present especially in the significance obtained using the transverse mass M_T as discriminating variable. Even using the 60-120 GeV normalisation region in E^T_{MISS} (the best choice for an integrated luminosity of 1 fb^{-1}), the significance is 3.9. Moreover, the statistical error is larger leading to an overall error (statistic and systematic) of 11% (it was 7.5% for the 1fb^{-1} case) in the estimation method .
The use of the other two variables using the 60-100 GeV normalisation region in E^T_{MISS} gives a similar potential with respect to the use of transverse mass variable, even if the statistical and the "intrinsic" systematic (e.g. the discrepancy in the estimation of the SM background when only the SM background is present) errors of the method are still quite large (38% for HT2 variable and 25% for the m(lj) variable).
Hence, with an integrated luminosity of 100pb^{-1}, the three methods show a more similar discovery potential with a significance varying from 2.7 to 3.9, depending on the variable used to perform the estimation.

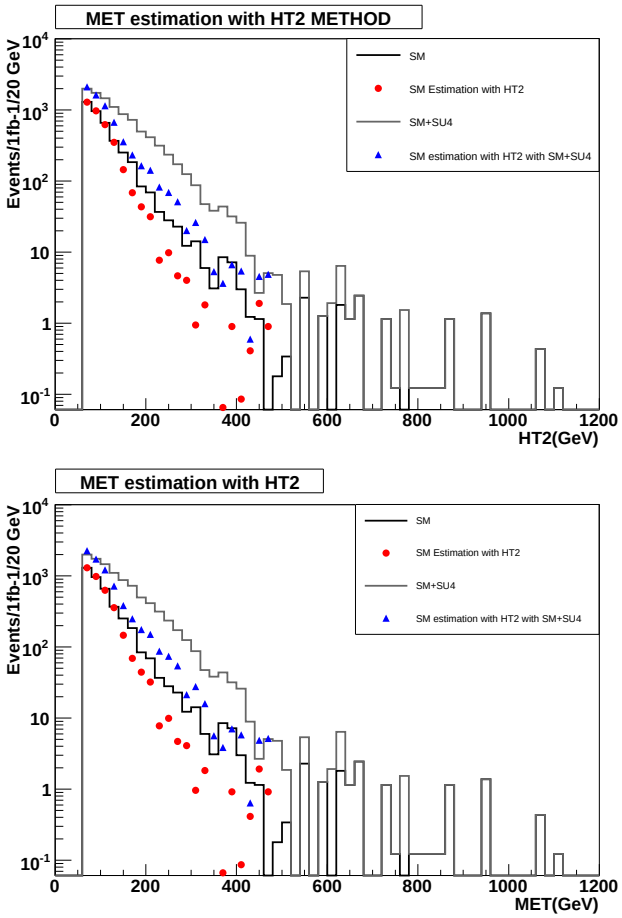

Figure 4.3: The E^T_{MISS} distributions of the events in the Signal Region, here defined by the cut HT2 $>$ 200 GeV. For both plots, the black solid line represents the contribution of all the SM considered backgrounds, the gray solid line represents the distribution when the SUSY signal is added to the SM background. The full dots represent the estimation of the E^T_{MISS} distribution in the Signal Region when only the SM background is present, while the triangles represent the estimation of the SM background in the Signal Region when also the SUSY signal is present. In the upper plot the estimation is obtained normalising the E^T_{MISS} distribution in the 60-100 GeV range, while the lower plot is obtained normalising the E^T_{MISS} distribution in the 60-120 GeV range, as described in the text. All the distributions are normalised to 1 fb^{-1}.

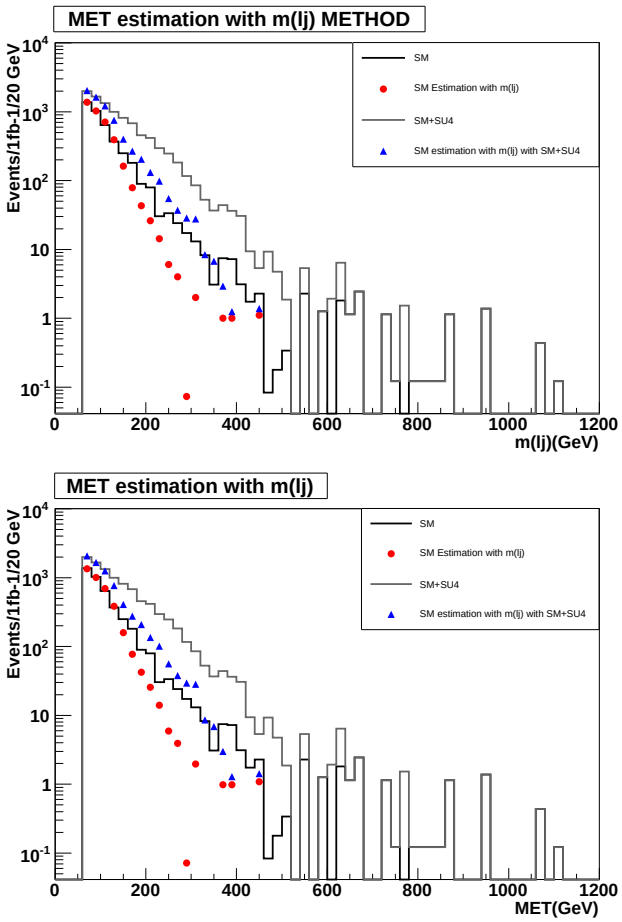

Figure 4.4: The E^T_{MISS} distributions of the events in the Signal Region, here defined by the cut m(lj)$>$ 120 GeV. For both plots, the black solid line represents the contribution of all the SM considered backgrounds, the gray solid line represents the distribution when the SUSY signal is added to the SM background. The full dots represent the estimation of the E^T_{MISS} distribution in the Signal Region when only the SM background is present, while the triangles represent the estimation of the SM background in the Signal Region when also the SUSY signal is present. In the upper plot the estimation is obtained normalising the E^T_{MISS} distribution in the 60-100 GeV range, while the lower plot is obtained normalising the E^T_{MISS} distribution in the 60-120 GeV range, as described in the text. All the distributions are normalised to 1 fb^{-1}.

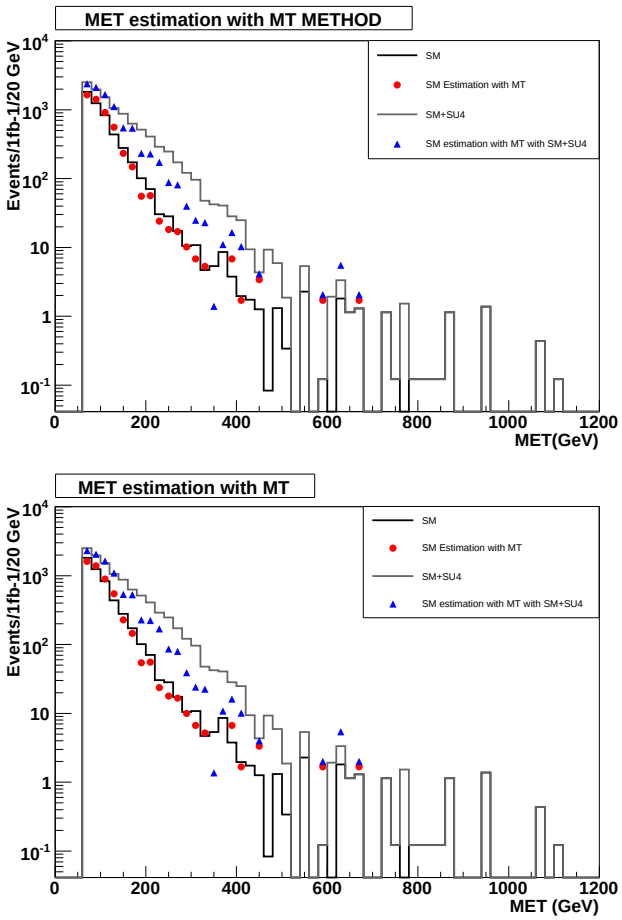

Figure 4.5: The E^T_{MISS} distributions of the events in the Signal Region, here defined by the cut $M_T \notin [60-100]$ GeV. For both plots, the black solid line represents the contribution of all the SM considered backgrounds, the gray solid line represents the distribution when the SUSY signal is added to the SM background. The full dots represent the estimation of the E^T_{MISS} distribution in the Signal Region when only the SM background is present, while the triangles represent the estimation of the SM background in the Signal Region when also the SUSY signal is present. In the upper plot the estimation is obtained normalising the E^T_{MISS} distribution in the 60-100 GeV range, while the lower plot is obtained normalising the E^T_{MISS} distribution in the 60-120 GeV range, as described in the text. All the distributions are normalised to 1 fb^{-1}.

Table 4.8: Number of estimated and true events in the Signal Region passing all the selection cuts, if both the SM background and the SUSY signal are present. The normalisation region used in the table is 60-100 GeV in E^T_{MISS}. The second column represents the number of estimated SM events with the statistical error related to the estimation, the third column represents the true number of SM events passing the cuts in the Signal Region, the fourth column represents the estimated number of signal events, the fifth column represents the true number of signal events and the sixth column represents the statistical significance of the excess of signal events with respect to the estimated SM background. All the numbers are normalised to 0.1 fb^{-1}.

	SM Est.	SM true	SU4 Signal est.	SU4 Signal true	Significance
HT2	301 ± 114	177	323	447	2.7
m(lj)	325 ± 81	178	264	411	3.0
M_T	482 ± 58	203	135	414	2.0

Table 4.9: Number of estimated and true events in the Signal Region passing all the selection cuts, if both the SM background and the SUSY signal are present. The normalisation region used in the table is 60-120 GeV in E^T_{MISS}. The second column represents the number of estimated SM events with the statistical error related to the estimation, the third column represents the true number of SM events passing the cuts in the Signal Region, the fourth column represents the estimated number of signal events, the fifth column represents the true number of signal events and the sixth column represents the statistical significance of the excess of signal events with respect to the estimated SM background. All the numbers are normalised to 1 fb^{-1}.

	SM Est.	SM true	SU4 Signal est.	SU4 Signal true	Significance
HT2	199 ± 126	111	279	366	2.1
m(lj)	207 ± 120	113	248	342	2.0
M_T	307 ± 33	120	157	345	3.9

4.5.1 Systematic uncertainties

The systematic uncertainties of the estimation method, for both the normalisation regions used (i.e. 60-100 GeV and 60-120 GeV) and for each of the three variables analysed, are summarised in tables 4.10 and 4.11.
The systematic uncertainties are computed from the variation of the ratio between the number of estimated SM events and true SM events in the signal region with respect to the values shown in tables 4.4 and 4.5.
The systematic uncertainty related to Jet Energy Scale has been computed varying by $\pm 5\%$ the energy and the momentum of all the jets in the events, and recalculating consequently the transverse missing energy. The systematic uncertainty related to Lepton Energy Scale has been computed varying by $\pm 0.2\%$ the energy and the momentum of all the leptons in the events, and recalculating consequently the transverse missing energy.
The systematic uncertainty due to changes in Monte Carlo event generation parameters has been evaluated comparing MC@NLO and AcerMC generators, while the systematic uncertainty related to the variation of the hadronization parameters has been evaluated using Monte Carlo samples, where the Initial State Radiation (ISR) and Final State Radiation (FSR) parameters of PYTHIA were changed, with the physical effect to have a lower or higher top mass value.
The total systematic uncertainty is lower when the narrowest normalisation region is chosen for all the three variables considered above. It is instead higher for the M_T variable with respect to the other two variables.
The estimation method using M_T variable, that has been proved to be the more performing variable to estimate the SM background, has then an overall systematic uncertainty of 10.5 %. This value has to be added to the statistical error to recalculate the significance of the SU4 SUSY excess over the SM background. The significance using the M_T variable and the normalisation region 60-120 GeV in E^T_{MISS} with a systematic error of 10.5 % added to the statistical error related to the estimation method is 4.0 (it was 6.6).
Anyway, some of the systematic uncertainties will be strongly reduced after the first phase of LHC data taking. In particular the uncertainty on jet and lepton energy scale can reach the 1 % and 0.1 % respectively [3]. Furthermore, the uncertainties on the other sources of systematic, can be reasonably reduced by a factor two, using measured $t\bar{t}$ events from collisions. Under these assumption, the systematic uncertainties can become comparable to the statistical error of the estimation procedure, leading to a significance of 5.0.
Hence, the value of 10.5 % of systematic uncertainty for the method using the M_T variable is pessimistic.

Table 4.10: Breakdown of systematic uncertainties in the estimation method. The normalisation region used here is 60-100 GeV in E_T^{MISS}. The first column represents the source of the uncertainty, the second, third and fourth columns represent the contribution of each source for HT2, m(lj) and M_T variables.

Systematics uncertainty source	Contribution (%)		
	HT2	m(lj)	M_T
Jet Energy Scale	2 %	1 %	2.5 %
Lepton Energy Scale	1 %	1 %	1 %
MC@NLO vs AcerMC	2 %	5 %	7 %
Monte Carlo parameters (ISR/FSR)	3 %	1 %	3 %
Total	4.5 %	6 %	8 %

Table 4.11: Breakdown of systematic uncertainties in the estimation method. The normalisation region used here is 60-120 GeV in E_T^{MISS}. The first column represents the source of the uncertainty, the second, third and fourth columns represent the contribution of each source for HT2, m(lj) and M_T variables.

Systematics uncertainty source	Contribution (%)		
	HT2	m(lj)	M_T
Jet Energy Scale	3 %	3 %	3.5 %
Lepton Energy Scale	1 %	1 %	1 %
MC@NLO vs AcerMC	3 %	1 %	6 %
Monte Carlo parameters (ISR/FSR)	7 %	6 %	7.5 %
Total	8 %	7 %	10.5 %

4.6 Optimization and scan in the mSUGRA space

The SU4 SUSY point studied so far was chosen as a benchmark point for a region in the mSUGRA parameter space, where the mass of the SUSY particles are relatively low. Obviously, there is no reason to think that it is representative of what might be found at the LHC. This section uses scan over the parameters of the mSUGRA model in order to sample a wider range of possibilities. The goal is to optimize the search strategy shown in the previous sections in order to cover as wide as possible the whole mSUGRA

parameter space, with particular attention to the "low mass" region of the space. The benchmark integrated luminosity will be 1 fb^{-1}, because the focus is still on the early data phase of LHC. Since this scan over the mSUGRA parameter space includes hundreds of points, in this section, one must rely on ATLFAST [2], the fast parametrized simulation of the ATLAS detector. It is impossible to scan the 105-dimensional parameter space of the MSSM, or even the 19 dimensional sub-space with flavour and CP conservation and degeneracy of the first two generations. Hence a number of SUSY-breaking models with many fewer parameters are usually used [1]. As said before, here the focus will be only on the mSUGRA model.

To perform the scan, a 25×25 fixed grid in the (m_0,$m_{1/2}$) plane has been defined, keeping the other parameters values of the model as constants: $tan\beta = 10$, $A_0 = 0$ and $\mu > 0$.

The 25×25 grid was made varying m_0 from 60 GeV to 2940 GeV in 25 steps of 120 GeV, and $m_{1/2}$ from 30 GeV to 1470 GeV in 25 steps of 60 GeV. SUSY spectra were generated using ISAJET 7.75 [4] with top quark mass of 175 GeV. Out of the 625 possible points, a spectrum could be successfully generated for 600; the other 25 failed for theoretical reasons (or the LSP is the $\tilde{\tau}_1$ or the electroweak symmetry breaking mechanism does not happen). For each good point, 20K events were produced using ATLFAST. Constraints other than from direct searches (LEP and TEVATRON) were ignored.

The analysis described above has used signal and background cross-sections normalised to next-to-leading-order calculations for nearly all the generated Monte Carlo samples. This was impractical for scan over many points, each involving many subprocesses. The goal here is not to determine the exact limit or exclusion value, but rather to test whether the proposed approach works for a wide range of mSUGRA points. Hence, the signal cross-sections for all the points of the grid are computed at leading-order by HERWIG, while the next-to-leading-order cross-sections are still used for the backgrounds. Since next-to-leading-order corrections generally increase cross-sections, the resulting reach estimates are conservative.

ATLFAST is a fast parametrised simulation of the ATLAS detector. The version used here is rather idealised. Corrections to the efficiency for electron reconstruction were applied as a function of p_T and η. In addition, in the ATLFAST algorithm that finds reconstructed cone jets, the split-merge step was missing. So that, jets matched to the same truth jet were combined. With these corrections the ATLFAST and full simulations agree reasonably well. All results shown here use ATLFAST with these corrections.

The reach plot in this section is based on the estimation procedure described in the previous sections, using the M_T variable and the normalisation region of 60-120 GeV in missing energy.

Before performing the scan on the whole mSUGRA parameter space, an optimisation procedure has been implemented, varying the thresholds on transverse missing energy and the two hardest jets of the event. This choice has been taken because the previous thresholds were very useful to test the validity and study the systematic uncertainties related to the estimation method, but they were not specifically focused on "low mass" regions of the mSUGRA space. Hence the cuts on missing energy and two hardest jets of the event have been chosen as those that optimize the significance of the SUSY excess for SU4 SUSY point. In particular, a scan over the transverse momentum thresholds for the two hardest jets has been performed. Three different thresholds have been evaluated: 70-50 GeV, 120-50 GeV and 200-80 GeV, where the first number represents the cut on the hardest jet and the second number the cut on the second hardest jet.
The transverse missing energy threshold has been left at 60 GeV and the control region is still defined in the range 60-120 GeV.
For each value of the momentum threshold of the two hardest jets, the signal region has been defined performing a scan in transverse missing energy from 120 to 300 GeV.
The estimation method has then been applied for each jet-transverse missing energy combination, estimating the number of SM and SUSY events in the signal region and then computing the significance.
The total systematic uncertainty of 10.5%, computed in the previous section, is added to the statistical error of the estimation procedure, in order to ensure a more reliable estimation of the significance of the SUSY excess over the SM background.
The combination of cuts in transverse missing energy, leptons and jets giving the best significance for SU4 SUSY point, in presence of systematic uncertainties, is the following:

- $E^T_{MISS} > 180$ GeV;
- At least two jets with $p_T > 80$ GeV and one jet with $p_T > 200$ GeV;
- Exactly two opposite sign leptons (electrons or muons) with $p_T > 15$ GeV and $|\eta| < 2.5$;

Using these cuts, there are 111 true SM events, and 842 SU4 events in the signal region. The number of estimated events in this region is 446 ± 76 events for SM and 507 events for SU4 SUSY signal. The estimation has then a statistical uncertainty of 17 % due to the limited number of events. The addition of a systematic uncertainty of 10.5 % leads to an overall uncertainty of 19.5 % and the significance is then 5.5.
The scan over the whole mSUGRA parameter space has then been implemented performing the analysis with the cuts on jets and transverse missing

energy described above. For each SUSY point in the mSUGRA grid, the estimation procedure has been repeated as in the SU4 case described in the previous section, normalizing the results to the integrated luminosity of 1 fb^{-1} and computing the significance of the SUSY signal excess over the SM background. In the significance calculation, both the statistical and the systematic uncertainties have been taken into account.
The result of the scan over the mSUGRA space parameter is shown in Fig.4.6. Different colours represent the different values of the statistical significance, computed as previously explained. An iterative procedure has been applied to the various point of the mSUGRA plane, in order to interpolate the significance in the regions not covered by the SUSY grid points, and then to smoothly connect the values each other. Fig.4.6 shows only the mSUGRA regions allowed by the experimental limits coming from the direct searches of SUSY at LEP and TEVATRON.
The highest significance, as expected, is in correspondence of the "SU4-like" region ($m_0 \approx 150-300$, $m_{1/2} \approx 150-200$) with a significance near to 5 (red and orange regions). The neighbouring regions, drawn in yellow and green, have a significance slightly lower, but the region where $m_0 < 350$ GeV and $m_{1/2} < 250$ GeV is nearly completely covered with a significance larger than 3. A tiny region with $m_0 \approx 100$ GeV and $m_{1/2}$ in the range (150-350) GeV is also characterised by a significance larger than 3.
The drop of significance in the region with $m_0 < 150$ GeV and $m_{1/2} < 150$ GeV, is mainly due to the limited available statistic for the points of the mSUGRA space lying in this region . Starting from 20K simulated events, the cross-section is of order of 1 nb, giving an integrated luminosity of some pb^{-1}, while the integrated luminosity available for the SU4 point is 650 pb^{-1}. Anyway, this region has already been excluded by TEVATRON limits due to its high cross-section, and then it is meaningless.
Furthermore, LEP limits exclude the region in Fig.4.6 with $m_{1/2} < 120$ GeV for $m_0 < 600$ GeV, while TEVATRON exclude at 95% C.L. the region with $m_{1/2} < 150$ GeV for low m_0 smaller than 200 GeV.
Despite the pessimistic estimation of the systematic uncertainties affecting the analysis and the limited statistics to estimate the SM background, it is important to notice that the 3σ evidence should be possible, already with 1 fb−1, in the region where $m_0 < 350$ GeV and $m_{1/2} < 250$ GeV, quite far from the actual direct limits described above.
By increasing the integrated luminosity and reducing the systematics, the 5σ discovery reach potential should then be extended until the regions characterised in the plot by a significance of 3 or more. The estimation method is then competitive for an early discovery not only in the SU4 benchmark point, where it has been studied, but also in a wider region of the mSUGRA parameter space.

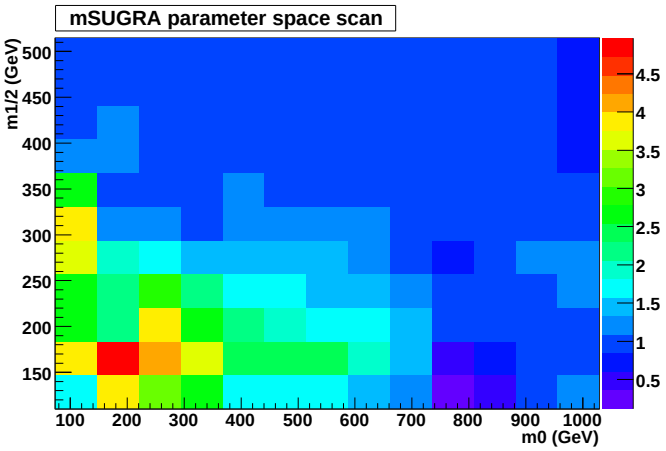

Figure 4.6: The 1fb−1 discovery potential in the mSUGRA space parameter as a function of m_0 and $m_{1/2}$ in GeV. Different values of the statistical significance of the SUSY excess with respect to the SM background, are associated to the colours following the legend on the right side of the plot. The cuts applied to perform the analysis are: $E^T_{MISS} > 180$ GeV, at least two jets with $p_T > 80$ GeV but one jet with $p_T > 200$ GeV and exactly two opposite sign leptons (electrons or muons) with $p_T > 15$ GeV and $|\eta < 2.5$.

4.7 Summary

In this chapter, a data driven estimation method of the SM background to SUSY events characterised by two isolated leptons, jets and missing energy has been studied. It has been implemented using three different choices of a kinematical variable (HT2, the lepton-jet invariant mass m(lj) and the transverse mass M_T) combined with the transverse missing energy. M_T variable is the most efficient to perform this estimation, allowing a significance of the SUSY excess over the SM background of 6.6, taking into account only the statistical uncertainty, for the benchmark SUSY point SU4 and for an integrated luminosity of 1fb^{-1}. Some of the systematic uncertainties related to the detector performance (Jet and Lepton energy scale) and to the Monte Carlo generators used to simulate the events, have also been evaluated and then added to statistical uncertainty, in order to evaluate the discovery potential in the whole mSUGRA parameter space. The result of the scan in the mSUGRA parameter space indicates that ATLAS should discover sig-

nals, for R-parity conserving SUSY, in the 2 lepton channel with gluino and squarks masses smaller than about 400 GeV/c^2, after having accumulated and understood data corresponding to an integrated luminosity of 1fb^{-1}.

Bibliography

[1] ATLAS Collaboration, Expected Performance of the ATLAS Experiment, Detector, Trigger and Physics. Supersymmetry Searches in ATLAS Chapter, CERN-OPEN-2008-020, Geneva, 2008, to appear.

[2] E. Richter-Was, D. Froidevaux, L.Poggioli, ATLFAST 2.0 a fast simulation package for ATLAS; Atlas Note ATL-PHYS-98-131.

[3] ATLAS Collaboration, Detector and Physics Performance Technical Design Report CERN/LHCC/99-14/15 (1999);

[4] F.Paige, S.Protopopescu, H.Baer and X.Tata, ISAJET 7.69: A Monte Carlo event generator for p p, anti-p p and e+e- reactions; hep-ph/0312045, 2003.

Chapter 5

Exclusive studies in the 2 leptons channel

5.1 Introduction

In this chapter I will concentrate on the reconstruction of the kinematics related to the production of two leptons in the decay chain of the supersymmetric particles eventually produced.
Once a signature consistent with Supersymmetry has been established using the strategies explained in chapter 4, the experimental emphasis will move on the sparticles mass spectrum and later on the model parameters. This kind of analysis will be performed with a statistics larger that the one needed for an inclusive search (chapter 4). However the analysis contained in this chapter considers 1 fb^{-1} as a benchmark integrated luminosity in order to establish the precision and the sensitivity achievable with early data.
The purpose of the analysis described here is therefore limited to the reconstruction of the kinematics of heavier sparticles decays involving two leptons. The extraction of the masses and the parameters of the model, as discussed in [1], needs more statistics to give reliable results.

5.2 The signature

In the case of R-parity conserving models, the decay chains of sparticles cannot be completely reconstructed because sparticles eventually decay into LSPs that escape detection. For this reason edges, rather than mass peaks, are measured in the invariant mass distributions of sparticle decay products. Obviously a complete coverage of all allowed SUSY models is impossible. However the measurement techniques and fit methods developed here can

be adapted for many models, not only within the mSUGRA framework.
During the initial data taking, the error on such measurements will be limited by statistics, making measurements possible only for models with moderate ($\leq$ 1TeV) values of the SUSY mass scale where enough events can be isolated.
Hence the focus in this work will be on cases:

- Total integrated luminosity of 0.5 fb^{-1} for the "Low mass" point (SU4);
- Total integrated luminosity of 1 fb^{-1} for the SU3 point in the "Bulk region".

The decay chain studied here is the following one:

$$\tilde{q}_L \rightarrow \tilde{\chi}_2^0 q \rightarrow \tilde{l}^{\pm} l^{\mp} q \rightarrow \chi_1^0 l^+ l^- q \tag{5.1}$$

in events containing two opposite sign isolated electrons or muons, hard jets and missing transverse energy. As previously said, because of the missed detection of the $\tilde{\chi}_1^0$ (LSP), the invariant mass of the two opposite sign leptons presents a kinematic endpoint that is a function of the masses of the particles involved in the decay . If the sleptons $\tilde{l}^{\pm}$ are heavier than the $\tilde{\chi}_2^0$, then the decay proceeds through the direct three body decay channel $\tilde{\chi}_2^0 \rightarrow \tilde{\chi}_1^0 l^+ l^-$ as in the SU4 benchmark point. In this case, the distribution of the invariant mass of the two leptons has a non triangular shape described in [4], with an endpoint equal to the difference of the mass of the two neutralinos:

$$m_{ll}^{edge} = m_{\tilde{\chi}_2^0} - m_{\tilde{\chi}_1^0} \tag{5.2}$$

If at least one of the sleptons is lighter than the $\tilde{\chi}_2^0$, then the two body decay channel $\tilde{\chi}_2^0 \rightarrow \tilde{l}^{\pm} l^{\mp} \rightarrow \chi_1^0 l^+ l^-$ dominates. The distribution of the invariant mass of the two leptons is triangular, with an endpoint at:

$$m_{ll}^{edge} = m_{\tilde{\chi}_2^0} \cdot \sqrt{(1 - \frac{m_{\tilde{l}}^2}{m_{\tilde{\chi}_2^0}^2})} \sqrt{(1 - \frac{m_{\tilde{\chi}_1^0}^2}{m_{\tilde{l}}^2})} \tag{5.3}$$

For the SU3 benchmark point, where the $\tilde{l}_R$ and the $\tilde{\tau}_1$ are lighter than the $\tilde{\chi}_2^0$, such an endpoint is expected in the l^+l^- distribution for $m_{edge}^{ll} = 100.2$ GeV/c^2.
For SU4 benchmark point, where instead the slepton is heavier than the $\tilde{\chi}_2^0$, such an endpoint is expected in the l^+l^- invariant mass distribution for $m_{edge}^{ll} = 53.6$ GeV/c^2.
An advantage of both the decays described above, is the possibility to estimate both the SUSY combinatorial background and the Standard Model

(SM) background from the data with high accuracy. The technique known as flavor subtraction, is based on the fact that the signal contains two opposite-sign-same-flavor leptons (OSSF), while the background is from leptons coming from different and uncorrelated decay chains, which can be of the same flavor or different flavor with the same probability. The background thus cancels in the subtraction:

$$N(e^+e^-)/\beta + \beta N(\mu^+\mu^-) - N(e^\pm\mu^\mp) \tag{5.4}$$

where β is an efficiency correction factor equal to the ratio of the electron and muon reconstruction efficiencies. The value of β is 0.86 taken from [2] [3], and is assumed in the following to be known with a conservative uncertainty of 10%.

5.3 Event selection

Events with two or three isolated leptons (electrons or muons) with $p_T > 10$ GeV, $|\eta| < 2.5$ have been selected. As discussed in detail in chapter 3, leptons had to fullfill the identification criteria concerning: the "medium" cuts reconstruction algorithm and the calorimetric isolation for the electrons; the best combination between the muon spectrometer and the ID tracks and the calorimetric isolation for muons. These identification criteria was used since in SUSY searches it has been tested that they give a reasonable balance between the reconstruction efficiency and the fake rates with respect to jets and taus.
If two leptons are selected, they are required to have opposite sign. If three leptons are present, the two opposite-sign combinations are considered and treated independently in the rest of the analysis.
In order to select SUSY events and reject the SM background ($t\bar{t}$, W+jets, Z+jets and QCD events) it is necessary to require the presence of energetic jets and missing energy. So that, the variables used to discriminate SUSY from the SM background are the transverse missing energy (E^T_{MISS}), the transverse momenta of the four leading jets, the ratio E^T_{MISS}/M_{EFF} and the transverse sphericity of the event (S_T).
The cuts on E^T_{MISS} and p_T of the leading jet are required in order to have a high trigger efficiency that is fundamental to perform the analysis. In fact, the redundancy of the two lepton trigger and missing energy-jet trigger is one of the strengths of this channel, allowing to recover with the missing energy-jet trigger the events lost by the leptonic trigger. For SU4 point, the two lepton trigger $2\mu10$ or $2e15i$ (e.g. two isolated muons with $p_T > 10$ GeV or two isolated electrons with $p_T > 15$ GeV) has an efficiency of 18%, the single lepton trigger $\mu20$ or $e25i$ (e.g. one isolated muons with $p_T > 20$

GeV or one isolated electrons with $p_T > 25$ GeV) has an efficiency of 84% while the $j70xE70$ trigger (one jet with $p_T > 70$ GeV and $E^T_{MISS} > 70$ GeV) has 94.3% efficiency. For SU3 point instead, the efficiency grows to 27% for di-leptonic trigger, 87.5% for the single lepton trigger and 98.9% for the missing energy-jet trigger.
In order to optimize the cuts on these variables, the value of

$$S = (N_{OSSF} - N_{OSDF})/\sqrt{N_{OSSF} + N_{OSDF}} \tag{5.5}$$

is maximized for the 2 benchmark points (SU3, SU4), where N_{OSSF} and N_{OSDF} are the number of same-flavor and different-flavor lepton pairs respectively.
The S variable is computed directly from data and no MC information are used. By maximizing the value of S, the selection efficiency for signal events is maximized, suppressing the SM and SUSY combinatorial background. In order to improve the sensitivity to the signal, only lepton pairs with the invariant mass $m_{ll} < m_{ll}^{edge} + 10$ GeV are considered. Since this true value m_{ll}^{edge} is not a priori known, this choice implies that the existence of the edge has already been observed and that afterwards the selection cuts are optimized as described here, in order to improve the separation between signal and background and to improve the measurement of the endpoint. The work is thus focused on determining selection cuts that would allow a precise endpoint measurement rather than on finding the first evidence for an excess in this channel.
In table 5.1 the optimal selection resulting from the scan in the main discriminating variables is shown. Both for SU3 and SU4 benchmark points a 2-jet+E^T_{MISS} selection is preferred, leaving out the cuts on third and fourth leading jets and on other variables like the ratio E^T_{MISS}/M_{EFF} or the transverse sphericity of the events (S_T) (see section 3.6 for the definitions), that usually are used to perform the inclusive analysis on Supersymmetry as described in chapter 4.
The scan has been performed in the following ranges: 100-300 GeV for the leading jets ($p_T, 1$) and transverse missing energy (E^T_{MISS}), 50-200 GeV for the second most energetic jet ($p_T, 2$).
For the SU3 "Bulk " point, the S-value is found to be stable in an interval around the maximum value (reached for the combination of cuts: $p^1_T > 180$ GeV, $p^2_T > 100$ GeV and $E^T_{MISS} > 120$ GeV), while for the "Low mass" point SU4, the best S-value is found for the loosest cuts allowed by the available Monte Carlo samples. We recall that a filter was applied in the Monte Carlo event generation in order to have a reasonable statistics. As showed in the previous section, looser cuts may be preferred for this "Low mass" point, giving probably a better S-value.

Table 5.1: Number of events after the optimized selection for the S-variables defined in formula 5.5 for signal (N_s) and Standard Model background (N_b) with range limit $m_{ll} < m_{ll}^{edge} + 10$ GeV for SU3 and SU4 benchmark points for 1 fb^{-1}. The best selection is shown.

	p_T^1 (GeV)	p_T^2 (GeV)	E_{MISS}^T (GeV)	s_{OSSF}	s_{OSDF}	b_{OSSF}	b_{OSDF}	S
SU3	180	100	120	615	149	93	92	15.1
SU4	100	50	100	3048	1574	411	419	19.9

Table 5.2: Number of leptons pairs passing the selection cuts optimized for the SUSY benchmark points SU3 (above) and SU4 (below), for 1 fb^{-1} of integrated luminosity. Standard Model background includes $t\bar{t}$, W, Z and WW, WZ, ZZ production. The contribution from $t\bar{t}$ is also indicated separately, as it constitutes the most important Standard Model background. The background due to QCD jets is negligible.

Sample	e^+e^-	$\mu^+\mu^-$	OSSF	OSDF
SUSY SU3	273.7	371.4	645.1	177.8
SM	76.1	120.5	195.6	172.1
$t\bar{t}$	75.1	114.7	189.8	165.1
SUSY SU4	1729.5	2670.5	4400.1	2856.3
SM	392.4	687.7	1081.1	1103.7
$t\bar{t}$	377.4	657.3	1034.7	1062.6

The number of signal and background lepton pairs passing the selection cuts, is shown in table 5.2 . All numbers are for 1 fb^{-1}.
The main SM background is always $t\bar{t}$, accounting for about 95% of the total SM background. The remaining background events are mainly from W, Z and di-boson production (WW, ZZ and WZ). The background due to QCD events is negligible because it is strongly reduced by the missing energy and the two isolate leptons requests. The fraction of SUSY events in the selected sample with OSSF leptons is 77% for SU3 point and 80% for SU4 point. In addition, the OSSF events differ from the OSDF events by about 10% for the SM events, while for SUSY events the difference is strongly enhanced (a factors 1.5 and 3.5 respectively for SU4 and SU3 points), due to the presence of the two opposite sign same flavor leptons in the decay chain in addition to the combinatorial and uncorrelated background of opposite sign different flavor events.

5.4 Reconstruction of the dilepton edge

The distribution of the invariant mass of same-flavor and different-flavor lepton pairs with opposite sign is shown in Fig.5.1, for the two benchmark points and the backgrounds studied here. In both pictures, the events have passed the optimized selection cuts described above for SU3 (upper plot) and SU4 (lower plot). The luminosities are respectively 1 fb^{-1} and 0.5 fb^{-1} for SU3 and SU4.
It can be seen, from the regions where the signal does not contribute (i.e. for the SM background and for $m_{ll} > m_{ll}^{edge}$ for SUSY), that the different-flavor distributions are similar to the same-flavor backgrounds. This justifies once again the correctness of the idea of the flavor subtraction technique, that is also applied in the fitting procedure, in order to increase the precision in the determination of the endpoint values.
The invariant mass distribution after this flavor subtraction procedure is shown in Fig.5.2.
The upper plot has been done in presence of the SU3 signal for an integrated luminosity of 1 fb^{-1}. The distribution has then been fitted with a triangle smeared with a Gaussian (bold curve) in order to take into account the experimental resolution in the energy of the reconstructed leptons. The width σ of the Gaussian has been left as a free parameter in the fit, where a value of 2.3 ± 1.3 GeV has been found. This value is compatible with the experimental resolution of few % in the lepton energy scale (see chapter 3). The dots with the error bars represent the result of the flavor subtraction for the SU3 signal events, while the histogram with the continuous line represents the contribution of the SM events to the invariant mass combination,

after the flavor subtraction procedure. The combinatorial background coming from SUSY and SM events where the two leptons are uncorrelated has been clearly removed, especially in the higher mass region beyond the nominal edge, ensuring a more precise determination of the endpoint.
The value obtained for the endpoint is $(99.7 \pm 1.4 \pm 0.3)$ GeV/c^2, where the first is the statistical error and the second is the systematic error, dominated by the uncertainty on the lepton energy scale and the lepton identification efficiency (the latest one is assumed to be 10%). This result is consistent with the true value of 100.2 GeV/c^2 calculated for this specific point from the Eq.5.3.

The right plot of Fig.5.2 shows the flavor subtracted distribution in presence of the SU4 signal for an integrated luminosity of 0.5 fb^{-1}. Also in this case, the technique shows its capability to strongly reduce the combinatorial background in the high invariant mass region, allowing a better estimation of the endpoint of the distribution.
The difference in shape of the distribution with respect to the previous one is visible, and is motivated by the fact that for SU4 point the slepton is heavier than the $\tilde{\chi}_2^0$, and then one has a direct three body decay $\tilde{\chi}_2^0 \rightarrow \tilde{\chi}_1^0 l^+ l^-$. Hence the fit was performed using the following function [4]:

$$\begin{aligned} \frac{d\Gamma}{dM_{inv}} = \quad & 2NM_{inv} \cdot \frac{\sqrt{M_{inv}^4 - M_{inv}^2(\mu^2+M^2)+\mu^2M^2}}{(M_{inv}^2 - M_Z^2)^2} \cdot \\ & \cdot[-2M_{inv}^4 + M_{inv}^2(2M^2+\mu^2) + \mu^2M^2] \end{aligned} \tag{5.6}$$

which describes the theoretical distribution for the three-body decay in the limit of large slepton mass as a function of the invariant mass $Minv$ of the leptons pair. The shape of the distribution depends then on 3 parameters: the normalization N, the sum of the two lightest neutralinos masses M and the difference between these two masses μ (that is the endpoint in this case).
The formula is then smeared by a Gaussian for the experimental resolution as in the SU3 case.
This function vanishes near the endpoint, and it is a better description of the distribution for SU4 than the smeared triangle with a sharp edge.
The endpoint from the fit is $(52.7 \pm 2.4 \pm 0.2)$ GeV/c^2, consistent with theoretical value of the endpoint 53.6 GeV/c^2.
Since the true distribution of the excess will not be known from data, the distribution has also been fitted with the smeared triangle expected for a two-body decay chain as in the SU3 case.
This fitting function also gives a good χ^2 with a probability of 84% (equal to the one given by the fit with the theoretical three-body function) and with an estimated endpoint of $(49.1 \pm 1.5 \pm 0.2)$ GeV, that is compatible with

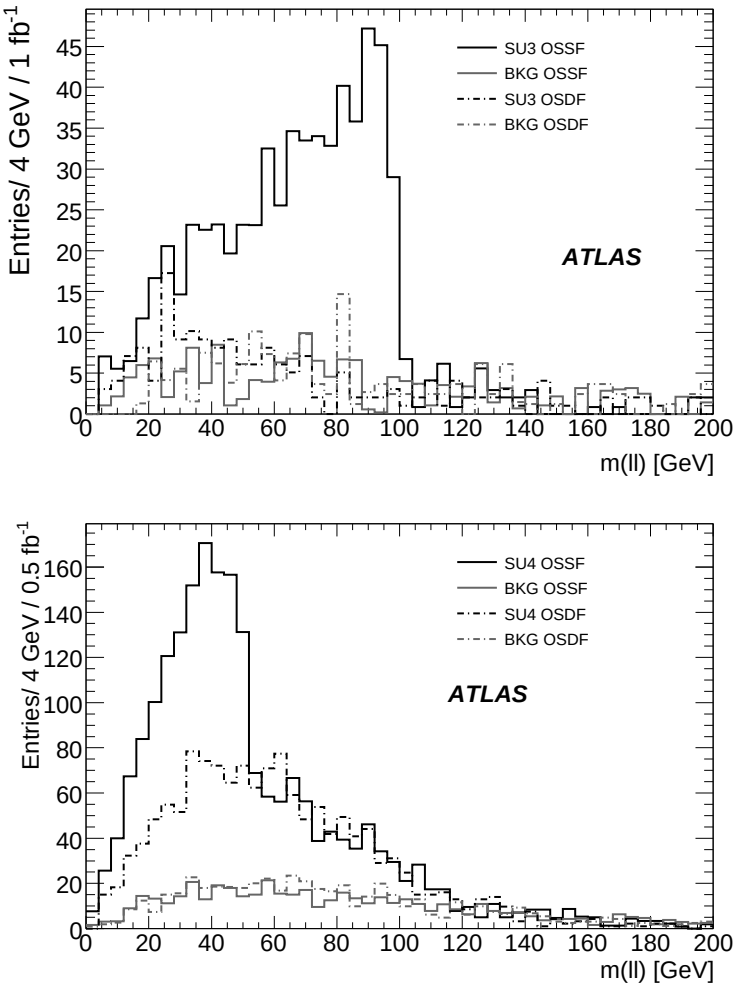

Figure 5.1: Distribution of the invariant mass of same-flavor and different-flavor lepton pairs with opposite sign for the SUSY benchmark points and SM backgrounds after the cuts optimized from data in presence of the SU3 signal (upper) and the SU4 signal(lower). The integrated luminosities are 1 fb^{-1} and 0.5 fb^{-1} respectively. In both cases, the solid black line represents the contribution of the SUSY Opposite Sign Same Flavor lepton pairs (SU3/SU4 OSSF), while the gray solid line represents the contribution of the SM Opposite Sign Same Flavor lepton pairs (SM OSSF). The dashed black line instead represents the contribution of the SUSY Opposite Sign Different Flavor lepton pairs (SU3/SU4 OSDF), while the gray dashed line represents the contribution of the SM Opposite Sign Different Flavor lepton pairs (SM OSDF).

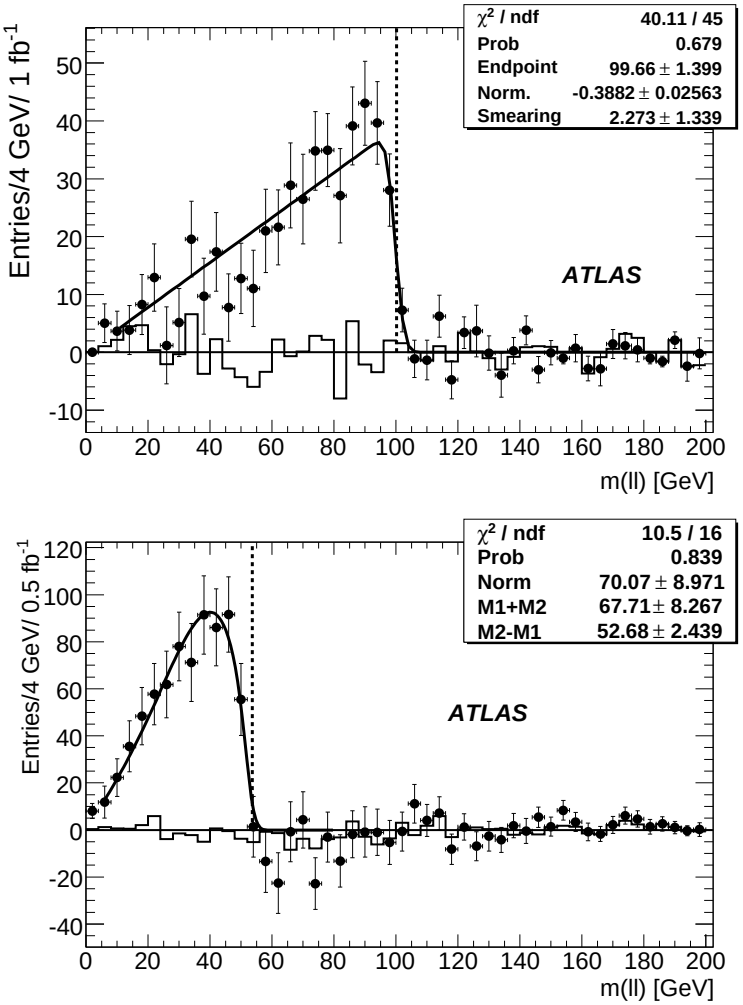

Figure 5.2: Distribution of invariant mass after flavor subtraction for the SU3 benchmark point (upper) with an integrated luminosity of 1 fb^{-1} and for the SU4 benchmark point (lower) with an integrated luminosity of 0.5 fb^{-1}. In both cases, the line histogram is the Standard Model contribution, while the points are the sum of Standard Model and SUSY contributions. The fitting function is superimposed and the expected position of the endpoint is indicated by a dashed vertical line.

endpoint value extracted from the fit with the three-body decay formula, but not compatible with the true value of 53.6 GeV/c^2.
A larger statistics is then required to use the shape of the dilepton invariant mass distribution to discriminate between the two-body and the three-body decays and, then, to find out conclusions on the nature of the decay chain and the mass spectrum of the slepton and the two lightest neutralinos.

5.5 Summary

After the discovery of Supersymmetry, the focus will be on measurements of the properties of the new particles. Here, the decay involving two opposite charge leptons from next-to-lightest-neutralino ($\tilde{\chi}_2^0 \rightarrow \tilde{\chi}_1^0 l^+ l-$) decay has been studied for the benchmark SUSY point SU3 and SU4 in the mSUGRA framework. The invariant mass of the two leptons shows a clear kinematic maximum which could be measured with a precision of few percent with an integrated luminosity of 1fb^{-1}. The values of these kinematical limits are in good agreement with the theoretical expected values for the benchmark points analysed. Fundamental in this sense is the application of the flavour subtraction procedure (difference between $ee+\mu\mu$ events and $e\mu$ events), that allows to estimate correctly from data the combinatorial SUSY background in this channel pointing out very clearly the position of the kinematical limit.

Bibliography

[1] ATLAS Collaboration, Expected Performance of the ATLAS Experiment, Detector, Trigger and Physics. Supersymmetry Searches in ATLAS Chapter, CERN-OPEN-2008-020, Geneva, 2008, to appear.

[2] ATLAS Collaboration, Expected Performance of the ATLAS Experiment, Detector, Trigger and Physics. Reconstruction and identification of electrons in ATLAS Chapter, CERN-OPEN-2008-020, Geneva, 2008, to appear.

[3] ATLAS Collaboration, Expected Performance of the ATLAS Experiment, Detector, Trigger and Physics. Muon reconstruction and identification performance in ATLAS: studies with simulated Monte Carlo samples Chapter, CERN-OPEN-2008-020, Geneva, 2008, to appear.

[4] U.De Sanctis, T.Lari, S.Montesano and C.Troncon, Perspectives for the detection and measurement of Supersymmetry in the focus point region of mSUGRA models with the ATLAS detector at LHC, European Physical Journal C, Vol.52 N.3 (2007).

Chapter 6

Summary and outlooks

6.1 Summary

This PhD thesis has examined the discovery potential in searches for Supersymmetry at ATLAS in the dileptonic channel with early data. In particular, the work has been focused on a "data driven" technique to estimate the Standard Model background in this channel and on measuring the properties of the new particles eventually produced.
All the results have been obtained in the mSUGRA model framework and referring to an integrated luminosity of 1fb^{-1}.
Events characterised by two isolated leptons, jets and missing energy have been studied, developing an estimation method of the SM background to SUSY events that completely relies on data (Chapter 4). This estimation procedure has been implemented using three different choices of a kinematical variable (HT2, the lepton-jet invariant mass m(lj) and the transverse mass M_T) combined with the transverse missing energy. The goal was to use the kinematical variable to discriminate Standard Model from SUSY events, and then to use the transverse missing energy in Standard Model events, to estimate their contribution in the regions of phase-space dominated by SUSY events.
The M_T variable is the most efficient to perform this estimation, allowing a significance of the SUSY excess over the SM background of 6.6, taking into account only the statistical uncertainty for the benchmark SUSY point SU4. Some of the systematic uncertainties related to the detector performance (Jet and Lepton energy scale) and to the Monte Carlo generators used to simulate the events have also been evaluated, contributing with a 10.5% to the overall uncertainty of the method. The systematic uncertainty has then been added to the statistical uncertainty, in order to evaluate the discovery potential in the whole mSUGRA parameter space. The result of

the scan in the mSUGRA parameter space indicates that ATLAS should discover signals, for R-parity conserving SUSY, in the 2 lepton channel with gluino and squarks masses smaller than about 400 GeV/c^2, after having accumulated and understood data corresponding to an integrated luminosity of 1fb^{-1}.
After the discovery of Supersymmetry, the focus will be on measurements of new particles properties(Chapter 5). Here, the decay involving two opposite charge leptons from next-to-lightest-neutralino ($\tilde{\chi}_2^0 \rightarrow \tilde{\chi}_1^0 l^+ l-$) decay, has been studied for the benchmark SUSY point SU3 and SU4 in the mSUGRA framework. The invariant mass of the two leptons shows a clear kinematic maximum, which could be measured with a precision of few percent with an integrated luminosity of 1fb^{-1}. The values of these kinematical limits are in good agreement with the theoretical expected values for the benchmark points analysed. Fundamental in this sense is the application of the flavour subtraction procedure (difference between $ee+\mu\mu$ events and $e\mu$ events), that allows to estimate correctly from data the combinatorial SUSY background in this channel, pointing out very clearly the position of the kinematical limit.

6.2 Outlooks

The work shown here has to be considered as a starting point to study the SUSY discovery potential in the dileptonic channel. Even if the work was focused on early data, the estimation procedure shown here is more general and it can be also implemented for different scenarios characterised by a larger integrated luminosity. Obviously, the cuts chosen here have to be rediscussed, but the main idea of the method and its limitations are still valid.
The estimation technique developed here, lies on the assumption that the kinematical variable and missing energy are not correlated. As clearly shown, this is true only in the case of M_T variable, that is in fact the most efficient variable to perform this estimation.
The reduction of the correlation between missing energy and the kinematical variable used to discriminate SUSY signal from SM background, is one of the possible improvement of the method, because such a correlation introduces a systematic under/over estimation of the SM background that affects the performances of the method.
Another aspect that must be carefully evaluated is the contamination of the SUSY signal. For the "low mass" SU4 SUSY point studied here as a reference, the contamination can mask up to the 70% of the excess of the SUSY signal over the SM background, affecting the discovery potential of

the method. If SUSY exists at low mass scale, its kinematic will be probably very similar to the SM one, and then a solution to reduce the contamination in the control region will be crucial to completely exploit the capability of the method. A technique to evaluate and subtract the SUSY signal contribution in the control region is desirable, but it can be performed only once a clear SUSY signal will be seen. So that, the improvement in the beginning of the LHC data taking will be probably related to find another procedure allowing to reduce the SUSY contamination.
Finally, due to the lack of time and available statistics in the Monte Carlo samples (it will be quickly produced but not in time for this work), it has not been possible a complete evaluation of the SUSY discovery potential in this channel when the energy of the collisions will be 10 TeV, as it is foreseen for 2009. The main priority for the next future will be then to repeat this work adapting the cuts to the different kinematical situation, in order to be ready to verify the validity of the method in the early LHC phase.

Chapter 7

Acknowledgements

Sorpresa! Almeno i ringraziamenti li voglio scrivere nella mia lingua madre, sia perchè ho già insultato a sufficienza la lingua inglese in questo centinaio di pagine, sia perchè mi viene meglio esprimere i miei sentimenti in lingua originale.
Alla fine di questi tre anni di dottorato e di questo lavoro di tesi, mi sembra doveroso ringraziare alcune persone. Di sicuro ne dimenticherò qualcuna, e per questo chiedo venia fin da ora!
Innanzitutto il mio sentito ringraziamento va al prof.Francesco Ragusa, mio supervisor durante questi tre anni di dottorato. I suoi consigli, sia sul lavoro svolto che su cosa implichi la ricerca, sono stati molto preziosi e mi saranno utili anche per il futuro.
Voglio poi ringraziare la d.ssa Clara Troncon per la sua costante presenza nel gruppo e i suoi suggerimenti durante questi anni. Un ringraziamento particolare va poi al dott. Tommaso Lari che mi ha seguito in questo percorso scientifico con la sua grande competenza e disponibilità (nonostante lo obbligassi a lavorare ogni tanto anche durante il week-end, non si è mai tirato indietro!!). Mi ritengo fortunato di aver potuto lavorare a stretto contatto con lui e gli sono grato per il tempo che mi ha pazientemente dedicato e la qualità delle discussioni di fisica che abbiamo avuto.
Desidero inoltre ringraziare la prof.ssa Alessia Tricomi dell'università di Catania che ha gentilmente accettato di farmi da referee per questa tesi dandomi utili suggerimenti e il dott.Giacomo Polesello dell'INFN di Pavia che è sempre stato disponibile e prodigo di consigli durante questo periodo di studi.
Ringrazio anche tutti gli altri membri del gruppo Pixel di Milano, soprattutto la d.ssa Chiara Meroni e il dott.Attilio Andreazza, con cui ho collaborato un po' di meno, ma che sono comunque stati sempre gentili e disponibili con me. Assieme a loro voglio anche ringraziare i miei compagni di dottorato

Simone Montesano e Lidia Dell'Asta con cui ho collaborato molto volentieri quando ce n'è stato bisogno: mi auguro che almeno loro possano avere dei dati veri per la tesi di dottorato!!
Un sentito ringraziamento va anche a Caterina Pizio, che ha ispirato la parte del mio terzo capitolo sull'energia mancante e a Guido Negri che è stato di fondamentale aiuto nell'aiutarmi a scaricare i campioni Monte Carlo da analizzare e nel creare script di shell magnifici. Non posso poi dimenticare, Danilo Banfi, con cui ho condiviso in questi tre anni la passione per la bici, e che mi ha anche dato una mano nella parte della tesi riguardante la calorimetria elettromagnetica.
Un sentito ringraziamento lo devo a Chiara, che ha pazientemente letto questa tesi aiutandomi tantissimo nella forma e nella grammatica inglese, sebbene la fisica delle particelle non sia esattamente la sua professione....
Voglio concludere, infine, ringraziando i miei genitori, che mi hanno sempre motivato in questi anni a continuare a inseguire i miei sogni e le mie aspirazioni. Una fase importante della mia vita probabilmente si è conclusa con il dottorato; ora spero che se ne apra un'altra altrettanto ricca di soddisfazioni sia lavorative che personali, e che questo non sia un punto di arrivo ma di partenza verso il futuro.
A tutte queste persone, e a tutte le altre che ho avuto il piacere di incontrare in questi anni e che qui non sono state nominate, va il mio più sentito grazie per quello che mi hanno trasmesso: non vi dimenticherò.